A novel surface trapping apparatus for ultracold cesium atoms

and the investigation of an Efimov resonance

Dissertation

zur Erlangung des Doktorgrades an der
Fakultät für Mathematik, Informatik und Physik
der Leopold-Franzens-Universität Innsbruck

vorgelegt von

Bastian Engeser

durchgeführt am Institut für Experimentalphysik
unter der Leitung von
Univ.-Prof. Dr. Rudolf Grimm

Oktober 2006

Abstract

This thesis reports on the construction and characterization of a novel surface trapping apparatus for experiments with ultracold cesium atoms. As a first application in the realm of three-body physics, measurements of recombination rates were performed to investigate an Efimov resonance.

Optical dipole traps based on evanescent waves are used to trap and cool atomic samples in close proximity to a dielectric surface. Starting from an existing experimental setup, a complete redesign of the vacuum system was performed in order to replace an old stainless steel chamber by a glass cell with integrated prism. The main technical improvements of the new apparatus are superior optical access, better surface quality of the prism and faster magnetic field control. In addition, the carefully constructed magnetic coils are now capable of producing magnetic gradients to partially compensate the gravitational force.

In the surface trap, a sequence of cooling methods is applied to prepare thermal gases at temperatures down to 50 nK. These methods include Raman sideband-cooling on the surface and a novel evanescent-wave trap that employs an 80 W high-power diode laser. A standing-wave surface trap is demonstrated that provides highly anisotropic confinement while preserving long lifetimes and presents a promising tool for future experiments on two-dimensional systems.

The technical improvements were essential for measurements of three-body recombination which have led to the main scientific result of this thesis. By exploiting the unique magnetic tunability of interactions in ultracold cesium gases, a dramatic three-body loss resonance at large negative scattering lengths was revealed. In collaboration with another experiment [Kra06b], the resonance could be identified as a manifestation of an Efimov state which confirmed a long-standing theoretical prediction. In further measurements, the position of the resonance was accurately determined in dependence of the temperature of the atomic sample. As a result, the scattering length of maximum loss shifted by about 50 Bohr radii when the temperature was reduced from 500 nK to 50 nK. This observation serves as a testing ground for several theoretical models describing the evolution of a bound Efimov state into a continuum resonance. The direction, magnitude and saturation behavior of the shift are well reproduced by the models and hence further confirm the applicability of Efimov's framework to the cesium system.

Zusammenfassung

In dieser Arbeit wird der Aufbau und die Charakterisierung eines neuartiges Oberflächenexperiments für ultrakalte Cäsiumatome beschrieben. Als erste Anwendung im Bereich der Dreikörperphysik wurden Messungen von Rekombinationsraten zur Untersuchung einer Efimovresonanz durchgeführt.

Um ein atomares Gas in unmittelbarer Nähe einer dielektrischen Oberfläche zu fangen und zu kühlen werden optische Dipolfallen eingesetzt, die auf evaneszenten Wellen basieren. Eine existierende Vakuumapparatur wurde vollständig überarbeitet, um eine alte Stahlkammer durch eine Glaszelle mit integriertem Prisma zu ersetzen. Die wesentlichen technischen Verbesserungen des neuen Aufbaus sind ein überlegener optischer Zugang, bessere Oberflächenqualität des Prismas und schnellere Steuerung von Magnetfeldern. Zudem erlauben sorgfältig konstruierte Magnetspulen die Erzeugung eines Gradientenfelds, mit dem sich die Schwerkraft teilweise kompensieren lässt.

In der Oberflächenfalle lassen sich eine Reihe von Kühlmethoden anwenden, mit denen sich thermische Gase mit Temperaturen von unter 50 nK herstellen lassen. Zu diesen Methoden zählt Raman-Seitenbandkühlen auf der Oberfläche und der Einsatz einer neuen Falle, die eine evaneszente Welle mit einem Hochleistungs-Diodenlaser bei 80 W Laserleistung erzeugt. Mittels einer Stehwelle nahe der Oberfäche konnte eine weitere Falle demonstriert werden, die stark anisotropen Einschluss erzeugt und eine lange Lebensdauer des gefangenen Gases zulässt. Solche Fallen sind vielversprechende Werkzeuge für künftige Experimente mit zweidimensionalen Systemen.

Die technischen Verbesserungen waren wesentliche Voraussetzungen für Messungen zur Dreikörperrekombination, die zum Hauptresultat dieser Arbeit geführt haben. Unter Ausnutzung der einzigartigen magnetischen Abstimmbarkeit von Wechselwirkungen in ultrakalten Cäsiumgasen konnte eine dramatische Resonanz der Dreikörperverluste bei negativen Streulängen nachgewiesen werden. In Zusammenarbeit mit einem anderen Experiment [Kra06b] wurde die Resonanz als Beleg für einen Efimov-Zustand interpretiert und so eine seit langem bestehende theoretische Vorhersage bestätigt. In weiterführenden Messungen wurde die Position der Resonanz bei verschiedenen Temperaturen des atomaren Gases genau bestimmt. Als Ergebnis konnte gezeigt werden, dass sich die Streulänge des maximalen Verlusts um etwa 50 Bohr-Radien verschiebt, wenn die Temperatur von 500 nK auf 50 nK abgesenkt wird. Diese Beobachtung ließ sich mit theoretischem Modellen vergleichen, die den Übergang eines gebundenen Efimovzustands in eine Kontinuumsresonanz beinhalten. Sowohl Vorzeichen, Stärke als auch das Sättigungsverhalten der Verschiebung werden von den Modellen richtig beschrieben, wodurch die Anwendbarkeit von Efimovs Ergebnissen auf ultrakalte Gase aus Cäsiumatomen weiter bestätigt wird.

Contents

1 Introduction

Ultracold atomic gases provide quantum systems of exceptional purity and offer almost complete experimental control. Not only is it possible to prepare the atoms in a well-defined internal state, but also can the external motion be cooled until it reaches its ground state. Most of the physical interest in ultracold gases is centered around interactions, since they are crucial to understand the large variety of observed phenomena.

As regards external interactions, trapping potentials can be engineered in a flexible way. Laser light interacts with induced optical dipole moments, while magnetic fields act on the permanent magnetic moments of the atoms. Present day laser technology together with accurate magnetic coil design is therefore used to form potentials that vary in space and time in complex ways. In the first part of this thesis, the construction of a novel trapping apparatus is described. Well-known optical effects like evanescent-waves close to a dielectric surface and standing-wave interference patterns are exploited in combination with magnetic field gradients. With these tools, it is possible to obtain highly anisotropic trapping potentials. In such an environment, the vibrational energy quantum in a tightly confined direction can exceed any other energy scale of the system. The motion in this direction is then always in its ground state and the system lends itself to a description in lower dimensions. Systems of reduced dimensionality have attracted much interest since they can behave in a strikingly different way as compared to the three-dimensional case [Pri04].

As regards internal interactions, the description of collisions between atoms simplifies dramatically in the ultracold limit. Two-body interactions are completely characterized by a single parameter, the s-wave scattering length. For the typically dilute gases, interactions can be treated in a fundamental way without resorting to phenomenological approaches. What is more, there exists an easily accessible external handle to tune the internal interactions: the scattering length depends on the magnetic field when Feshbach resonances are present [Tie93, Ino98]. The atomic element of choice for our experiment is cesium, and it offers an abundant supply of useful Feshbach resonances. Measurements of the resonance positions have led to a precise understanding of the energy spectrum of weakly-bound molecules made of two cesium atoms [Chi04]. On this basis, it was possible to gather experimental evidence for Efimov states - special weakly-bound molecules made of three atoms [Kra06b]. The second part of this thesis deals with measurements of three-body recombination rates

that reveal a resonance due to an Efimov state. A further investigation of the resonance position at varying temperature is presented and confirms the link to Efimov physics.

While the influence of dimensionality on the behavior of a system is obviously of general interest, one might be tempted to dismiss the experimental findings on molecular cesium states as just another spectroscopic dataset characterizing the complicated interaction potentials between atoms. However, this impression is not adequate. It is important to realize that the details of the cesium-specific interaction potentials only matter for short distances between the atoms. When the size of weakly-bound molecules exceeds the domain of short-range potentials, such 'halo'-objects [Jen04] are subject to universal physical relations. Theoretical laws of general interest apply, with interaction details summarized in one or few parameters. The history of Efimov states demonstrates the universal applicability throughout various branches of physics. Initially predicted theoretically in the context of nuclear physics and experimentally sought after in molecular systems, they have now been discovered in atomic gases. As Efimov states have evaded their discovery for more than three decades, their detection demonstrates the experimental power of ultracold gases.

While Feshbach resonances have enabled the control of two-body interactions and the production of ultracold dimers, Efimov resonances now give access to the three-body sector. These developments rely on the tunability of internal interactions and highlight the favorable scattering properties of cesium. An especially appealing prospect would be to bring into play the other mainstay of our experiment and combine tunable internal interactions with highly anisotropic external interactions. Such experiments would open up unique possibilities to study the largely unexplored world of few-body quantum phenomena in lower dimensions.

2 Evanescent-wave trapping

Atom traps based on evanescent waves are a crucial ingredient to our experiments. Such traps provide highly anisotropic confinement close to a dielectric surface, which is appealing for the creation of low-dimensional quantum gases. In this chapter, we first analyze the classical atomic motion in the trapping potential and then discuss the importance of quantum effects.

2.1 Optical dipole potential

Ultracold matter requires traps which are well isolated from the room-temperature environment. While many experiments are based on magnetic traps, optical dipole forces present an attractive alternative [Gri00]. With optical traps, atoms can be held in their lowest internal state which reduces collisional losses. Also, the freedom to apply arbitrary magnetic fields makes optical traps favorable for magnetic tuning of interactions [Tie93, Ino98].

The dipole force is conservative and leads to a trapping potential that is simply proportional to the laser intensity. Large forces for tight confinement therefore require strong intensity gradients. An intriguing way to achieve strong gradients over a large area is the formation of an evanescent wave close to a dielectric surface. For blue-detuned light, the evanescent wave can be viewed as a repulsive 'coating' for the material surface and provides a mirror for ultracold atoms.

A detailed description of evanescent waves and their use as atom-optical elements is given in [For00, Dow96]. Typical parameters for our experiment and a discussion of the mostly negligible Van-der-Waals interaction can be found in [Ham02a].

In the following, we will analyze the motion of atoms bouncing on the evanescent wave under the influence of gravity. Special attention will be paid to the possible application of a vertical magnetic gradient which partially levitates the atoms (see appendix B) and replaces the constant of gravity g by an effective value $\tilde{g}$. The combined effect of gravity, magnetic gradient and evanescent-wave on the atomic motion can then be described by the conservative potential

$$U = U_0 \exp\left(\frac{-2z}{\Lambda}\right) + m\tilde{g}z \tag{2.1}$$

with the maximum optical potential U_0, the decay length Λ of the evanescent electric field, the mass of the cesium atom m and the height above the surface denoted by z.

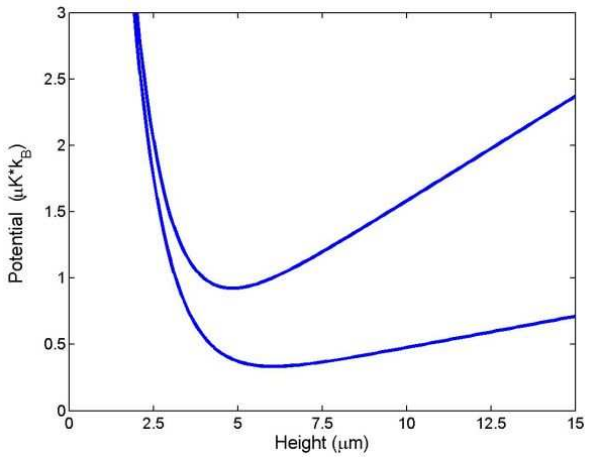

Figure 2.1: Vertical potential with full gravitation ($\tilde{g} = g$, upper curve) and with partial levitation ($\tilde{g} = 0.3\,g$, lower curve).

Figure 2.1 shows the potential as a function of the height above the prism for unlevitated ($\tilde{g} = g$) and partially levitated ($\tilde{g} = 0.3\,g$) conditions. In both cases, the optical potential at the surface is $20\,\mu\mathrm{K} * \mathrm{k_B}$ and the decay length of the evanescent wave is set to $2\,\mu$m. A comparison of the two curves makes clear that partial levitation reduces the compression of the trap and shifts the minimum position to larger heights.

2.2 Wedge potential at high temperatures

Let us first consider the trajectory of an atom with an upper turning point lying high above the prism surface, by far out of reach for the evanescent wave. Gravity then accelerates the atom downwards, and it obtains a large velocity before its impact on the evanescent wave. The strong repulsive force of the evanescent light field decelerates the atom quickly. After stopping deep inside the evanescent wave, the atom turns around and is launched up high again.

Such conditions will prevail when the typical thermal bouncing height $k_B T/(m\tilde{g})$ greatly exceeds the decay length $\Lambda/2$ of the evanescent-wave potential. This is equivalent to comparing the thermal energy to the energy scale $m\tilde{g}\Lambda/2$. As an example, cesium atoms at a temperature of $10\,\mu$K typically reach a height of $63\,\mu$m above the surface without levitation ($\tilde{g} = g$), which is much larger than $1\,\mu$m, the typical value for the decay length $\Lambda/2$. The same is true for an ensemble at $1\,\mu$K, when the effective gravitational acceleration $\tilde{g}$ is reduced by a factor of 10 using an appropriate magnetic levitation gradient.

Since the atom leaves the evanescent light field completely, the motion can be described in two parts. When the atom falls down from its upper turning point, the force of the evanescent wave can be neglected, and the atom only feels the constant acceleration of gravity. On the other hand, when the atom approaches its lower turning point,

the optical force dominates and the linear potential of gravity is negligible. The intermediate region, where both potentials contribute, is passed through quickly and plays little role.

The atom spends most of its time high above the surface in the field of gravity alone, whereas the duration of its interaction with the evanescent wave during a bounce is comparatively short. Thus it is a useful approximation to replace the evanescent wave potential by a hard potential wall that acts as an atom mirror. Together with the linear potential of gravity, the total potential has the shape of a wedge.

The density profile of a thermal cloud in a wedge potential is proportional to the Boltzmann factor $\exp(-m\tilde{g}z/(k_BT))$, so the density rises exponentially with decreasing height. The maximum value n_0 is reached at the position of the atom mirror close to the surface, below which the density drops to zero.

$$n(z) = n_0 \exp\left(-\frac{m\tilde{g}z}{k_BT}\right) \tag{2.2}$$

An atom launched upwards from the mirror at a velocity v_0 returns after the time $2v_0/\tilde{g}$, so the bouncing rate is $\nu = \tilde{g}/2v_0$. For example, at $10\,\mu$K the thermal velocity $v_0 = \sqrt{2k_BT/m}$ is 3.5 cm/s, which results in a bouncing rate of 140 Hz for $\tilde{g} = g$. When cooling the sample, the bouncing rate increases to a few hundred Hertz before the approximation of using the wedge-shaped potential becomes questionable.

2.3 Harmonic potential at low temperatures

When the atoms are cold enough, they stay in the vicinity of the potential minimum and the harmonic approximation can be applied. The atoms perform harmonic oscillations at a frequency $\omega/2\pi$ around the equilibrium position z_m. From equation 2.1 we derive the values

$$\omega = \sqrt{\frac{2\tilde{g}}{\Lambda}} \tag{2.3}$$

$$z_m = \frac{1}{2}\ln\left(\frac{2U_0}{m\tilde{g}\Lambda}\right) \tag{2.4}$$

and write down the potential in the harmonic approximation:

$$U = m\tilde{g}z_m + \frac{m\tilde{g}\Lambda}{2} + \frac{1}{2}m\omega^2(z - z_m)^2 \tag{2.5}$$

As for all harmonic traps, the density distribution of a thermal gas has a Gaussian shape centered around the position of the potential minimum. At temperature T and peak density n_0 the density distribution reads

$$n(z) = n_0 \exp\left(-\frac{m\omega^2}{2k_BT}(z - z_m)^2\right) \tag{2.6}$$

The harmonic approximation will be valid as long as the typical thermal amplitude of oscillations $\sqrt{k_BT/(m\omega^2)}$ is small compared to the decay length $\Lambda/2$ of the evanescent-wave intensity. Using equation 2.3 for ω, this is equivalent to comparing the thermal energy k_BT to the same energy scale $m\tilde{g}\Lambda/2$ as already introduced in section 2.2. Equation 2.5 shows that this characteristic energy scale is in fact the optical potential energy at the equilibrium height z_m.

2.4 Anharmonic corrections

With the energy scale $m\tilde{g}\Lambda/2$ limiting the temperature range of harmonic trapping it becomes clear that a partially levitated trap with reduced $\tilde{g}$ will only reach the harmonic regime at extremely low temperatures. With $\Lambda = 3\,\mu$m, the temperature should be below 240 nK in an unlevitated trap, while levitation at $\tilde{g} = 0.15g$ requires temperatures below 40 nK for harmonic trapping. As a consequence, anharmonic corrections gain importance when magnetic levitation is used.

While slow atoms perform symmetric oscillations around the equilibrium position, faster atoms undergo anharmonic oscillations. They experience an increased restoring force close to the surface and a reduced restoring force when they begin to leave the evanescent-wave at larger heights. A thermal gas then has an asymmetric density profile with reduced peak density. We now calculate these effects by taking into account higher orders in the power series of the trapping potential.

Introducing the dimensionless height $x = 2z/\Lambda$ and shifting the origin of potential and position to the location of the potential minimum, we can write the exact potential 2.1 in the form

$$U = \frac{m\tilde{g}\Lambda}{2}\left(e^{-x} + x - 1\right) \tag{2.7}$$

Hence the power series of the potential is the exponential series with the constant and linear terms omitted:

$$U = \frac{m\tilde{g}\Lambda}{2}\left(\frac{x^2}{2} - \frac{x^3}{6} + \frac{x^4}{24} - \frac{x^5}{5!} + \frac{x^6}{6!} \mp \dots\right) \tag{2.8}$$

When introducing the dimensionless temperature $\epsilon = k_BT/(m\tilde{g}\Lambda/2)$, the density profile of a thermal cloud can be expressed as

$$n = n_0 \exp\left(-\frac{x^2}{2\epsilon}\right)\exp\left(\frac{x^3}{6\epsilon} - \frac{x^4}{24\epsilon} + \frac{x^5}{5!\epsilon} - \frac{x^6}{6!\epsilon} \pm \dots\right) \tag{2.9}$$

For small temperatures $\epsilon \ll 1$, the density profile is mainly given by the first exponential factor describing the Gaussian shape of a harmonically trapped ensemble. Within

the range of this Gaussian, the second exponential factor is close to one. It includes the corrections to the Gaussian profile due to the anharmonicity of the trapping potential. By expansion of the second exponential we get

$$n = n_0 \exp\left(-\frac{x^2}{2\epsilon}\right)\left(1 + \frac{x^3}{6\epsilon} - \frac{x^4}{24\epsilon} + \frac{x^5}{5!\epsilon} - \frac{x^6}{6!\epsilon} + \frac{x^6}{72\epsilon^2} \pm \dots\right) \tag{2.10}$$

2.4.1 Peak density

Let us now use the result 2.10 to calculate the anharmonic correction to the peak density n_0. Integrating over the Gaussian profile without the correction factor leads to $n_0^h = (2N/\Lambda)(2\pi\epsilon)^{-\frac{1}{2}}$, which is the value for the peak density in the harmonic approximation when N atoms are in the trap. In order to evaluate the corrections we need to deal with integrals of the form $\int_{-\infty}^{\infty} x^n \exp\left(-x^2\right) dx$. For uneven powers n the whole integrand is an uneven function, and therefore the integral vanishes. For even powers $n = 2m$, the integral can be calculated using the Gamma-function:

$$\int_{-\infty}^{\infty} x^{2m} \exp\left(-\frac{x^2}{2\epsilon}\right) dx = (2\epsilon)^{m+\frac{1}{2}}\ \Gamma(m + \frac{1}{2}) \tag{2.11}$$

We see that the leading corrections in 2.10 are due to the terms $-\frac{x^4}{24\epsilon}$ and $\frac{x^6}{72\epsilon^2}$:

$$N = n_0 \frac{\Lambda}{2} \sqrt{2\pi\epsilon}\left(1 - \frac{1}{8}\,\epsilon + \frac{5}{24}\,\epsilon \pm \dots\right) \tag{2.12}$$

Neglecting higher orders, the peak density is

$$n_0 = \frac{n_0^h}{1 + \frac{\epsilon}{12}} \tag{2.13}$$

where the harmonic result is modified by the anharmonic correction factor $\left(1 + \frac{\epsilon}{12}\right)^{-1}$. Although the derivation of this result was based on the assumption of small temperatures $\epsilon \ll 1$, it is surprisingly accurate even for higher temperatures. By comparison with the numerically evaluated exact peak density, the approximation 2.13 is found to deviate by at most one per mil in the range $0 \le \epsilon \le 2$ and at most three per cent in the range $0 \le \epsilon \le 5$.

For $\epsilon = 1$, the peak density is reduced by 8 per cent, which might be noticeable in some experiments.

2.4.2 Asymmetry

Besides the reduction in peak density, the anharmonicity of the potential also leads to an asymmetric density distribution. As a measure of asymmetry we define the parameter

$$\alpha = \frac{N^+ - N^-}{N} \tag{2.14}$$

where N^+ is the number of particles above the height of the potential minimum, and N^- counts the particles sitting below the minimum. Thus we get

$$\alpha = \frac{\Lambda}{2N}\left(\int_0^\infty n\, dx - \int_{-\infty}^0 n\, dx\right) \tag{2.15}$$

Plugging in the formula 2.10 for the density distribution n, we see that now the even powers in the expansion cancel out. The remaining integrals involving x^{2m+1} with integer m are evaluated using the Gamma function:

$$2\int_0^\infty x^{2m+1} \exp\left(-\frac{x^2}{2\epsilon}\right) dx = (2\epsilon)^{m+1}\, m! \tag{2.16}$$

The leading contribution to α comes from the term $\frac{x^3}{6\epsilon}$ in 2.10, and gives

$$\alpha = \frac{\Lambda n_0 \epsilon}{3N} \tag{2.17}$$

To lowest order, we can replace the peak density n_0 by its harmonic value $n_0^h = (2N/\Lambda)(2\pi\epsilon)^{-\frac{1}{2}}$ and obtain the result

$$\alpha = \frac{2}{3\sqrt{2\pi}}\sqrt{\epsilon} \tag{2.18}$$

which is approximately $\alpha = 0.266\sqrt{\epsilon}$. By comparison to an exact numerical calculation, the accuracy of the formula 2.18 is found to be better than 7 per mil in the range $0 \le \epsilon \le 1$.

2.5 Photon scattering rate

A crucial quantity for optical atom traps is the rate of photon scattering Γ_{sc}. For far detuned traps [Gri00], where the detuning δ is much larger than the transition linewidth Γ, the scattering rate is related to the dipole potential U by

$$\Gamma_{sc} = U\frac{\Gamma}{\hbar\delta} \tag{2.19}$$

Therefore one needs to calculate the average dipole potential that the atoms see while moving around in the trap.

In the high temperature limit, the average optical potential is the product of the bouncing rate and the time-integrated optical potential for a single bounce. At an impact velocity v, the bouncing rate is $\tilde{g}/(2v)$, while the integrated potential of a bouncing event can be shown [Söd95] to be $mv\Lambda$. The average optical potential is then

$$\bar{U} = \frac{m\tilde{g}\Lambda}{2} \tag{2.20}$$

This result is independent of the velocity v and therefore the photon scattering rate does not depend on the temperature of the atomic gas. When the temperature is reduced, the atoms bounce more frequently on the evanescent wave, but each impact is less hard, and so the average dipole potential remains the same.

Although this interpretation is only possible in the high temperature limit, we will show now that result 2.20 is truly independent of the temperature, i.e. it also holds in the medium temperature range and in the low temperature limit. The latter case is easy to verify, since $m\tilde{g}\Lambda/2$ is the optical potential at the minimum of the total potential 2.1. The gradient of the optical potential does not change the average value for a harmonic oscillation, because the motion is symmetric around the minimum. For asymmetric oscillations with larger amplitudes, higher orders come into play, and it is less straight-forward to see whether the average potential changes or not.

Let the atomic motion start at time t_0 at the lower turning point inside the evanescent wave at position z_0, and denote the time and position of the upper turning point by t_1 and z_1. It is sufficient to consider half of an oscillation period. Therefore, by definition, the average potential is

$$\bar{U} = \frac{1}{t_1 - t_0} \int_{t_0}^{t_1} U_0 \exp\left(\frac{-2z(t)}{\Lambda}\right) dt \tag{2.21}$$

where $z(t)$ is the unknown solution for the atomic motion. We transform the integral substituting t by z using $dz = \dot{z}\, dt$.

$$\bar{U} = \frac{1}{t_1 - t_0} \int_{z_0}^{z_1} U_0 \exp\left(\frac{-2z}{\Lambda}\right) \frac{dz}{\dot{z}} \tag{2.22}$$

The conservation of the energy E gives a first integral of the equation of motion, and we can express the velocity $\dot{z}$ as a function of z

$$\dot{z} = \sqrt{\frac{2}{m}\left(E - m\tilde{g}z - U_0 \exp\left(\frac{-2z}{\Lambda}\right)\right)} \tag{2.23}$$

Separation of variables leads to

$$t_1 - t_0 = \sqrt{\frac{m}{2}} \int_{z_0}^{z_1} \left(E - m\tilde{g}z - U_0 \exp\left(\frac{-2z}{\Lambda}\right)\right)^{-\frac{1}{2}} dz \tag{2.24}$$

Inserting equations 2.23 and 2.24 into 2.22 gives an integral expression for the average potential $\bar{U}$. The expression can be simplified by expanding the numerator in the following way:

$$\bar{U} = \frac{1}{t_1 - t_0} \int_{z_0}^{z_1} \frac{\frac{\Lambda}{2}\left(\frac{2}{\Lambda} U_0 \exp\left(\frac{-2z}{\Lambda}\right) - m\tilde{g}\right) + \frac{m\tilde{g}\Lambda}{2}}{\sqrt{\frac{2}{m}\left(E - m\tilde{g}z - U_0 \exp\left(\frac{-2z}{\Lambda}\right)\right)}} dz \tag{2.25}$$

We then evaluate the integral:

$$\bar{U} = \frac{\Lambda}{t_1 - t_0} \sqrt{\frac{m}{2}} \left[\sqrt{E - m\tilde{g}z - U_0 \exp\left(\frac{-2z}{\Lambda}\right)} \right]_{z_0}^{z_1} + \frac{t_1 - t_0}{t_1 - t_0} \frac{m\tilde{g}\Lambda}{2} \tag{2.26}$$

The first term is zero as the velocity vanishes at the turning points. Finally, we arrive at

$$\bar{U} = \frac{m\tilde{g}\Lambda}{2} \tag{2.27}$$

In conclusion, the average optical potential that is seen by an atom bouncing on an evanescent wave is always $m\tilde{g}\Lambda/2$, and it does not depend on its energy. This result is a special property of the potential 2.1 and it holds not only in the high energy limit, but also in the general case.

It is also remarkable that, as long as the evanescent wave is strong enough to reflect the atoms, the average optical potential does not depend on the intensity of the evanescent wave. The laser power used for the evanescent wave determines the height of the potential barrier to the surface and the position of the potential minimum, but has no effect on the value of the optical potential in the minimum.

As a numerical example we consider an evanescent wave with decay length $\Lambda = 1.5\,\mu$m ($\Delta\theta = 0.3^\circ$) and without magnetic levitation ($\tilde{g} = g$), and obtain an average optical potential $\bar{U} = 119\,$nK. Assuming a detuning of 2 nm, i.e. $\delta = 830\,$GHz, formula 2.19 gives a photon scattering rate $\Gamma_{sc} = 0.1\,\mathrm{s}^{-1}$. It is clear that a reduction of the effective constant of gravity $\tilde{g}$ by a certain factor will reduce the average optical potential and consequently the photon scattering rate by the same factor.

2.6 Quantum effects

So far, we have discussed the atomic motion in the trapping potential in an entirely classical way. However, the main interest in ultracold gases arises from the importance of quantum mechanical effects in such systems. Hence we now turn to the question of where the classical description fails and the quantum world begins.

In general, a system in a thermal mixture of many quantum states can be expected to behave classically. The observation of quantum effects then requires a reduction in temperature until only few states remain energetically available. In our specific case, we start with a classical thermal gas in the wedge-shaped potential (see section 2.2) and after substantial cooling enter into the harmonic trapping regime (see section 2.3) where we approach the quantum world. Although it is possible to solve the quantum mechanical problem of motion in a wedge potential [Wal92], we thus readily restrict the discussion to the more familiar case of a harmonic trap.

Zero-point motion and reduced dimensions

A peculiarly simple quantum effect is already present for a single trapped particle. Because the trap constrains the spatial extent of the wavefunction, the uncertainty principle requires a non-zero minimum kinetic energy. This kinetic energy of the quantum mechanical ground state gives a lower bound for the release energy which can be extracted from expansion measurements of ultracold gases. In an anisotropic trap, continuous cooling leads to correspondingly reduced kinetic energies in the weakly confined directions, while the kinetic energy in the tightly confined direction finally levels off when it reaches its minimum value [Gör01, Ryc04b]. A related well-known quantum effect is the discrete spectrum of excited states in a trap, with a constant energy-level spacing of $h\nu$ for a harmonic trapping frequency ν. When the thermal energy is not sufficient to provide a single vibrational excitation quantum ($k_B T < h\nu$), the tightly confined oscillation will remain in its ground state. As long as the energy of the vibrational energy quantum dominates all other energy scales of the system, any dynamics will be restricted to the weakly confined directions. This phenomenon of 'freezing' a degree of freedom and the effective formation of a lower-dimensional system demands high trapping frequencies and low temperatures. At a frequency of 1 kHz for the tightly confined direction, a thermal gas enters the two-dimensional regime at temperatures below 50 nK.

Interactions

When two atoms approach each other, they interact via the same strong interatomic potentials at short distances (< 1 nm) which are responsible for chemical bonds. The scattering problem is simplified by the large deBroglie wavelength of ultracold atoms, which is typically much larger than the range of strong interactions [Wei99]. Elastic scattering is then completely characterized by a single parameter, the s-wave scattering length a. The theoretical treatment of scattering processes relies heavily on quantum mechanical concepts and is by far outside the scope of classical theories. Therefore, collisional effects like thermalization due to elastic collisions as well as heating and trap loss due to inelastic collisions should be viewed as quantum phenomena. This becomes particularly clear when pronounced scattering resonances appear as indications of weakly bound molecules [Ino98, Kra06b], which are fascinating quantum objects.

Under normal conditions the external trapping potential has no effect on atomic interactions. Even a two-dimensional gas with the tightly confined motion in its ground state will exhibit ordinary three-dimensional scattering properties, unless extremely tight confinement and large scattering lengths are realized. As a condition for modified scattering, the scattering length needs to exceed the harmonic oscillator length in the tightly confined direction [Pet00, Bou02]. The external potential then also deforms weakly bound molecules and affects the associated scattering resonances.

Although interacting thermal gases do exhibit pronounced quantum effects, even more dramatic quantum phenomena and a direct visualization of quantum mechanical concepts are attainable in Bose-Einstein condensates.

Bose-Einstein condensation

A sufficiently cold and dense thermal Bose gas undergoes a phase transition that produces a macroscopic population of the ground state. Condensation into the ground state sets in when the atomic wavefunctions start to overlap, i.e. when the thermal de-Broglie wavelength becomes comparable to the spacing between particles. This phase transition yields a macroscopical ground-state wavefunction although the thermal energy might still greatly exceed the vibrational level spacing of the trap [Pet02, Pit03].

Bose-Einstein condensation occurs as a consequence of the quantum statistical properties of identical bosons, and not because of interactions. However, as the atomic wavefunctions are permanently overlapping, interactions have a strong effect on the shape and behavior of the condensates. A very successful approach describes the impact of interactions in a mean-field picture, where all atoms share the same wavefunction but are affected by an interaction energy proportional to the local density. This approach yields the Gross-Pitaevskii equation, which takes the form of a non-linear Schrödinger equation [Pit03]. Since the advent of condensates about a decade ago, a wealth of phenomena has been observed, e.g. related to matter-wave coherence, superfluid flow and collective excitations, and many impressive pictures of the quantum world have been obtained [Sou02].

With respect to two-dimensional systems, it is important to realize that the interactions in a condensate provide another energy scale, the chemical potential μ. A two-dimensional description of a Bose-Einstein condensate therefore requires the chemical potential to be smaller than the vibrational energy quantum in the tightly confined direction. This condition then guarantees that the 'frozen' direction is not excited via the available interaction energy. The restricted dimensionality can lead to qualitatively different behavior of the condensate [Pri04] and modifies the coherence properties [Pet00, Det01].

3 Vacuum System

Experiments with ultracold gases are performed with trapped ensembles within a vacuum system. It is necessary to remove the thermal background gas in order to avoid loss that is caused by collisions of fast background atoms with the cold trapped gas. With standard vacuum technology, ultra-high vacuum (UHV) conditions at pressures in the range of 10^{-11} mbar are achievable and permit trapping times of tens of seconds.

3.1 Glass cell with integrated prism

In this chapter, we start with a glance at the preexisting stainless steel chamber and its shortcomings, and then describe the new approach which is based on a large glass cell. A special issue is the integration of a custom-made superpolished prism into the cell.

3.1.1 Stainless steel chamber

Our surface trapping experiment was started about a decade ago [Ovc97] in Heidelberg, where the first versions of the vacuum system were built [Man99]. Later, the whole experiment was transported to Innsbruck [Ham02a, Ryc04a]. The main components of this setup are shown in Fig.3.1.

An effusive beam of cesium atoms was produced in the oven section, and then used to load the optical traps in the main chamber. The various pumps were needed in order to maintain the ultra-high vacuum in the main chamber, where all the experiments were performed. The chamber was made of stainless steel, had a spherical shape and provided optical access through as many as 16 viewports. It was originally designed as a multi-purpose chamber with no special dedication to surface experiments. The prism was installed on a holder in the center of the chamber. Magnetic fields were generated outside of the vacuum by coils mounted around the viewports, and some coils were even loosely wound directly on the chamber walls.

The old apparatus enabled us to perform experiments with thermal atoms in sophisticated surface traps [Ham03], and after tedious optimization procedures, we could even produce a small Bose-Einstein condensate of cesium [Ryc04b]. However, it was evident that we had pushed the apparatus to its limit. In detail, we encountered the following technical problems:

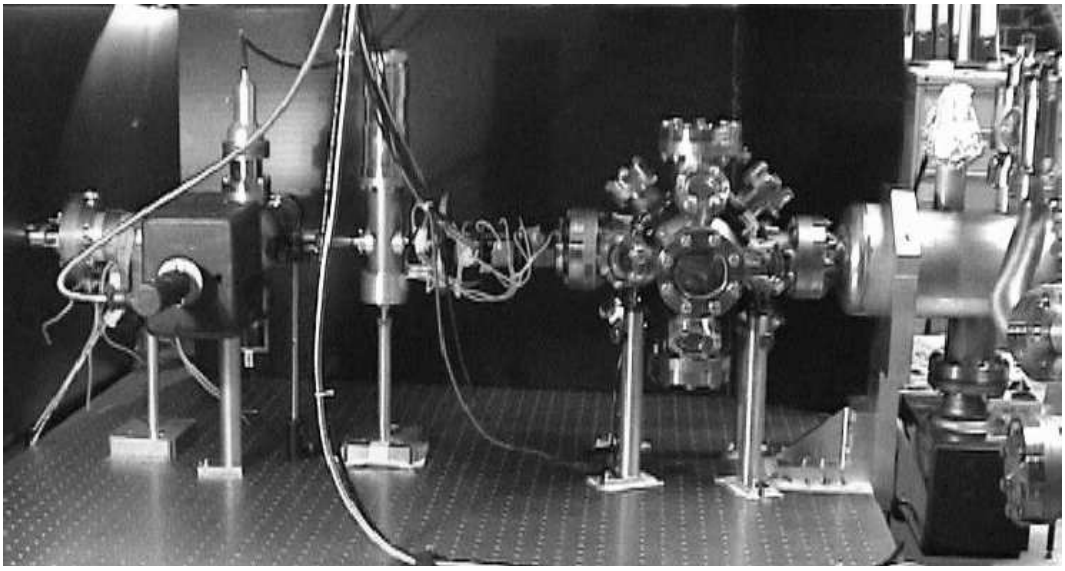

Figure 3.1: Old vacuum setup. From left to right: Oven, pumping cross, valve, Zeeman slower, main chamber, pumping section.

- Limited optical access. All of the viewports were occupied, and it became more and more difficult or even impossible to feed another laser beam through them. Despite the many viewports, a large fraction of the solid angle around the position of the atoms was blocked by the stainless steel walls of the chamber. An implementation of additional optical cooling stages, e.g. Raman sideband cooling, was simply not possible. There was no space to install an absorption imaging system for the top-view, either.

- Poor magnetic field control

  - Slow switching. The occurrence of eddy currents in the steel walls of the chamber inhibited fast ramps of the magnetic fields. The typical timescale for switching the magnetic fields was a few ms.

  - Sloppy coil construction. Due to space restrictions, the levitation coils were wound directly onto the chamber, without housing and water cooling. We could not levitate the atoms for extended periods of time, e.g. during a long evaporation ramp.

- Prism design. Only two of the four side faces of the prism were polished. The implementation of a surface lattice with orthogonal, counter-propagating evanescent waves was not feasible. Also, we believed that the surface quality of the top side could be improved by state-of-the-art superpolishing.

3.1.2 Glass cell

The restrictions imposed by the old steel chamber were so severe that we felt it was high time for a major reconstruction. The long-standing idea was to replace the bulky steel chamber by a glass cell without changing too much of the rest of the system. But in practice, some changes implicated the next ones and also, analyzing the old scheme, we found more and more things to improve. In the end, it turned out that instead of replacing some parts of the old setup, we had built up a completely new system while recycling some of the old parts.

In our traditional steel chamber, the prism was mounted on a titanium holder that stood on the bottom viewport. When replacing the steel chamber by a glass cell, the first basic question is: how do you integrate a prism into the glass cell?

It is possible to use a standard glass cell and simply put the prism inside, not necessarily using a holder [Col03]. The laser beams for the evanescent waves then pass the cell walls before and after the prism, leading to reflections and stray light. Uncoated cell walls might also impose etalon effects on the beams. It should be noted that the inner cell walls cannot be coated as the coatings do not stand the high temperatures involved in the direct fusion technique, which is needed to assemble cells of high optical quality.

A better approach would be to create the evanescent wave directly on the inner glass surface of one of the cell walls. With a standard cell, this could be achieved by optically contacting a prism to the outside of a cell wall. The light is then coupled in through the prism, but the evanescent wave is formed directly on the cell wall. A similar idea is to order a custom-made cell that directly incorporates a prism in one of the walls. However, the manufacturer of our cells[1] warned us with respect to the achievable surface quality. Obviously, the inner surfaces of the cell are not accessible for polishing after assembly. Starting with a superpolished surface, there are so many following steps in the production process, that the manufacturer was not willing to guarantee the highest surface quality in the end.

In order to avoid any compromise on surface quality, it is advantageous to buy a highly polished prism, test its quality, and integrate it into the cell as a last step in the assembly procedure. As a simple and versatile method, one can use an epoxy resin to glue the prism to the cell. However, using glue in ultra-high vacuum experiments is not common practice as the evident questions of leakage and outgassing need careful consideration.

Test setup

The encouraging performance of glued cells developed in the atomchip community [Du04] made epoxy seals appealing for our application. For the purpose of testing different epoxies and learning how to handle them, a small UHV chamber was set up

[1] Hellma GmbH & Co. KG, Müllheim/Baden, Germany

in addition to several cheap glass cells with glued contacts. The test chamber also served as a playground where I could gain experience in vacuum technology.

Figure 3.2: Test chamber with glued glass cell.

The chamber consists of a six-way cross with all the pumping capabilities needed for achieving UHV conditions, i.e. there is a small ion pump (20 l/s), a titanium sublimation pump, and the option to attach a turbo pump via an angle valve. Another angle valve separates the pumping cross from the actual testing section that is made of a T-piece with a UHV gauge on one side and the glued glass cell to be tested on the opposite side. The setup lends itself to two measuring methods. In the first case, one closes the valve to stop pumping and observes the pressure rise in the testing section. In the second case, the steady state pressure with open valve is measured. The second method is only suited for calculating the rate of leakage and outgassing if the actual pumping speed is known.

To achieve this, we have reduced the pumping speed by introducing a copper disc with a bored hole of 8.5 mm diameter between the valve and the T-piece. The copper disc[2] also seals the CF-connection, i.e. it replaces the usual ring-shaped copper gaskets. We found this technique simple and effective and therefore also used it later in the main setup for differential pumping (see section 3.2.1). The reduction of the pumping speed also ensures that the pressure at the position of the gauge equals the pressure in the glued glass cell, since the connecting tubes are much larger than the pumping hole.

The test cells are cheap commercial cells[3], with a round hole in one of the sides. A Pyrex-to-metal transition is then glued to this bored side. On the opposite side, another epoxy seal is used to attach the top cover of the cell. The overall length of the epoxy seals is about 20 cm. We have tested two different epoxies: VacSeal II and Epotek 353 ND.

VacSeal II is a version of the well-known leak sealant VacSeal, but features a higher viscosity. It can be used for cementing glass pieces together and should stand

[2]Blank copper gasket, Vacuum generators order code ZCUB38
[3]Hellma 'Large Cells'

high bakeout temperatures. After gluing the cell, we cured it at 260 °C for one hour, and then integrated it into the test setup. We could not reach pressures below 1.3×10^{-7} mbar after several days of pumping with a turbo pump. Baking out the chamber at 200 °C didn't lead to lower pressures, either. A Helium leak-test finally showed that the epoxy seal was not leak-proof, and therefore VacSeal II was not appropriate for our purposes.

Epotek 353 ND is a readily available two-component epoxy, and was approved by the NASA for low outgassing[4]. It stands temperatures higher than 200 °C and can be cured at moderate temperatures. We glued a new cell and heated it up to 100 °C for ten minutes, with the epoxy showing an amber color change upon cure. After attaching the cell to the test setup and turning on the turbo pump, we performed a helium leak-test again. This time, no signs for leakage from the epoxy seals were found. A week of pumping led to a pressure of 4×10^{-9} mbar. We then baked the whole setup at 180 °C for a few days and reached a final pressure of 1.5×10^{-10} mbar.

It is remarkable that the Epotek seals can be baked at temperatures higher than 100 °C, because the glue undergoes a phase transition at this temperature, leading to a reduced bonding strength and a much higher coefficient of thermal expansion. We just gave it a try - and it worked. The cell even endured a high temperature test at 250 °C for 12 hours.

In order to check for leakage through the seals, we stopped pumping by closing the angle valve and observed the pressure rise. While closing the valve within a minute, the pressure quickly increased from 1.5×10^{-10} mbar to 1.1×10^{-9} mbar. Then, during the next hour, we observed a slow linear rise of the pressure to 3.6×10^{-9} mbar. With the volume of the testing section given by 0.25 l, the rate of pressure rise indicates a minuscule gas load of 1.8×10^{-13} mbar l/s. Generally speaking, any gas load stems from leakage and outgassing. While the rate of outgassing strongly depends on the pressure range, the leak rate should be constant (unless approaching atmospheric pressure) and is always present. We therefore conclude that leakage from the epoxy seals is completely negligible, i.e. the sealing performance of Epotek 353 ND is perfect.

The final pressure that can be reached is then limited by the amount of outgassing from the epoxy. In the measurement of the rate of pressure rise, we could not record the initial rise as it happened too fast. We therefore extract the rate of outgassing from the final steady-state pressure 1.5×10^{-10} mbar in combination with the known pumping speed. For most gases, the pumping speed of the cross exceeds the vacuum conductance of the bored copper disc, which then limits the pumping speed to the testing section. For air, the conductance of the hole [O'H03] with diameter 8.5 mm is 6.6 l/s. Lighter gases are pumped at a higher speed because the conductance of the hole gets larger for higher thermal velocities. Noble gases are only pumped by the ion pump, and the pumping speed is only about 10% of the nominal 20 l/s, and so the bored copper disc plays no role in this case. We do not know what kind of gas species

[4] http://outgassing.nasa.gov/

are involved in the outgassing of the epoxy, but assuming the same pumping speed as for air leads to the value 9.9×10^{-10} mbar $\times$ l/s for the gas load.

The exact knowledge of the absolute value of the gas load is not really important when estimating the final pressure that will be reached in the real experiment. If the pumping speed of the test setup (deliberately reduced by the bored copper disc) can be improved by a certain factor, one would expect the final pressure to drop by the same factor. This would be true for a constant gas load. In reality, however, it is not as simple as that. Whenever the pressure falls below the saturation pressure of another substance, the gas load increases, so there is no simple relation between pumping speed and steady-state pressure. Hence, the extrapolation to lower pressures is questionable, especially over large pressure ranges. In our case, 1.5×10^{-10} mbar was not so far away from the desired pressure of a few times 10^{-11} mbar, and we were confident to improve the pumping speed by more than an order of magnitude (to 80 l/s, see section 3.1.2).

In conclusion, the test setup revealed that Epotek 353 ND features excellent sealing properties, and that its outgassing load is acceptable as long as no compromise on the pumping speed is made.

Glass cell with round hole

The performance of the epoxy seals in the test setup convinced us to use the same technique in the real experiment. We designed a prism with a round pedestal and a glass cell with a round hole, and later assembled the parts using an epoxy seal.

The glass cell was manufactured by Hellma[5] in a direct fusion process. In contrast to glass blowing techniques, this process works with temperatures well below the melting point of the glass and preserves the high optical quality of the cell walls. Thus, the center part of the cell consists of four polished rectangular, parallel plates made of high-quality fused-silica (Spectrosil). The outer dimensions are 238 mm $\times$ 45 mm $\times$ 60 mm, and the walls are 4 mm thick. At its center, one of the sides has a round hole with a diameter of 48 mm. The cell is open on both ends, where CF63-flanges are attached via glass-to-metal transitions[6]. Attempts of a glass-blowing company to directly connect the glass-to-metal transitions to the cell failed, so finally the attachment was done by Hellma using small adapter pieces and the direct fusion process. The adapter plates have a round aperture with a diameter of 35 mm. On each side, the tubing of the transition glasses is about 140 mm long and 64 mm in diameter.

The overall pumping speed at the position of the prism is geometrically limited by the vacuum conductances of the cell, the orifice of the adapter pieces and the tubing of the glass-to-metal transitions (with adjoining bellows). The three contributions are approximately equal, and give a total vacuum conductance of 40 l/s to either side, assuming air at room temperature as the gas load. Note that vacuum conductances are smaller for heavier gases, and that the pumping speed of noble gases is not limited by the geometrical conductances but rather by the performance of the pumps.

[5] Hellma GmbH & Co. KG, Müllheim/Baden, Germany
[6] Larson Electronic Glass, Redwood City, CA, USA

3.1.3 Superpolished Prism

A crucial point for our surface trap is the quality of the polishing, since defects cause stray light that reduces the lifetime of the trapped atoms. In addition, interference of stray light with the evanescent wave can lead to unwanted distortions of the trapping potential. Stray light emerges not only from localized defects, but also from the surface roughness. By interference, the surface roughness then introduces roughness to the evanescent wave mirror [Hen97].

Our new prism was custom-made by Research Electro-Optics, Inc.[7] The design with dimensions in mm is shown in figure 3.3. The specifications are as follows:

- The prism was manufactured out of a single piece of quartz, no optical contacting of the round pedestal was necessary. The high-quality fused-silica material is specified as 'Dynasil 1101 or equivalent'.
- The superpolished area at the center of the round pedestal (S2) has a surface quality of 5/2 scratch/dig or better (0/0 typical). Surface roughness is below 1 Angstrom RMS. Surface flatness is Lambda/20 (within the 10 mm diameter). The whole surface was superpolished, but only for the central region are the specifications guaranteed.
- Around the pedestal, there is an unpolished annular region with a surface roughness below 10 μm. This surface is to be glued to the glass cell, and the roughness doesn't adversely affect the epoxy seal.
- The top (S2) and bottom (S1) surface are parallel within 0.01 degrees. Overall surface flatness is better than $1/4$ wave.
- The bottom surface (S1) is polished to 10/5 scratch/dig. It is the only coated surface. The AR-coating provides a reflectivity below 1 per cent over a dual band, 850 ± 10 nm and 1064 ± 5 nm, $0-30$ deg, S- and P-polarization. At normal incidence, the reflectivity should be below 0.2 per cent.
- All four sides are polished to scratch/dig 20/10 with 10/5 on a limited clear aperture. The angle between top and side surfaces is specified to 78.5 ± 0.1 degrees.

Figure 3.4 shows a beam path for the creation of an evanescent wave. The prism angle of 78.5 degrees between top and side faces is chosen for the evanescent-wave laser beams to be incident under Brewster's angle. Therefore, no optical coating on the side faces was necessary. Note that the suppression of reflections under Brewster's angle only works for TM-polarization. In order to maximize the evanescent light field, this polarization was already used in earlier experiments [Ham02a, Ryc04a]. After total internal reflection close to the critical angle at the top surface, the beam exits the

[7] Boulder, Colorado, USA

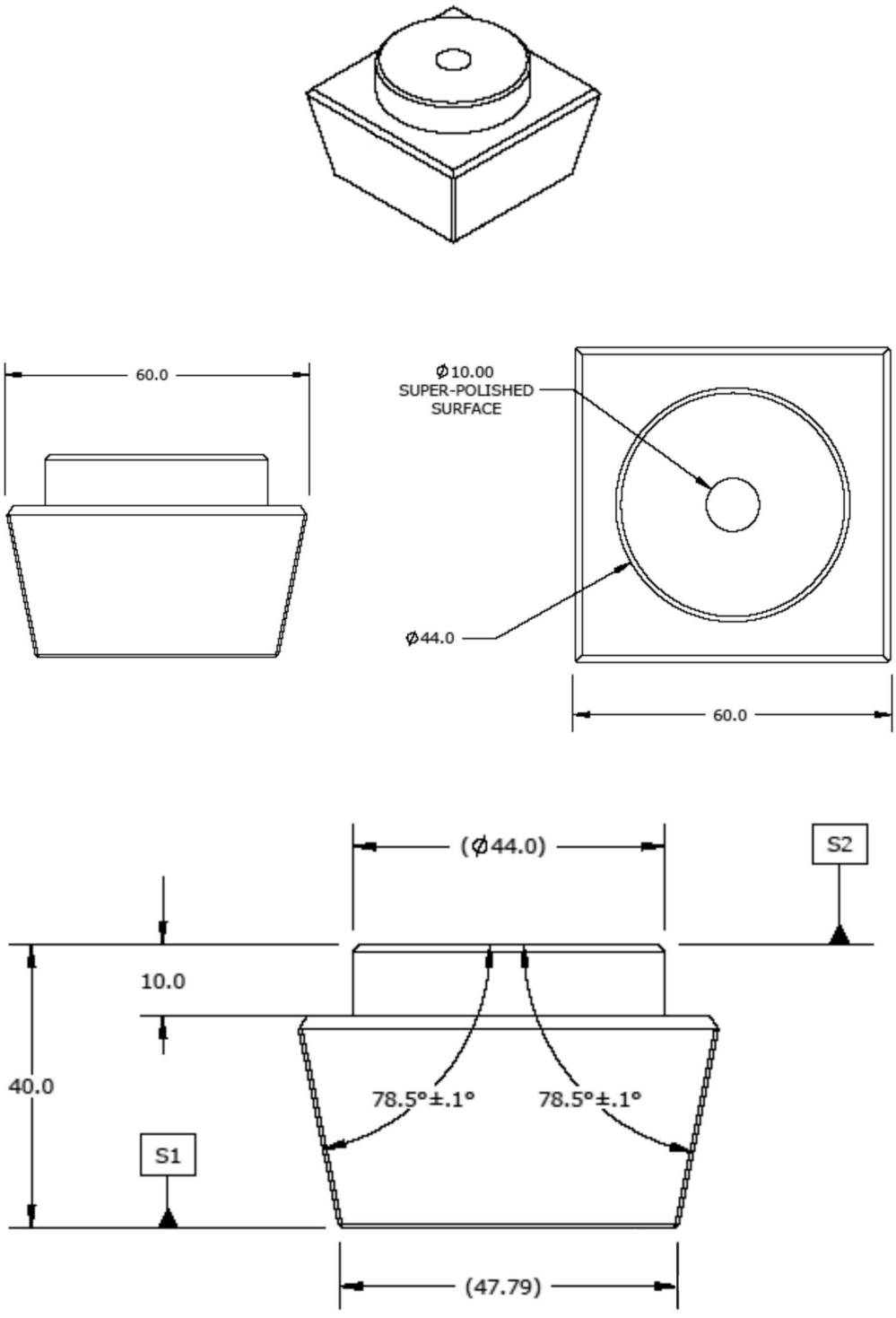

Figure 3.3: Technical drawing of the prism

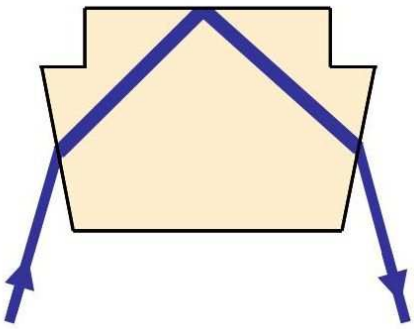

Figure 3.4: A laser beam enters the prism through a side face from below and undergoes total internal reflection at the top surface, before leaving the prism at the opposite side face. Reflections from the side faces are suppressed due to incidence under Brewster's angle.

prism at the opposite side, again under Brewster's angle. A slight disadvantage is that an initially round laser beam will produce an elliptical evanescent-wave spot with an aspect ratio of about 2 : 1. Our former prism geometry with coated sides at an angle of 45 degrees produced a better aspect ratio of $\sqrt{2}$: 1. However, a round spot can be achieved by beam shaping with cylindrical lenses when necessary.

Two new prisms were produced. To test the improvement in surface quality, we sent one of them to Carl Zeiss[8], together with the used prism that we removed from the old stainless-steel chamber. The surface profiles were examined with a white light interferometer[9]. As a result, a substantial improvement in surface quality was confirmed. Figure 3.5 shows typical profiles with a field of view of $200\,\mu\text{m} \times 160\,\mu\text{m}$. For the old prism, surface roughness is determined to be larger than 3 Å RMS and typically more than 20 micron-sized defects with a height difference of over 1 nm are found. For the new prism, surface roughness is less than 1.5 Å RMS and typically less than 5 defects are present. The field of view is smaller than the diameter of our evanescent waves, but it approximately fits the size of a hot thermal atomic cloud. After evaporation, the cloud size is a few tens of microns, and only a subregion of the surface profiles in figure 3.5 will be probed. Fine tuning of the trap position then helps to avoid nearby detrimental surface defects.

Epoxy Seal

The prism and the glass cell were glued together with the epoxy Epotek 353 ND, which was extensively tested before (see section 3.1.2). For assembly, we mounted the glass cell with the round hole facing upwards and applied a thin ring of epoxy around the hole, leaving a distance of a few mm to the edge of the hole. Then the prism was carefully inserted with its pedestal facing downwards. As soon as the rough surface

[8] Oberkochen, Germany
[9] Micromap Promap 512

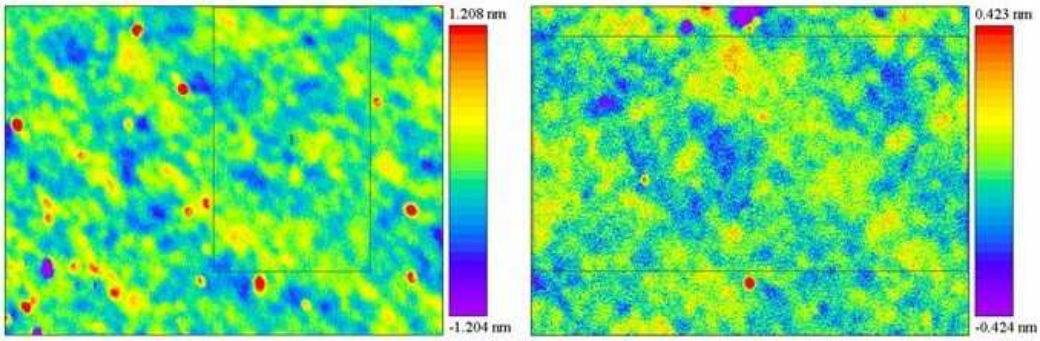

Figure 3.5: Surface profiles obtained with a white light interferometer. Old prism to the left, new prism to the right. Note the different scales of the color bars.

area around the pedestal touched the epoxy ring, the epoxy started to spread out under the weight of the prism. No additional pressure was applied to connect the pieces. On the timescale of an hour, the epoxy slowly diffused to the edge of the hole and then ceased to spread out any further.

It is crucial to use the right amount of epoxy and a suitable viscosity, which we obtained by mixing the two components of the epoxy about one hour before application. The slow curing process at room temperature then increases the viscosity. If the epoxy is too liquid or if too much of it is applied, the epoxy might not stop spreading out at the edge of the hole and flow into the glass cell - leading to an excessive outgassing load. On the other hand, too high of a viscosity or using too small amounts can result in the epoxy not reaching the edge of the hole. Then the vacuum might be affected by the outgassing of air enclosures in between the two glass surfaces. After gaining some experience in the handling of the epoxy, it was not too difficult to obtain the right conditions, and our first try with the real prism and cell worked well. A nice epoxy seal without enclosures was formed, and no epoxy flowed into the cell.

In order to cure the epoxy, we carefully wrapped up the mounted cell in aluminium foil and attached several heating tapes and temperature sensors. We then ramped up the temperature to 80°C within two hours and held it for one hour before slowly letting the cell cool down again.

After the curing process, the epoxy had hardened and showed a slight amber color change as expected. The prism was firmly fixed and we could turn the cell around into its final position, with the prism on the lower side (see figure 3.6. The cell was now ready for integration into the vacuum setup.

3.2 Layout of the vacuum setup

The old vacuum setup (see section 3.1.1) consisted of an oven with pumping cross and valve, a differential pumping tube with surrounding coils for the Zeeman slower, the main steel chamber, and a pumping section. Simply replacing the steel chamber with

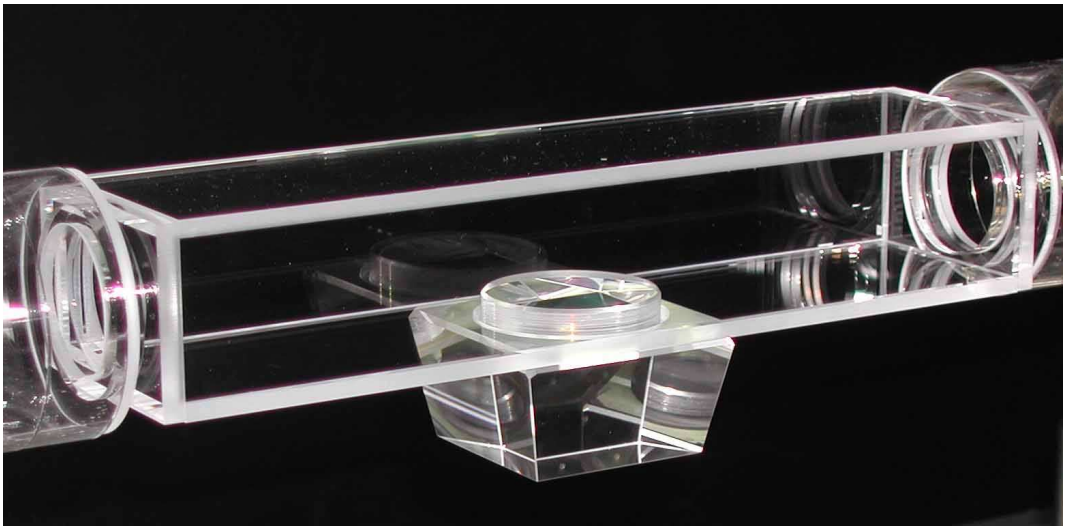

Figure 3.6: Glass cell with integrated prism. The sealing ring of epoxy around the pedestal is barely visible.

the glass cell was not feasible for various reasons. The glass cell with its length of about 50 cm was considerably longer than the old main chamber with 30 cm length. Also, at least one additional bellow needed to be introduced to avoid mechanical stress on the glass cell. It was also highly desirable to pump the cell from both sides because of the outgassing load from the epoxy seal, requiring a second pumping cross after the differential pumping section. Since it was necessary to build a new Zeeman slower around the glass cell tubing, we decided to redesign the differential pumping stage as well.

3.2.1 Oven section

As a source of cesium we use dispensers[10] which are mounted on marcor holders in a simple metal tube with CF63 flanges on both ends. On one side, there is a blank flange with a built-in nozzle, while the other flange has four current feed-throughs and also provides a CF16 viewport. We have introduced some changes with respect to the old oven used before [Man99, Ham02a, Ryc04a].

The dispensers are rearranged in order to establish two independent current circuits. Normally only one of the circuits is used, and the other dispensers are kept in reserve. When one circuit fails (e.g. because of a short circuit or a broken connection), one can simply switch to the other dispensers and there is no need to break the vacuum.

After one year of operation, we experienced leakage of the oven window. After several similar incidents occurred in the past at different cesium experiments in our group, we concluded that cesium chemically attacks the viewport sealing. In our case,

[10] SAES getters CS/NF/8/25 FT10+10

the leak opened slowly on the timescale of hours and we could close the gate valve to protect the main vacuum in time. On another occasion in our group, the window broke suddenly and the main vacuum was only saved because an automatic pressure valve with an interlock circuit was installed. Since larger windows have a thicker sealing, two experiments now use a CF40 viewport in the oven section and have not experienced any further problems up to now. To avoid any risk we have opted to replace the window by a blank flange instead. The window was helpful for aligning the Zeeman slower beam and for the detection of an absorption signal to make sure the presence of cesium in the oven. But once the system was in operation, the window was never used any more, and we now appreciate the safety provided by the blank flange.

We have completely changed the design of the oven nozzle as well. The old nozzle [Man99] was a copper piece with a 40 mm long channel with a diameter of 2 mm. In order to increase the flux of atoms without worsening the differential pumping performance, we now use a much longer tube with larger diameter. The length is 20 cm and the inner diameter 3 mm, which should result in a pressure ratio of about three orders of magnitude between the two sides of the nozzle. We are still using the old pumping cross with its 20 l/s ion pump behind the nozzle. The cross also incorporates a valve for connecting a turbo pump during bake out and a wobble stick which is used as a shutter for the atomic beam.

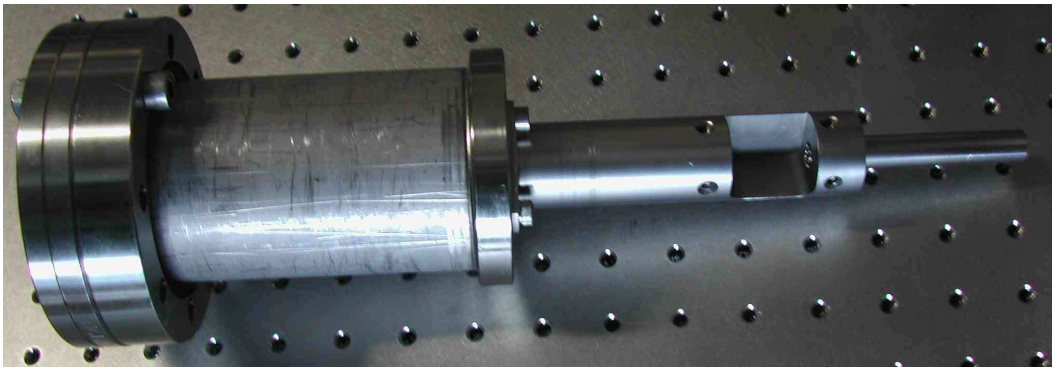

Figure 3.7: Oven with nozzle

Figure 3.7 shows the oven on the left side, and the nozzle piece attached on the right side. A square opening was milled into the nozzle piece where the shutter interrupts the atomic beam. To the left of the opening, the 20 cm long inner tube (not visible in the picture) extends far into the oven part with the dispensers. To the right of the opening, a second differential pumping tube of 8 cm length and 4 mm inner diameter was introduced. The opening for the shutter also serves the purpose of pumping in between the tubes.

It is important to note that the 8 cm long second differential pumping tube replaces the old 25 cm long tube with varying diameter from 4 to 9 mm around which the Zeeman slower coils of the old setup were wound. Because of the dramatic scaling of the vacuum conductance of a long tube with the third power of its diameter, it is highly

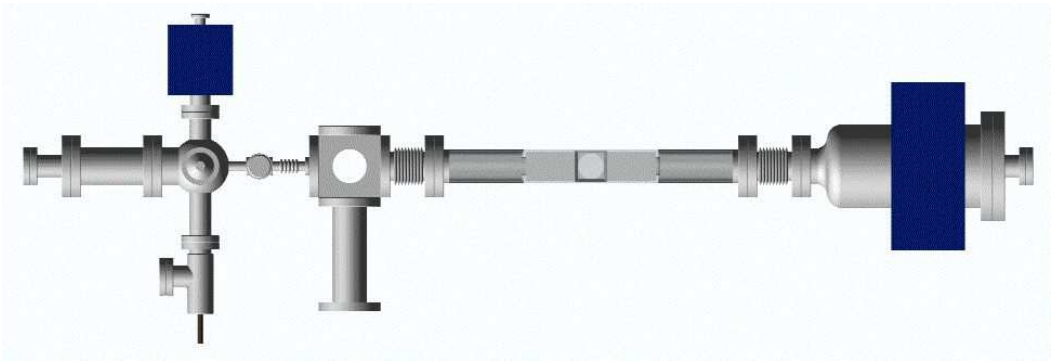

Figure 3.8: Overview of the vacuum system

advisable to do all of the differential pumping as close to the oven as possible. At larger distances to the oven nozzle, larger apertures have to be used in order to avoid truncation of the atomic beam, and differential pumping becomes inefficient. In the old design of the pumping tube, its second half had a diameter of 6 mm or more and barely contributed to the overall vacuum resistance. The new 8 cm long tube with a diameter of 4 mm gives a vacuum resistance of about 20 s/l, which is only a factor 1.5 smaller than the old value for the 25 cm long tube. This is more than sufficient given the introduction of an additional Titanium sublimation pump (see section 3.2.2) on the UHV side of the apparatus.

3.2.2 UHV section

Figure 3.8 shows a schematic top view of the assembled vacuum system. On the left side, there is the oven section (see 3.2.1) with a small ion pump attached to the old pumping cross [Man99]. The nozzle (see figure 3.7) is not visible, but it extends right to the gate valve which separates the oven section from the UHV section. In order to seal the right hand side of the nozzle to the CF16 flange of the valve, we use a blank copper gasket[11] with a bored hole where the nozzle fits in tightly. The hole has a diameter of 12.2 mm and we have diminished the outer diameter of the copper disc by about 1 mm to achieve a larger tolerance. The next vacuum element is a small bellow which gives the flexibility to adjust the whole oven section such that there is good overlap of the atomic beam with the MOT position. The bellow connects to a CF63 cube[12], which provides the same access as an ordinary cross but at a very compact size. It is used to attach a bent tube with a gauge (not shown in figure 3.8), and a tube with a Titanium sublimation pump[13]. The position of the cube is fixed by two massive stainless steel mounting clamps. It is important to use robust mounts which do not move under the substantial forces due to air pressure.

[11] CUB19, Thermo Vacuum Generators
[12] Hositrad CU63
[13] SBST 140 mm, Thermo Vacuum Generators

When installing a glass cell in a vacuum system, it is important to introduce bellows for stress reduction. We have opted for a bellow on either side of the cell, which simplifies the mounting. It would be sufficient to use a single bellow and a fixed connection on the other side, but then a resilient support has to be used for the flange that connects to the bellow. Without a supporting holder, the weight of the CF63 steel flanges might break the glass cell. With a bellow on either side, no resilient holders are necessary, and we could simply deposit the cell flanges on two steel supports with V-shaped grooves. The weight of the cell keeps it in place, and in addition we have secured the position with plastic screws under moderate stress.

We use large bellows[14] with CF63 flanges to get high vacuum conductances. It is essential to use the same type of bellow on either side. When the bellows have different sizes, the larger one will completely contract as soon as the pumps are turned on. Only for equal sizes do the forces due to air pressure cancel out.

As a special concern in our surface trapping scheme, the prism needs to be oriented horizontally. Using a water-level, we have done a coarse adjustment during assembly. The flexibility provided by the bellows enables a readjustment of the heights of the two ends of the cell if necessary. However, the bellows do not compensate for torsion, and therefore we have concentrated on avoiding rotational misalignment of the cell before tightening the vacuum screws. For a later fine-tuning of the surface orientation, it is possible to adjust the height of the feet of our floating optical table.

Connecting the cell to the rest of the vacuum system is an exciting task because of the risk of breakage. To minimize the stress that needs to be applied we have used annealed copper gaskets, which are softer than the ordinary ones.

The last part of our vacuum system is the old pumping section [Man99] with two NEG-modules[15] and an ion pump, a UHV gauge and a viewport to shine in the Zeeman slower beam. There is also a valve to attach a turbo pump while baking the system. The only update to the pumping section was a replacement of the valve, since we suspected the old one to leak. We have also rotated the whole section by 180 degrees and installed it with the ion pump facing upwards because of space restrictions. Again, as for the cube on the other side of the cell, we use a robust mounting clamp to withstand the air pressure on the system.

Baking procedure

Before the final assembly of the vacuum system, we performed a preliminary bake-out of the two bellows and the UHV pumping section at 350 °C for a few days. Later, the fully assembled system (including the glass cell with the epoxy seal) was baked for 5 days at 180 °C. To avoid temperature gradients, the whole apparatus was wrapped up in many layers of aluminium foil. Temperature sensors on either end of the cell showed temperature differences of less than 5 K during all of the bake-out. The heat-up time was about two days.

[14] Comvat, Haag, Switzerland
[15] WP950-ST707, SAES Getters

During the cool-down phase at 120 °C we activated the NEG-modules by running a current of 46 A at a voltage of 11 V for 4 minutes, which should result in activating temperatures of about 500 °C for the getter material. Because of an accompanying rise in temperature of the surrounding metal chamber to 140 °C we waited for half an hour before repeating the procedure twice. We also turned on the ion pumps while the system was hot, since there always is an initial burst of gas emitted when the pumps are started. We have also flashed all three filaments of our titanium sublimation pump for one minute at a current of 48 A before the baking procedure. After baking only the first filament was flashed several times.

Finally, at room temperature and without turbo pump, both the gauge close to the cube and the gauge in the UHV pumping section stated a pressure below 2×10^{-11} mbar. This ensures maximum pumping performance on both sides of the cell, but the local vacuum at the position of the prism might still be bad because of the outgassing of the epoxy seal. In order to test the vacuum there, we have measured the lifetime of atoms in a magnetic trap a few millimeters above the prism surface. The trap was loaded out of our MOT (see 5.1.1) by ramping up the quadrupole field and turning off all the laser beams. A homogenous magnetic field was used to control the vertical position of the trap. Figure 3.9 shows the exponential decay of the atom number with a decay time of 14 s, which is sufficient for our experiments. A comparison with lifetimes exceeding 100 s in other setups (e.g. [Web03a]) at pressures close to 10^{-11} mbar leads to the conclusion that our local pressure at the surface is around 10^{-10} mbar. Although all of the near-resonant laser light is generated on an optical table situated at a distance of a few meters to the trap, we found out that it is important to apply shields against stray light. Otherwise the lifetime shortens to values below 5 s.

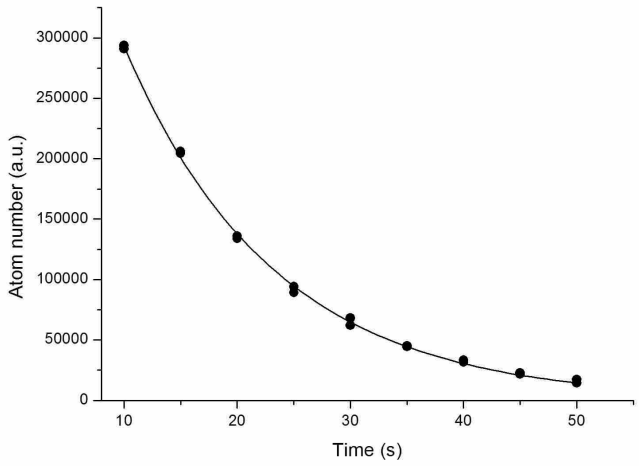

Figure 3.9: Lifetime measurement of a magnetic trap close to the prism surface, revealing a lifetime of 14 s.

4 Magnetic fields

Precise and fast magnetic field control is a crucial requirement for our experiment because of two reasons. On the one hand, magnetic gradients can be used to exert forces on the atoms, e.g. vertical forces which partially compensate gravity (see appendix B). After evaporation, the atomic ensemble is typically held in a shallow trap with weak optical forces, and precise control of the magnetic forces becomes important. On the other hand, the application of homogeneous magnetic fields facilitates the tuning of interactions in the presence of Feshbach resonances [Tie93, Ino98]. Since many resonances for cesium are narrow [Chi04], accurate control is essential. Also, the implementation of time-dependent schemes often requires fast switching times which are possible in our glass cell apparatus where eddy currents are absent. This chapter describes the design and specifications of our magnetic field coils and finally presents a microwave setup which is used to directly probe the field at the position of the atoms.

4.1 Vertical coils

The design of magnetic field coils involves finding the right trade-off between maximally achievable field strengths and optical access. Because cesium offers easy tuning of the scattering length via Feshbach resonances [Tie93, Ino98] already at weak magnetic fields, we aimed at a moderate maximum field strength of about 100 G. Therefore we could focus on building coils with the least restriction of our optical access to the glass cell. However, coil design proved to be a challenge because of the following constraints.

In addition to the homogenous field used for tuning of the scattering properties, a quadrupole field is also required in order to apply magnetic forces to the atoms. This enables partial or complete compensation of the gravitational force, or even overcompensation leading to an upward acceleration of the atomic cloud. In fact, the installation of powerful levitation coils was a prime objective, since it yields many experimental advantages. The design goal was to enable continuous full levitation (see appendix B) at a magnetic field gradient of 31 G/cm and to achieve a maximum gradient of 60 G/cm for a few seconds. We found the requirements for the quadrupole field much harder to meet than those for the homogenous field.

It is necessary to take into account the fact that our surface traps are not located in the center of the cell. Our cell has an outer height of 45 mm, and the pedestal height

of the prism is 10 mm. As a consequence, the atoms in a surface trap are situated at a distance of 10 mm to the lower outer side of the cell, whereas the distance to the upper side is 35 mm. It is desirable to build coils symmetrically around the position of the atoms, i.e. the trap should be located on the symmetry axis at equal distances to the coils. Therefore, the top coils are placed as close to the cell wall as possible, whereas there is an additional spacing of 25 mm for the bottom coils to achieve a symmetrical arrangement. Bearing in mind the thickness of the coils, we arrive at an effective distance between the top and bottom coils of about 100 mm, which is a comparatively large distance.

It is tempting to reduce the distance between the coils by shifting the bottom coil as close to the cell as possible and giving up the symmetry with respect to the trap position. But then, since the zero of the quadrupole field would not coincide with the trap position, there would be a contribution to the absolute value of the B-field coming from the quadrupole coils. Thus, the value of the magnetic field and its gradient could no longer be controlled independently, and a change in levitation strength would require an accompanying readjustment of the homogenous field. Another drawback of shifting the bottom coils upwards is that the zero of the quadrupole field then also shifts upwards by more than a centimeter. For levitation, the zero of the total magnetic field needs to be positioned below the atomic cloud, since the atoms are polarized in a high-field seeking state. Therefore, in order to shift the zero downwards, a high homogenous offset field of more than 30 G would be necessary in addition to any desired homogenous field strength.

To achieve independent control of the B-field value and its gradient, we have opted for the symmetrical arrangement of the coils, with the point of symmetry lying in the center of the prism surface. We then faced the problem that on the one hand, levitation requires the zero to be shifted downwards, but on the other hand, we planned to use the quadrupole coils also for the operation of our MOT (see 5.1.1), requiring an upward shift of the zero. With unipolar power supplies, only one of the two options could be realized. The problem was solved by building an electronic bridge-circuit that is able to flip the direction of the current flowing through the coils, handling currents of up to 100 A. The circuit can also be used to rapidly turn off the current[Pil05].

Coil construction

Our design is inspired by the coils used in another experiment in our group [Joc04], where the coils were made of flat copper wire and the cooling water was flowing within a PVC-housing. Every single winding had direct contact to the cooling water, which lead to efficient cooling and allowed for a power dissipation as high as 6 kW. Since our power requirements were less demanding, we could adapt the design and avoid the need of a water-proof PVC-housing which had repeatedly caused leakage problems.

The basic idea is to build two layers of coils made of flat copper wire, and then use a metallic disc in between to transport the heat away. The disc is then water-cooled on its periphery by flowing water through a copper tube. Since every winding touches the

disc, the cooling is still efficient without the need of freely flowing water in between the windings. We also found the disc very helpful for stable and versatile mounting of the coils and other elements.

Figure 4.1: Left, the water-cooled mounting disc. Right, the assembled vertical coil construction.

Cooled mounting discs

The left picture of figure 4.1 shows one of the two water-cooled mounting discs. It was milled out of a 3 mm thick aluminium plate and was black anodized later. It is important to introduce a slit in order to avoid eddy currents in the disc which would otherwise inhibit fast magnetic field switching. This main slit can be seen at the position of the two ends of the copper tubing. Care must be taken not to short-circuit the slit with the copper tube or other metallic mounting material. In addition to the main slit, we have introduced many grooves to further reduce eddy currents. The grooves also turned out to be valuable when aligning the coils before bonding them to the disc with epoxy. With the epoxy filling the groves, they helped to increase the bonding strength, too.

On the periphery of the cooling disc, we have introduced many bored holes for mounting purposes. They are used to attach the spacers between the upper and lower coil, to attach the four feet used to mount the coils on the optical table, and to connect the horizontal coil construction (see 4.2) to the discs.

Coil winding

We have wound a total of six coils and glued them to the two mounting discs. We used a flat copper wire with a cross section of 10 mm × 1 mm, leading to 10 mm thick ring-shaped coils. The winding was done by hand on a lathe, using a winding aid which provided the desired inner coil diameters. We have applied a thin layer of epoxy on every single winding to increase the stability of the coil. It was important to ensure

persistent drag on the wire during the winding process in order to avoid air gaps or excessive amounts of epoxy between the wires, which would otherwise have reduced the thermal conductivity across the coil. We have carefully selected an epoxy[1] with a high thermal conductivity of 1.3 W/mK and with a low thermal expansion coefficient which is matched to aluminium and copper. The same epoxy was later used to bond the coils to the mounting discs. To achieve good thermal contact to the discs, we concentrated on producing coils with an even surface during the winding process.

To create homogeneous fields, two coils with 10 windings were attached to the inner sides of the mounting discs, and connected to yield corotating currents. For the quadrupole field, we have produced 4 coils with 25 windings, and bonded them to either side of the two discs. They were connected to effectively form two coils with 50 windings in a counterrotating geometry. Taking into account the thickness of the coils, table 4.1 gives the approximate dimensions of the coils together with the resulting magnetic field and gradient per current. To achieve a more precise calibration, we have later performed measurements with cold trapped atoms. The calibration of the homogenous field was done using microwave spectroscopy with the setup described in section 4.5 and also by measuring the positions of various known Feshbach resonances [Chi04]. To get precise information on the magnetic gradient, we have observed the parabolic trajectories of an atomic cloud moving under the combined magnetic and gravitational forces for different currents in the quadrupole coils.

	radius	distance	windings	coefficient (calculated)	coefficient (measured)
Quadrupole	85 mm	96 mm	2×50	0.74 G/(A cm)	0.75 G/(A cm)
Homogenous	63 mm	83 mm	2×10	1.17 G/A	1.10 G/A

Table 4.1: Data for the vertical coils

Before final installation, the magnetic field coils were tested thoroughly [Pil05]. Measurements with a Hall probe confirmed the expected field values, and continuous operation of the quadrupole coils at 60 A lead to a moderate rise in temperature to about 35 °C . Thus, the water-cooling is efficient enough to allow for permanent levitation of cesium.

Current control

We use two independent switching power supplies[2] as a current source for the homogenous[3] and for the quadrupole[4] coils. We chose the options for fast programming and isolated input, in order to get faster response and to avoid ground-loop problems. The

[1] Eccobond 285 with catalyst 9
[2] Delta Elektronika, Netherlands
[3] SM 45-70
[4] SM 60-100

supplies are capable of delivering much more power (3 kW and 6 kW) than what is necessary to drive the ohmic load of our coils in a steady-state situation. This is necessary since it is our goal to achieve fast switching times. In order to build up a magnetic field fast, the supplies are forced to provide the energy which is stored in the magnetic field within a short time. Another way of saying this is that a large voltage reserve is needed to overcome the induction voltage which hinders changes of the current in the coils.

Turning off the coils quickly can be accomplished with transistor switches. We use a bridge-circuit which also allows for reversing the current flow in the coils. A varistor is installed to protect the switch against excessive induction voltages during turn-off. The energy of the magnetic field is then dissipated in the varistor and the transistors, and achievable switch-off times are below 100 μs. When high magnetic fields are turned off rapidly, there is the concern of vibrations induced by the mechanical forces on the coils. These vibrations might adversely affect the imaging procedure which often follows immediately after the magnetic field switching. Also, one might be afraid of loosening the epoxy bonds which hold our coils together. So far, we have not experienced any problems with fast magnetic field switching, but we try to avoid aggressive switching sequences. A simple way to check for vibrations is to put a finger on one of the coils during the experimental cycle, and when a shock wave can be felt, it might be a good idea to revise the timing sequence.

It is simple to completely turn off the current with the transistor switches, but sometimes a fast analog downward ramp with a non-zero final value needs to be programmed. In contrast to upward ramps, where it is sufficient to have a large voltage reserve, downward ramps present a problem which is critical at low currents. The reason is that our supplies are unipolar and are capable of sourcing current, but they cannot sink it. When programmed to reduce the current, the best they can do is to reduce the output voltage to zero and to effectively short-circuit the supply outputs. The current then drops exponentially with the time constant L/R, where L is the inductivity of the coils and R the resistance. The energy of the magnetic field is then converted to ohmic heat.

A straight-forward way to improve the performance of the analog ramps is to increase R by connecting external resistors in series with the coils. The time constant L/R is then reduced and allows faster downward ramps. The external resistors also improve the characteristics of the load, since otherwise an almost purely inductive load needs to be driven by the power supplies. The phase shifts introduced by the inductive load then adversely affect the stability of the current control loop. We typically use external resistances clearly larger than the resistance of the coils. Note that for too high values of the resistance, there is a compromise on the voltage reserve for upward ramps at high currents or even on the maximum achievable current. One should also take into account the high power dissipation across the resistors. We chose a simple resistor type which contains special metal plates[5], since these resistors are very robust

[5]Frizlen, Germany, resistor type FGFL

and work with air cooling even for many kilowatts of power dissipation.

At low currents, only slow downward ramps can be programmed because of the long exponential tail of the current decay, and increasing the resistance does not help much. We therefore additionally introduced high-power diodes into the current circuit in series with the coils. The diodes have a voltage threshold U_0 of a few volts and only conduct current at higher voltages. There is the same constant voltage drop U_0 across the diodes when a current flows, so effectively the diodes shift the zero of the voltage scale upwards by a few volts. Although still using unipolar supplies, to turn off the supplies is now equivalent to applying a negative offset voltage U_0. This leads to a linear decrease in current and avoids the long exponential tail of the decay curve without diodes.

The supplies can be programmed by an external voltage either in the constant current or constant voltage mode. Since we need stable magnetic fields and therefore currents, the constant current mode would be the natural choice. However, the supplies generate less current noise in the constant voltage mode. We hence decided to use this mode and to build an external feedback loop to control the current. Sensing of the actual current value is done using compensated transducers[6], and the desired value is programmed with 16-bit DACs providing voltages in the range from $-10\,\mathrm{V}$ to $+10\,\mathrm{V}$. It is essential to use high-quality sensors and to avoid ground-loops both in the sensing and programming circuit, since any ripple on the signals directly translates to a ripple on the current. Only the inaccuracies of the power supply will be suppressed by the gain of the feedback loop. Actual and programmed values are compared using PID-circuits which then generate the control voltage for the power supplies. The coefficients of the PID-circuit are adjusted with potentiometers in order to adapt to the specific characteristics of the supplies and their loads.

4.2 Horizontal coils

Although the main design axis for magnetic fields is the vertical axis, we have also installed coils to produce fields of up to 25 G in both horizontal directions. Since many applications do not require higher fields for cesium, the orientation of the magnetic field vector can then be chosen arbitrarily. When the levitation coils are active, the horizontal fields provide the possibility to fine-tune the direction of the magnetic gradient in order to avoid unwanted horizontal forces.

Figure 4.2 shows the horizontal coil construction, consisting of two pairs of rectangular coils. Each coil is held in place by two aluminium rails. Instead of epoxy, we applied thermally conductive paste and used screws to fix the position of the windings. The smaller coils had to be wound directly around the glass cell. The same flat copper wire was used as before, and the aluminium rails were attached to the mounting

[6] LEM IT600-S

discs of the vertical construction. The water cooling of the discs then also cools the horizontal coils.

Figure 4.2: Horizontal coil construction

Table 4.2 summarizes the geometrical data of the horizontal coils. Note the large width of the coils which are installed parallel to the cell, providing excellent optical access to the prism.

	height	width	distance	windings	coefficient (calculated)
small	135 mm	130 mm	252 mm	2×20	0.44 G/A
large	135 mm	460 mm	230 mm	2×20	0.67 G/A

Table 4.2: Data for the horizontal coils

4.3 Compensation cage

Already at an early stage before setting up the vacuum system, we installed a large cage around our optical breadboard. Three pairs of coils produce magnetic fields of up to 1 G in arbitrary directions. This is sufficient to compensate the magnetic field of the earth and weak stray fields. Figure 4.3 shows the dimensions and winding numbers of the coils. Typical currents in the coils are below 2 A and are driven with a self-built bipolar supply.

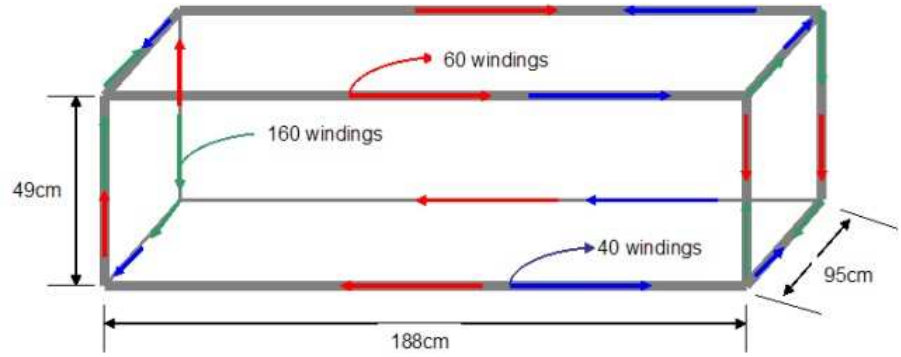

Figure 4.3: Compensation cage, see [Pil05]

A large compensation cage has many advantages:

- The large distance between the compensation coils and the actual experimental coils minimizes inductive coupling of the circuits. The magnetic flux produced by the high-field experimental coils flows within the cage without penetrating the compensation coils. This is important during fast switching sequences in order to avoid inductive voltage spikes in the compensation circuits.

- Fast reduction of the magnetic field to a small but non-zero value is difficult to achieve with the analog control of the main coils, as described in 4.1. Instead one can use the compensation coils to produce the desired small offset field, and rapidly switch off the main coils. Note that the procedure only works for negligible inductive coupling between the circuits. We use this technique to provide the small offset field required for Raman sideband cooling (see 5.1.3).

- Large coils produce more homogeneous magnetic fields. This helps when a sensor is placed close to the cell to measure the field. Clearly it is not possible to place the sensor to the actual point of interest, but for large compensation coils the magnetic field will not vary too much. The magnetic gradient of the compensation field will normally have a negligible effect on the cold atoms, but the practical problem of sensing the field is an issue favoring large homogenous coils.

To reduce the inhomogenous field produced by the permanent magnets of the ion pumps, we have installed magnetic shields around both pumps. The shields are made of several layers of special sheet metal as used in transformers, and an outer layer of μ-metal. The outer layer alone would not be sufficient because the high magnetic fields would saturate the μ-metal.

The compensation of ambient fluctuations is often the limiting factor of magnetic field stability in cesium experiments. This is different from experiments operating at high fields, e.g. 1000 G for experiments with ^{6}Li or ^{87}Rb, where the stability is limited by the performance of the current supply circuit for the high-field coils. In our case,

operation at 20 G with a relative current stability of better than 10^{-4} leads to fluctuations below 2 mG. On the other hand, ambient fluctuations often reach amplitudes of 10 mG or even more and are therefore the dominating source of instability.

The main contribution to the ambient fluctuations is the 50 Hz ripple originating from the AC power line. As long as noisy instruments are absent in the immediate vicinity of the experiment, the magnetic ripple will vary slowly in space and can be measured with a sensor at a distance of a few ten centimeters to the trap position. Placing the sensor too close to the main coils would expose it to excessive magnetic field strengths during the experimental cycle. We chose a three-axes fluxgate sensor[7] with a range of ± 2 G. It is possible to filter out the 50 Hz AC component of the sensor signal and install a negative feedback loop to control the current in the compensation coils. Although we have not finally implemented the feedback, some preliminary tests suggest that a reduction of the ripple amplitude by about an order of magnitude seems feasible.

4.4 Zeeman slower

Loading of a magneto-optical trap with an atomic beam is accomplished after continuously slowing down the atoms with a counterpropagating laser beam. It is necessary to design a spatially varying magnetic field that ensures resonant absorption by introducing Zeeman shifts that compensate for the change in Doppler shift due to the decreasing velocity. Constant deceleration requires a square-root shaped magnetic field profile, and it is desirable to finally merge the Zeeman slower field with the quadrupole field for the MOT. A large distance between the quadrupole coils and the Zeeman slower coils should be avoided since it would lead to excessive divergence of the atomic beam as a result of slow longitudinal and fast transverse motion. Therefore we had to design a new Zeeman slower around the glass-to-metal transitions of our glass cell, directly adjacent to the main coil construction.

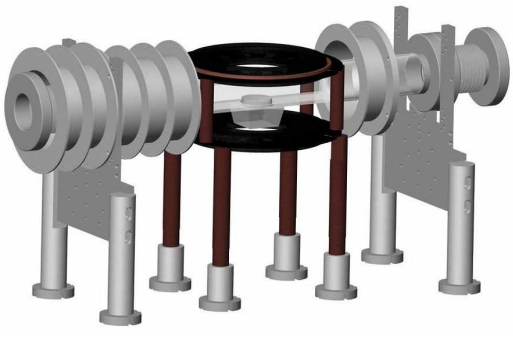

Figure 4.4: Zeeman coil assembly, see [Pil05]

[7] Stefan Mayer Instruments, Germany

Figure 4.4 shows the Zeeman coils mounted around the glass-to-metal transitions of the cell. On the left-hand side, five individual coils are fixed to the left holder of the cell, while there is a single coil mounted on the right-hand side. This coil compensates the residual Zeeman slower field at the position of the MOT, which would otherwise lead to a shift of the trapping position. The winding numbers from left to right are $301, 236, 216, 107, 193$ for the five Zeeman coils and 324 for the compensation coil. We operate all coils at the same current of about 2 A. The coil shells consist of two halves and were installed after completion of the vacuum setup. The shells were mounted in a rotatable way to simplify the handling of the wire during the winding process. For future bake-outs, after removal of some plastic clamps, it should be possible to bake the Zeeman slower at temperatures above 150°C, limited by the isolation coat of the wire.

Figure 4.5 shows the magnetic field contributions of the Zeeman slower and MOT coils in the axial direction and the total resulting field. It is possible to fine-tune the currents in the individual coils to achieve an almost ideal square-root curve, but we have checked experimentally that the performance of the slower is quite insensitive to such adjustments. We therefore prefer to operate the slower from a single power supply that delivers a current of 2 A. No cooling efforts are necessary since the coils only warm up slightly when continuously operated.

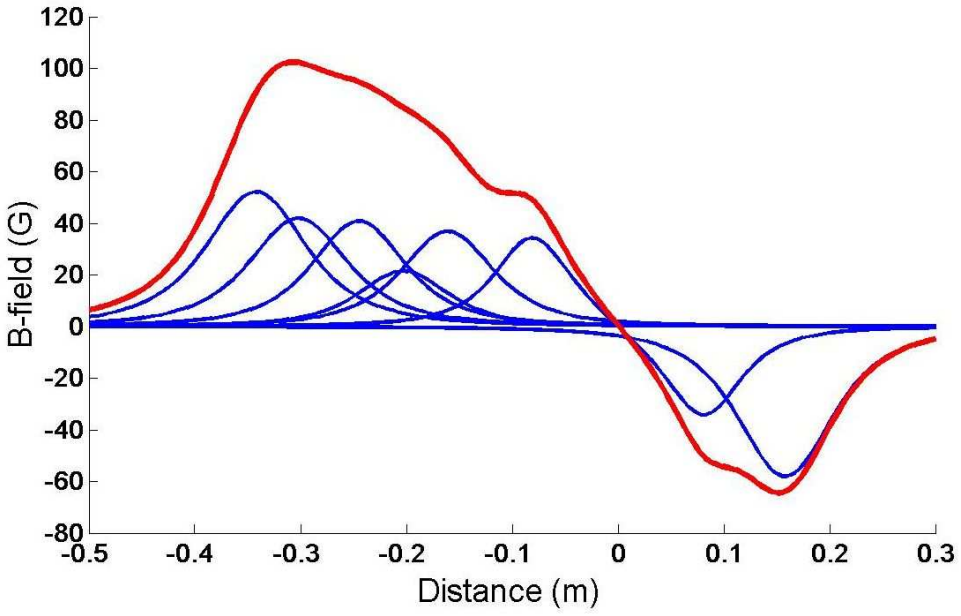

Figure 4.5: The axial magnetic field profile of the Zeeman slower and MOT coils. Blue curves show the contributions from individual coils, the red curve is the profile of the total axial field.

4.5 Microwave spectroscopy

As a useful tool for the characterization of magnetic fields, we have built a basic setup for microwave spectroscopy. The cold atoms themselves represent sensitive magnetic field sensors because of the Zeeman shift of their internal energy levels. Either hyperfine level $F = 3$ and $F = 4$ splits into its m_F substates as described in appendix A. Microwave radiation drives transitions between the hyperfine levels at frequencies close to 9.2 GHz. The selection rule for magnetic dipole transitions requires the m_F quantum number to remain the same or change by at most one. Keeping in mind the inverted m_F-structure of the upper hyperfine level $F = 4$, in total 15 transition lines are allowed in an unpolarized sample. For accessible magnetic field strengths, the Zeeman shift is linear and leads to equally spaced lines with a frequency difference of roughly 350 kHz/G between neighboring lines. The exact values and quadratic corrections are given in appendix A. Microwave spectra therefore provide a precise calibration of the magnetic field. In contrast to RF-spectroscopy, it is also possible to measure very small magnetic field values. We cancel the ambient field with our compensation coils by first reducing the spacing between the transition lines until they overlap and then minimizing the width of the degenerate line. The residual field can be reduced to a few mG. In addition to magnetic field calibration, microwave spectra reveal information on the inhomogeneity of the field via an analysis of the linewidths. Also, the intensity of the lines can be used to check the atomic polarization. For example, only the three lines with the highest frequencies should be observable for polarized atoms in the lowest state $F = 3, m_F = 3$.

Figure 4.6 presents a schematic view of the simple setup. The actual microwave source is a phase-locked dielectric resonator oscillator (PLDRO)[8] providing a fixed frequency of 9.15 GHz. The oscillator is referenced to an accurate 10 MHz signal derived from a commercial clock[9]. We then use a programmable radiofrequency source[10] and a mixer[11] to generate tunable sidebands. The carrier frequency of 9.15 GHz is normally off-resonant and does not perturb the atoms, while the sum frequency is used as the probe frequency. A switch[12] is controlled with a digital logic signal to turn the sideband on and off. After the mixer, an amplifier[13] boosts the output power and we get up to 20 dBm into the sideband. All the wiring is done using semi-flexible microwave cables with SMA-connectors. The amplified microwave is then fed into an outcoupler[14] which ejects the microwave into free space.

[8] PLDRO AM-4000-0910, Amplus Communication, Singapore
[9] PRS10 Rubidium frequency standard, Stanford Research Systems, USA
[10] Agilent 33250A, 80 MHz, GPIB
[11] ZMX-10G, Mini-Circuits, England
[12] ZWSW-1211, Mini-Circuits, England
[13] QPN-09113030, 8.5 to 9.6 GHz, 30dB gain, 30dBm output power, Quinstar Technology Inc, USA
[14] Waveguide R100, flange UER100, one side cut off, adapter UER100-SMA, Walter Krenn Hochfrequenztechnik GmbH, Austria

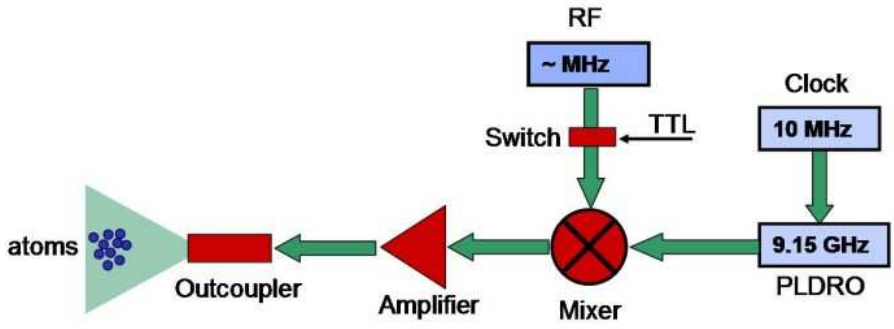

Figure 4.6: Schematic of the microwave setup.

We normally install the outcoupler at a distance of about 20 cm to the atoms. For maximum microwave intensity, the distance can be reduced to about 5 cm at the cost of reduced optical access to the glass cell. By contrast, it is often desirable to decrease the intensity in order to avoid power broadening of the spectroscopic lines. The output power is adjustable via the amplitude of the radiofrequency source or by insertion of fixed attenuators after the amplifier. The attenuators then also reduce potentially harmful reflections from the outcoupler which are caused by the mismatch in impedance between the waveguide and free space. Sure enough does amplification and subsequent attenuation introduce avoidable noise to the microwave signal, but so far this was not detrimental in our applications. The noise characteristics could also be greatly improved by directly connecting the clock signal to the PLDRO, since the PLDRO is very sensitive to any noise on its reference signal. At present, a clock from a distant lab is used in combination with a first distribution amplifier[15] and a second low-quality distribution amplifier[16]. We point out that the simple setup provides remarkably stable microwave frequencies due to the high quality of the readily available commercial clocks. When the radiofrequency source is referenced to the same clock signal, the microwave frequency drifts by less than 1 Hz. We often use a power splitter[17] before the outcoupler to monitor the frequency on a spectrum analyzer[18].

As its main application, the microwave setup is used to characterize magnetic fields. Figure 4.7 shows all of the expected 15 loss lines when the microwave is applied to an unpolarized sample in the lower hyperfine state $F = 3$. Increased loss is observed at each resonance because any population of the higher hyperfine state $F = 4$ quickly leads to trap loss via inelastic collisions. The line spacing of 120 kHz indicates a magnetic field value of 340 mG. The polarization of the microwave includes linear and circular components, as transitions with $\Delta m_F = 0$ as well as transitions with $\Delta m_F = \pm 1$

[15]Datum RF distribution amplifier, Symmetricom, USA
[16]PTS50, Precision Test Systems LTD, England
[17]ZFSC-2-10G, Mini-Circuits, England
[18]Rohde&Schwarz, FSP 13.6 GHz

are driven. The latter lines are slightly stronger since two transitions contribute to each line, with the exception of the non-degenerate outer lines ($F = 3, m_F = 3$ to $F = 4, m_F = 4$ for the highest frequency and $F = 3, m_F = -3$ to $F = 4, m_F = -4$ for the lowest frequency). The spectrum is compatible with the assumption of equal populations in every m_F-substate of the lower hyperfine level $F = 3$. In a polarized sample of atoms in $F = 3, m_F = 3$, only the three lines with the highest frequencies are visible.

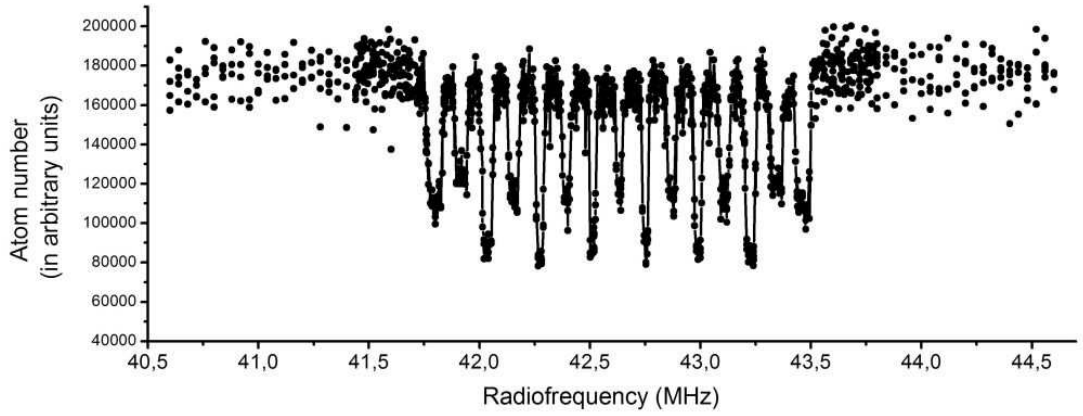

Figure 4.7: Microwave spectrum in an unpolarized sample. The radiofrequency is added to a fixed microwave frequency of 9.15 GHz.

In a later measurement, we have accurately determined the position and linewidth of the central line. This line corresponds to the clock transition from $F = 3, m_F = 0$ to $F = 4, m_F = 0$ with vanishing linear Zeeman shift. The loss signal was obtained by applying the microwave for 2 s at a power level reduced by 50 dB to avoid power broadening. We observed a very narrow line with a width of 35 Hz (FWHM) close to the expected clock frequency (see fig. 4.8). Since the quadratic Zeeman effect for the clock transition is 427 Hz at a field of 1 G (see appendix A), the slight shift of 20 Hz indicates the presence of a small magnetic field of 200 mG. As we observe a very narrow line at the clock transition, the stability of the microwave setup is not a limiting factor for the linewidth of the other lines. When power broadening is avoided, it is then possible to deduce the inhomogeneity of the magnetic field from the observed widths.

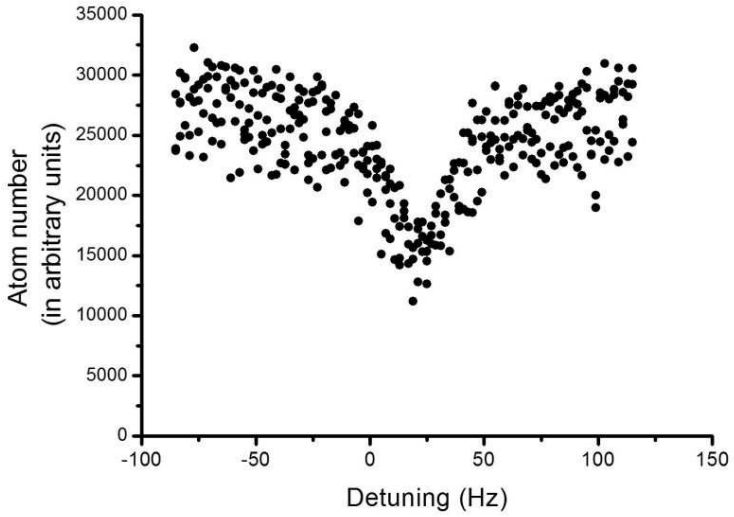

Figure 4.8: Microwave resonance of the clock transition from $F = 3, m_F = 0$ to $F = 4, m_F = 0$. The detuning refers to the exact transition frequency $9'192'631'770$ Hz.

5 Experimental methods

Our scheme for the preparation of ultracold cesium in a surface trap is based on a sequence of cooling and trapping methods. This chapter describes these methods and our standard techniques for the characterization of the system. Temperature measurements, the determination of trapping frequencies and absorption imaging are discussed. With this set of tools, we investigate the performance of optical evaporation and demonstrate a standing-wave surface trap.

5.1 Optical cooling

In the last two decades, many powerful optical cooling methods were developed in the quest for ultralow temperatures and high phase-space densities. A sequence of these are used as important stages of capturing and precooling atoms in our experiment. Since most methods are standard techniques, they are only shortly described in the context of our surface trap.

5.1.1 Magneto-optical trap

Almost all experiments on ultracold atomic gases make use of a magneto-optical trap (MOT) as a first step to collect large atomic samples at temperatures in the microkelvin regime. A MOT relies on the spontaneous force of near-resonant laser light acting on the atomic motion [Raa87]. Six counterpropagating, red-detuned laser beams are applied to the gas from all directions. A magnetic quadrupole field spatially tunes the light force via the Zeeman effect which leads to confinement of the gas. At the same time, cooling takes place due to the Doppler effect which causes velocity-dependent forces and dissipation.

As a source for near-resonant light, we use a diode laser system that is described in detail in [Pil05]. The system is based on a grating stabilized master laser and several injection locked slave lasers. Acousto-optical modulators (AOMs) shift the frequency of the light to the desired detuning and provide fast intensity control. In order to protect the experimental setup from stray light, the diode lasers are situated on a shielded separate table. Polarization maintaining optical fibers deliver the light to the experiment, with the additional benefit of decoupling the laser alignment of the two tables and

simplifying occasional troubleshooting. However, fibers can introduce thermal fluctuations as a result of imperfect polarization maintenance. Our standard outcoupling setup therefore includes a polarizing beam-splitter cube to clean up the polarization and afterwards a pick-off plate that couples out a few percent of the light for monitoring purposes. The monitored intensities are stabilized via control loops acting on the AOMs before the fibers. After the fibers, we work with output powers of 60 mW for the MOT, 20 mW for the Repumper and 40 mW for the Zeeman slower.

We load the MOT at a distance of a few millimeters to the surface from the Zeeman-slowed atomic beam (see section 4.4). The orientation of the MOT geometry has been rotated with respect to the old setup [Ham02a, Ryc04a] such that the levitation coils can be used to create the required quadrupole field. Four beams are applied in the horizontal plane, and careful adjustment is necessary since the desired circular polarization is spoiled upon reflection from the surface. Loading the MOT too close to the surface is inefficient because of imperfect polarizations and the truncated capturing volume. Within a loading time of 4 s we collect about 2×10^8 atoms. The cloud is then moved closer to the surface by shifting the zero of the quadrupole field before releasing the atoms into the surface trap. When optimizing the size of the MOT, it is necessary to keep in mind that the alignment of the lasers should also allow for a decent transfer down to the surface. During the transfer sequence, we ramp up the gradient of the quadrupole field from 7 G/cm to 22 G/cm and increase the detuning of the MOT beams from 8 MHz to about 50 MHz. This procedure helps to compress the atomic cloud and to further reduce its temperature to about 40 μK via sub-Doppler cooling mechanisms [Tow95, Tow96].

5.1.2 Sisyphus cooling

Even with careful alignment of the MOT beams, the size of the atomic cloud limits the average distance to the surface to more than 200 μm. After release from the MOT, the atoms gain large amounts of gravitational energy ($mg * 6\,\mu\text{m} = k_B * 1\,\mu\text{K}$). As a crucial step in our loading sequence, the first surface trap includes a dissipative mechanism which quickly cools away the energy introduced by the vertical transfer. The mechanism is based on inelastic reflections from an evanescent-wave mirror and was examined in detail in early experiments of the previous setup [Ovc97, Man99, Ham02a]. A diode laser provides a beam of 50 mW blue-detuned with respect to the D2-line by about 2 GHz. The beam undergoes total internal reflection at the prism surface and forms a repulsive evanescent wave. Spontaneous photon scattering events during a bounce and subsequent optical pumping lead to optical Sisyphus cooling. The repulsive evanescent wave and gravity give rise to a wedge-shaped trapping potential in the vertical direction. Horizontal confinement is achieved with a repulsive hollow beam that evolves from a special axicon optics [Ham02a]. The beam has a diameter of 800 μm and a power of 80 mW at a detuning of about 25 GHz and is produced by a diode laser. Figure 5.1 shows a schematic of the trap setup. After several seconds of

Sisyphus cooling, ensembles of about 10^7 unpolarized atoms at a temperature of $10\,\mu$K are obtained.

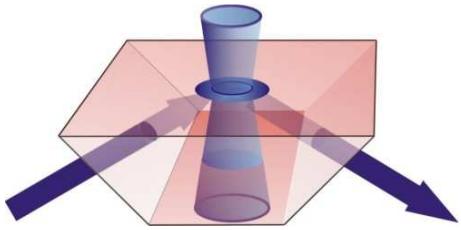

Figure 5.1: Schematic view of the hollow-beam trap.

5.1.3 Raman sideband cooling in a surface trap

Further optical cooling is achieved by degenerate Raman sideband cooling [Ker00] with the additional benefit of simultaneous polarization into the lowest internal atomic state. We have adopted the geometry presented in [Tre01] which comprehends in total four lattice beams with linear polarizations. A vertical beam is sent in from above while two beams enter horizontally, and one of the horizontal beams is retro-reflected. We implement Raman cooling directly in our reservoir trap close to the surface by applying the horizontal beams under grazing incidence at an angle of a few degrees to the surface. Under these conditions the prism reflects almost perfectly, and obviously the resulting lattice structure is not as simple as would be the case without surface. However, after careful optimization of adjustment, polarizations and the required magnetic offset field, the cooling technique still works. In the following, we present practical hints for the implementation of Raman cooling and the results we have achieved.

It is not hard to optimize the setup once a first signal for successful Raman cooling has been observed. However, it might take a long time to obtain the first signal since the method depends sensitively on many parameters. In our view, the best way to start the implementation is to make sure optical pumping with the polarizing beam works reasonably well. This may be done by Stern-Gerlach separation experiments after an optical pumping pulse. Even if this procedure requires temporary adaptations of the imaging setup to obtain a larger field of view, it is worth the effort since the polarization of the pumping beam can then be set without worrying about the Raman lattice beams. The beam diameter should be a few mm, since a large beam is less sensitive to adjustment and only low laser powers of below 1 mW are necessary. The value of the magnetic offset field should be roughly a few hundred mG, which is then optimized later during Raman cooling. With an optical pumping pulse of $100\,\mu$s, we typically obtain a polarized sample with a purity of about 90 percent.

As a next step, we optimize the adjustment of the four lattice beams. Coarse positioning of the beams is easily accomplished by permanently turning on a single beam while operating a MOT. When the alignment is approximately right, the beam should

blow the MOT away. Since the MOT is not situated at the same position as the surface trap where Raman cooling should take place, we then implement a refined adjustment procedure. After loading the reservoir trap and shortly before absorption imaging, we apply a pulse of about 200 μs from a single Raman beam and try to shoot the reservoir cloud away. As opposed to the usual cooling sequence, it is essential to turn on the repumping beam as well. Otherwise the atoms remain in the lower hyperfine state and do not absorb the Raman laser light. Alignment of the vertical and two horizontal beams is then followed by adjusting the retro-reflected beam such that it overlaps with the incoming beam.

At this stage the setup is ready to search for a preliminary signal from Raman cooling. After a cooling phase of a few ms, a simple signature can be obtained by letting the atomic cloud expand for a fixed time (e.g. 20 ms) and aiming at high densities after expansion. Varying the magnitude of the magnetic offset field should lead to resonant behavior and reveal the optimum value.

As a next step, the sudden turn-off of the lattice should be replaced with an adiabatic ramp, which typically reduces the achievable temperatures by about a factor of two. We do not observe a critical dependence on the exact waveform or timescale of the ramp and use a simple low-pass filter with a RC-time of about 100 μs to generate an exponential ramp. The intensity is stabilized with a control loop which measures the output power after an optical fiber and controls an AOM before the fiber. The maximum output power is 60 mW after the fiber and, as a technical remark, the AOM is optimized for short pulses. Turning the RF-power on for longer times would heat up the AOM and affect the beam-pointing and thus the fiber-coupling efficiency. Under normal operation, the Raman beams are turned on for only 7 ms once in an experimental cycle, and the AOM remains cold.

After a basic Raman cooling performance has been established, repeated fine-tuning of all parameters including the orientation of the magnetic offset field and beam polarizations will yield the final result. In a preliminary experiment under ordinary conditions high above the surface, we directly loaded atoms from a detuned MOT into the Raman lattice and achieved temperatures of about 1 μK with 2×10^7 polarized atoms. For the actual implementation with the reservoir close to the surface, we could only measure the temperature after loading the atoms into the high-power evanescent wave trap (see 5.2). After equilibration, 3×10^6 atoms at a temperature of 3 μK could be trapped, with a polarization purity of better than 90 percent. It is important to realize that loading a Raman cooled sample into a trap can introduce substantial heating due to imperfect mode-matching. In this case, further improvements in the cooling performance will not translate into better final conditions in the trap [Web03a].

5.2 High-power evanescent wave trap

In the reservoir trap described in section 5.1.2, the density distribution is constant in the horizontal directions and shows an exponential decay in the upward direction with the

thermal decay length $k_B T/(mg)$. The Raman cooling stage (see 5.1.3) freezes this distribution, since the atoms are trapped in the lattice potential. Simply turning the lattice off would result in vertical equilibration oscillations since the old density distribution does not fit to the suddenly reduced temperature which would require a correspondingly reduced vertical decay length. In order to avoid this mode-matching problem and the resulting heating, we ramp up our magnetic levitation field immediately after the lattice is switched off. We obtained the best performance when compensating for 85 per cent of gravity.

In order to preserve the atomic polarization, it is necessary to replace the near-resonant trapping light for the evanescent wave and the hollow beam with far-detuned, high-power laser light. For the hollow beam, we use our Titanium-Sapphire laser at a wavelength of 846 nm, i.e. at a detuning of 6 nm from the D2-line. The light is coupled into the fiber that feeds the hollow-beam optics and we obtain about 400 mW of laser power in the final beam. For the evanescent wave, we have set up a new high power laser system[1] operating at 810 nm with an output power of 80 W. It consists of high-power laser diodes emitting into a multimode fiber and providing an incoherent, but homogenous beam at the fiber output.

When dealing with incoherent light sources, some differences to diffraction-limited laser beams require careful consideration. In general, Gaussian-beam optics is only applicable for laser beams which are almost diffraction-limited. Incoherent light beams show much stronger divergence and are more difficult to handle. The light propagation can be described by geometrical optics, with the output facet of the fiber treated as a homogenously shining disc. The light rays emerge within a cone from every point of the disc, and the angle of the cone is determined by the numerical aperture (NA) of the fiber. It is possible to interpret the lenses for collimation and focussing as an optical system which takes the output facet of the fiber as an object and forms an image at the position of the atomic trap, i.e. at the prism surface. As a general imaging property, the product of diameter and divergence angle remains constant. In the following, we consider the practical implications of this property.

A serious concern when forming an evanescent wave from a spatially incoherent light beam is the fact that there is no single, well-defined angle of incidence but rather a distribution of angles because of the inherent divergence of the beam. A coherent laser beam would have flat wavefronts in its focus, but this is not true for incoherent beams. Setting the average angle of incidence too close to the critical angle of total internal reflection therefore leads to partial transmittance of the beam, which is highly undesirable for an atomic trap. However, our experience with evanescent wave traps shows that the angle of incidence should not deviate by more than a few degrees from the critical angle. Otherwise the very short decay lengths of the evanescent waves would result in short trapping lifetimes due to surface effects. With this constraint in mind we have chosen a fiber with only 150 μm diameter and a numerical aperture of NA 0.22. The beam divergence at the fiber output is ±13 degrees, and since the

[1] OTF90-15-IP, Optotools, Germany

evanescent-wave spot should have a diameter of roughly 1 mm, the lens system reduces the divergence at the prism by a factor of 7, and the index of refraction of the fused-silica prism helps with another factor of 1.45. The angle of incidence then has a narrow distribution of ±1.3 degrees, which is still acceptable for the creation of an evanescent-wave trap. In practice, we set the angle as close to the critical angle as possible while making sure that no transmitted beam emerges from the prism.

For convenient beam handling, we work with large beam diameters and consequently low divergence. The output coupler has a focal length of $f = 35\,\text{mm}$ and produces an almost collimated beam with a diameter of $\text{NA} \times 2f = 15\,\text{mm}$. Large beam diameters are also advantageous because of the high laser power of 80 W, since the intensity of smaller beams might exceed the damage threshold of optical elements or lead to burn-in of dust into optical coatings.

A schematic view of the setup is presented in figure 5.2. The unpolarized output from the fiber is equally split into two polarized beams with a polarizing cube which is operating close to its specified damage threshold. For the transmitted beam, we then rotate the polarization with a $\lambda/2$-retardation plate, and finally superimpose the two TM-polarized beams on the prism surface. The polarization is important to maximize the evanescent-wave intensity and also to make sure that reflections from the prism are suppressed for entry and exit under the brewster angle. Interference fringes do not occur since the optical lengths of the two paths differ by many centimeters, which is by far more than the coherence length of a few millimeters.

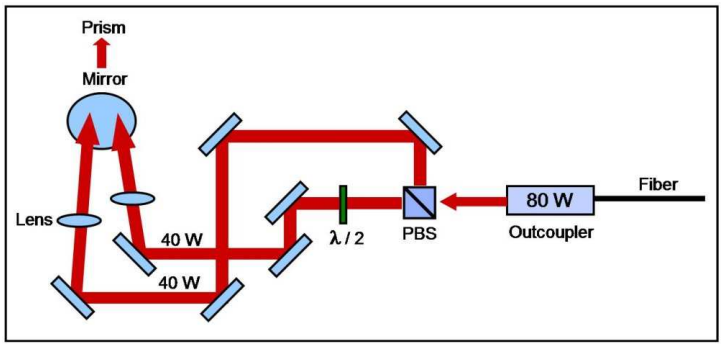

Figure 5.2: Optical setup for the high-power evanescent wave.

Most of the mirrors are ordinary broad-band dielectric mirrors[2]. In an effort to eliminate any harmful background light which might cause resonant absorption at the cesium D1- and D2-lines, we have later exchanged some of the mirrors with long-pass filters[3]. These filters are highly reflective at the desired laser wavelength of 810 nm, but do not reflect light at 850 nm and 895 nm. Although the introduction of the filters has not led to an improvement in trapping performance in our case, we would always

[2]Thorlabs BB1-E03
[3]Laseroptik Garbsen, Germany

recommend to consider a possible resonant background when using high-power diode lasers.

As a result, we are able to load 3×10^6 polarized atoms at a temperature of $3\,\mu$K into the far-detuned reservoir trap. The lifetime of the sample is about 7 s, which is sufficient for the subsequent loading of a dimple potential (see section 5.3). As expected, the lifetime drops dramatically when the less detuned diode-laser light for the evanescent wave and hollow beam is not extinguished.

5.3 Evaporative cooling

A well-known technique to enhance the phase-space density and the elastic collision rate of a trapped atomic gas is the dimple trick [Pin97, SK98]. We use our reservoir to load a small dimple potential which is formed by a focused attractive beam derived from a 10 W fiber-laser at a wavelength of 1060 nm. After turning off the hollow beam, we perform forced evaporative cooling by slowly ramping down the optical dimple potential. A similar procedure already proved successful in the old setup [Ham02b, Ryc04a], but with an unpolarized reservoir and subsequent optical pumping in the dimple trap. With the new scheme of directly loading from a polarized sample, we avoid inelastic two-body loss already in the loading phase.

Our quantitative results depend critically on measurements of atom number, temperature and trapping frequencies, and we have implemented updated measurement procedures in the new setup.

5.3.1 Absorption imaging

A common technique to measure the density distribution of an atomic cloud is absorption imaging [Ket99]. A short pulse of resonant laser light illuminates the atoms and is absorbed according to the integrated column density of the cloud. The absorption profile is then imaged onto a CCD-camera with a suitable lens system. With the known absorption cross section, the pictures provide calibrated density and atom number measurements. It is often adequate to fit a Gaussian to the density profile and extract the peak density and width of the distribution.

In our special situation we need to take into account the presence of the surface. Attempts to align the imaging beam parallel to the surface fail because of beam truncation and diffraction patterns which obscure the atomic signal. In order to image atoms at heights as low as a few micrometers above the prism, we reflect the beam under grazing incidence from the surface at an angle of typically 5 degrees. In this configuration, the camera picture shows not only the real atomic cloud but also its mirror image due to the reflection on the prism (see figure 5.3).

For large clouds close to the surface, image and mirror image overlap. It is then still possible to evaluate the atom number by summing up the total signal and dividing the calculated atom number by two.

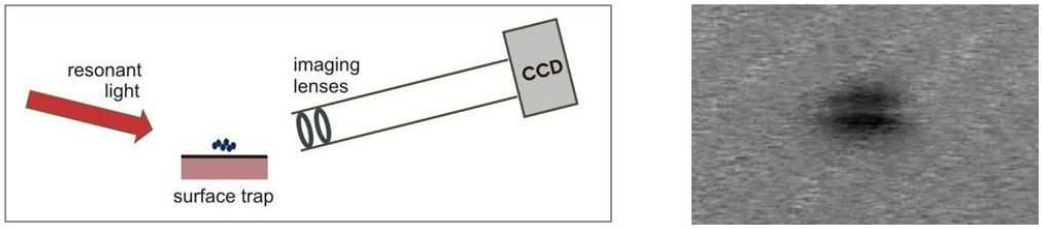

Figure 5.3: Left: Absorption imaging of atoms in a surface trap. The imaging beam is reflected on the surface under grazing incidence at an angle of about 5 degrees. Right: Image and mirror image of an ultracold cesium cloud at a temperature of 30 nK, with a distance to the surface of 11 μm.

We use a CCD-chip[4] with a pixel size of 7.5 μm × 7.5 μm and an imaging system that provides a magnification of roughly a factor of three. The first imaging lens is a monochromatic doublet[5] with a focal length of 80 mm and the second lens is an achromat[6] with a focal length of 250 mm. With the object situated in the focal plane of the first lens, the system provides an image in the focal plane of the second lens. We have conveniently mounted the lenses in a 30 cm long tube[7] which directly connects to the camera. A resolution test pattern revealed a spatial resolution below 10 μm and provided a precise calibration of the magnification factor of $M = 3.36$. Therefore, each pixel of an image corresponds to 2.23 μm × 2.23 μm in reality. With respect to sensitivity, our detection limit is below one thousand atoms, while reliable Gaussian fits require a few thousand atoms.

5.3.2 Temperature measurements

Let us consider a harmonically trapped thermal cloud with a Gaussian density profile $n = n_0 \exp\left(-x^2/(2\sigma^2)\right)$ with standard width σ. The initial width $\sigma_0 = \sqrt{k_B T/(m\omega^2)}$ depends on the temperature and on the trapping frequency $\omega/(2\pi)$. When suddenly released from the trap, the cloud retains its Gaussian shape and expands according to

$$\sigma(t) = \sqrt{\sigma_0^2 + (k_B T/m)\, t^2} \tag{5.1}$$

with t denoting the expansion time and T the temperature of the cloud. However, in our special situation we have to take into account the presence of the surface. Ultracold atoms hitting the room-temperature prism will be immediately lost. With the trapping light switched off, the atomic cloud expands while falling under gravity, with the surface cutting into the Gaussian density distribution. Measuring the remaining

[4] Philips FT18 within Theta System SIS1-p18
[5] LAI009/76, Melles Griot
[6] AC254-250-B, Thorlabs
[7] Thorlabs SM1

total atom number at various expansion times then allows to extract the temperature of the sample. In the rest frame of the atomic center of mass, the surface is initially at a distance z_0 and then accelerates upwards with the constant of gravity g. The remaining fraction f of atoms is calculated as an integral over the density distribution with the surface position as a lower bound, giving

$$f = N\left(\frac{1}{\sigma(t)}\left(z_0 - \frac{1}{2}gt^2\right)\right) \tag{5.2}$$

with N denoting the cumulative normal distribution and $\sigma(t)$ determined by equation 5.1. When partial magnetic levitation is applied, the constant of gravity is to be replaced with its effective value $\tilde{g}$. At ultralow temperatures, the function $f(t)$ features a plateau at small evolution times t which reflects the time that is needed to fall the initial distance z_0. Figure 5.4 shows a typical curve for $\tilde{g} = 0.15g$ with the temperature 78(8) nK determined from a fit to equation 5.2.

Another way of dealing with the surface is to switch off the optical trap and rapidly lift the atoms up with a magnetic gradient before they fall onto the surface. It is then possible to monitor the thermally expanding cloud with absorption images and determine the temperature in the standard way using equation 5.1. Figure 5.4 also shows such an expansion measurement under identical initial conditions as for the previous method. The fit gives a value for the temperature of 75 nK, proving that both methods yield consistent results.

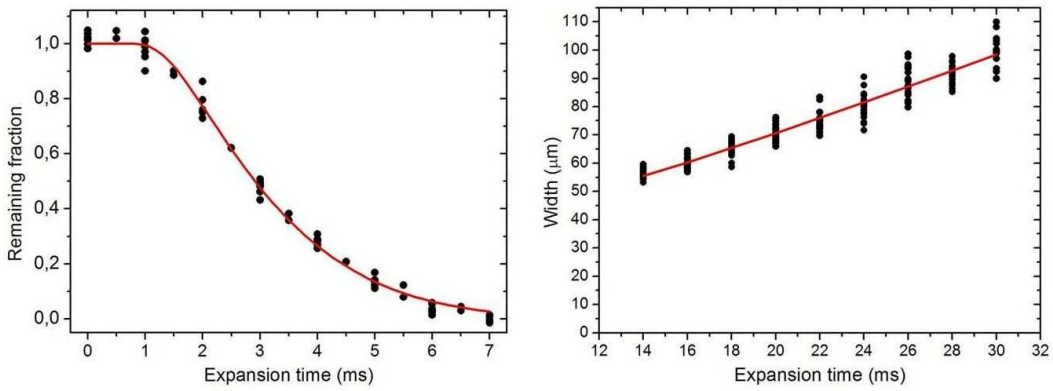

Figure 5.4: Left, temperature measurement with atoms hitting the surface. Right, temperature measurement with a magnetic gradient accelerating the atoms away from the surface. Both methods yield a consistent temperature of 75 ± 8 nK.

5.3.3 Trapping frequencies

Our measurements of trapping frequencies rely on different approaches for the horizontal and the vertical directions.

In the horizontal directions, we directly observe the dipolar oscillations of the atomic cloud after a small initial displacement of the trap. The displacement is realized via a scanning setup for the dimple laser as described in [Pil05]. We use two AOMs in order to control the position of the laser beam on the prism, and a jump in the driving radiofrequency results in the initial displacement which triggers oscillations of the trapped cloud around the new equilibrium position. After variable waiting times, the center position of the cloud is directly measured via an absorption picture. It is possible to enhance the visibility of the oscillations by turning the dimple laser off about 10 ms before the picture and thereby allowing for some free expansion. Figure 5.5 shows such oscillations which allow for the precise determination of horizontal trapping frequencies. Since the laser power of the dimple beam can be measured independently, such frequency measurements reveal the actual waist of the focused beam at the position of the prism surface. For a given waist, the trapping frequencies vary proportional to the square root of the laser power. In the presented example, we measure a trapping frequency of 40(4) Hz at a power of 80 mW and infer a beam waist of 80 μm.

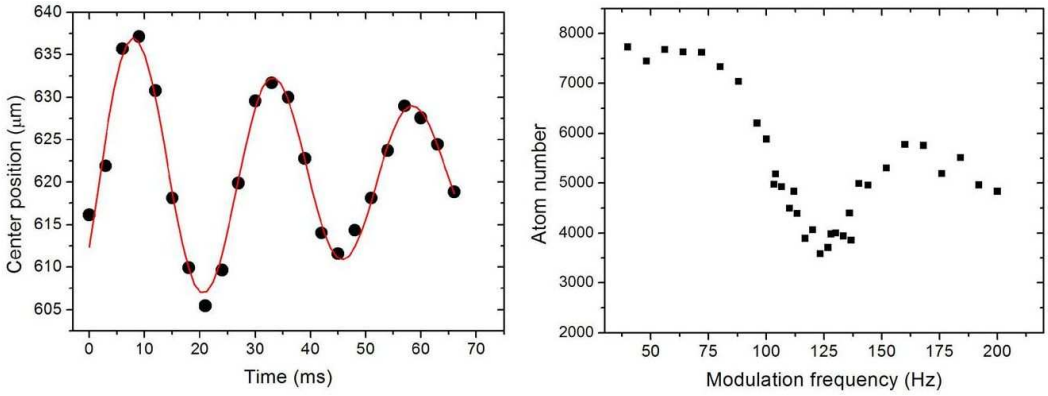

Figure 5.5: Trapping frequencies are measured via direct observation of dipolar oscillations in the horizontal directions (left), or via resonant loss induced by a modulation of the evanescent-wave intensity (right).

In the vertical direction, measuring the trapping frequency is only possible after cooling the atomic cloud into the harmonic trapping regime (see section 2.3). We then modulate the intensity of the evanescent-wave and observe resonant loss when the modulation frequency is close to the vertical trapping frequency. Since anharmonic effects need to be considered, the minimum position in the remaining atom number does not coincide with the value of the trapping frequency. As a reasonable estimate, we assume that the trapping frequency lies above the minimum within the width of the loss peak. Figure 5.5 shows a typical vertical trapping frequency measurement, with a relative modulation amplitude of 10 per cent applied for 1.7 s to the evanescent-wave intensity. In the example, the frequency is determined to 145(20) Hz.

5.3.4 Evaporation results

Loading the dimple potential from the reservoir and waiting for 300 ms of plain evaporation leads to a sample of 7×10^5 polarized atoms at a temperature of $4.7\,\mu$K. With a power of 1.6 W and a waist of $85\,\mu$m, the dimple laser confines the atoms horizontally with a trapping frequency of 170 Hz. In the vertical direction, the wedge-shaped potential is determined by the reduced constant of gravity $\tilde{g} = 0.15\,g$. These parameters lead to calculated values for the peak density $n_0 = 2 \times 10^{12}\,\mathrm{cm}^{-3}$ and the peak phase-space density $D_0 = 6 \times 10^{-4}$.

With these initial conditions, forced evaporation is started by ramping down the laser power of the dimple. Within 5 s, we decrease the power from 1.6 W to 18 mW. In the horizontal directions, the trap is decompressed which leads to adiabatic cooling. In addition, evaporative cooling takes place and enhances the phase-space density. We measure a final temperature of 75 nK for 1.3×10^4 atoms at a horizontal trapping frequency of 18 Hz. In contrast to the initial situation, we now approximate the vertical potential with its harmonic expansion and measure a value of 145 Hz for the vertical trapping frequency. With these parameters, we calculate a peak density of $1.0 \times 10^{12}\,\mathrm{cm}^{-3}$ and a peak phase-space density of 0.2. The atom number goes down by a factor of 55 while there is an increase in phase-space density by a factor of 300. The overall efficiency parameter [Ket96] $\gamma = \ln(D/D_0)/\ln(N/N_0)$ therefore equals 1.4. It is possible to extend the evaporation ramp to even lower temperatures, and we reach phase-space densities close to unity. However, the low atom numbers make reliable temperature measurements difficult and we could not observe signatures of quantum degeneracy as demonstrated in previous work [Ryc04b].

With respect to initial conditions and efficiency, our evaporation results are comparable with the performance that was obtained in the previous setup [Ryc04a]. In the old apparatus, the last step from a nearly degenerate sample to the actual indirect observation of a tiny Bose-Einstein condensate required an extensive effort of optimization. The procedure included repeated changes in the trap position to find the best spot on the prism with subsequent realignment of all experimental stages, and also dynamic variation of trap parameters during the evaporation ramp. In the new setup, a moderate effort of optimization has led to conditions close to degeneracy, but the phase-transition was not observed so far.

As a conclusion, the improvement in surface quality and the use of a polarized reservoir has not resulted in superior evaporation performance. We observe a critical dependence on the actual trapping position on the prism, which indicates that surface effects still hamper more efficient evaporation. However, we are able to reliably produce samples at ultralow temperatures in a range down to below 100 nK, which is crucial for the measurements on three-body loss presented in chapter 6.3. These measurements are performed at negative scattering lengths, where a Bose-Einstein condensate would not be stable anyways. Also, our evaporation scheme leads to moderate final densities which is advantageous for the investigation of resonantly enhanced three-body loss.

5.4 Standing-wave surface trap

One of the main motivations for surface trapping is to provide the highly anisotropic confinement which is necessary for the investigation of low-dimensional systems. As an example, we have achieved a two-dimensional Bose-Einstein condensate in the old apparatus [Ryc04b], with both thermal energy and chemical potential dominated by the vibrational energy quantum in the tightly confined vertical direction. Modifications of elastic two-body collisions or inelastic three-body loss are expected when the vertical harmonic oscillator length is so small that it becomes comparable to the scattering length. However, such conditions are hard to achieve and require additional compression techniques.

We apply a magnetic gradient to partially compensate for gravity ($\tilde{g} = 0.15g$) during optical evaporation, which results in vertical trapping frequencies of about 150 Hz. When the gradient is ramped down afterwards, the trapping frequency increases to about 500 Hz. Further compression by reversing the magnetic force and pressing the atoms onto the evanescent wave is possible but not very effective. At maximum, our gradient coils could enhance g by a factor of three, and thus increase the trapping frequency by a mere factor of $\sqrt{3}$.

Much higher frequencies are achievable via additional optical dipole potentials. By squeezing the atomic cloud in between a long-range attractive evanescent wave and a short-range repulsive evanescent wave [Ham03] we could demonstrate trapping frequencies of up to 10 kHz. However, trap lifetimes were as short as 200 ms probably because of surface effects, since the average distance to the surface in a double-evanescent wave trap was only about 1 μm.

In an effort to create a tightly confining trap with long lifetime, we have implemented a standing wave surface trap. Ordinary standing-wave traps offer extremely high trapping frequencies, but loading such traps generally results in the occupation of multiple potential wells. In order to preserve the advantage of loading a single well, we designed a standing wave with a large lattice spacing by reflecting a laser beam from the surface under grazing incidence.

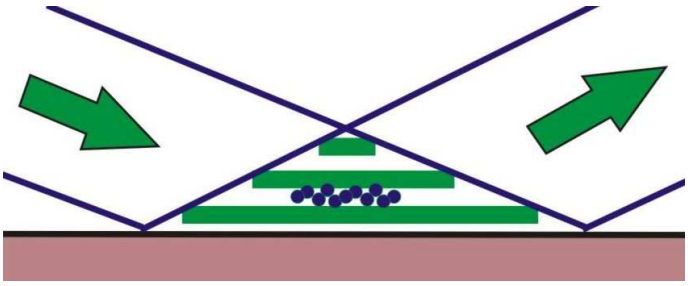

Figure 5.6: A standing wave trap is created by a repulsive laser beam that is reflected from the surface under grazing incidence. The atoms are vertically confined between the first two anti-nodes, while a dimple potential (not shown) ensures horizontal trapping.

The laser light is derived from a 'Verdi' laser at a wavelength of 532 nm. We couple out approximately 2 W, while the remaining 8 W are still sufficient to pump the Titanium-Sapphire laser which is used in the previous stages of the experiment. As usual, analog control of the light intensity is accomplished with an acousto-optical modulator. The beam is sent onto the surface at an angle of 3 degrees, which leads to a spacing between the potential wells of the standing wave of about 5 μm. We have chosen s-polarized light, since then the reflectivity of the dielectric surface is 82 per cent compared to 66 per cent in the case of p-polarization. Since a round laser beam would produce a very elongated spot on the prism under grazing incidence, cylindrical lenses are used for beam shaping. Close to the surface, the beam waist are 500 μm horizontally and 60 μm vertically. The far blue-detuned, repulsive light forms a standing wave with potential maxima at heights of 2.5 μm and 7.5 μm, which traps the atoms in between without any need for an additional evanescent wave. But since we are using blue-detuned light, we still rely on the dimple potential to provide horizontal confinement and to compensate the horizontal anti-trapping forces of the repulsive lattice. It would be possible to use a red-detuned high-power laser for the standing wave instead, and we point out that in contrast to ordinary standing waves, single-frequency lasers are not required. The close proximity of the reflecting surface will always lead to the desired interference effect as long as the coherence length of the laser is larger than a few ten micrometers, which is normally the case.

To load the trap, we apply our standard preparation sequence that leads to a disc-shaped atomic cloud on the evanescent-wave at a temperature of about 100 nK. Then the standing-wave power is ramped up in 100 ms with an accompanying upward ramp of the dimple potential to cancel the horizontal anti-trapping forces.

As a first check, we switch off the evanescent-wave and still retain the atom signal. Optical confinement in the upward direction is verified by application of a strong magnetic gradient which would lift the atoms up if only gravity would be present, and in fact the cloud remains trapped close to the surface. We measure a lifetime of about 10 s in the standing-wave trap, which is better than typical lifetimes in an evanescent-wave trap and by far exceeds the lifetimes obtained in the double-evanescent wave scheme [Ham02a].

As a convenient method to determine the vertical trapping frequency, we modulate the standing-wave intensity with a relative amplitude of about 10 per cent for 2 s and observe loss from parametric heating. Figure 5.7 shows a typical dip in the atom number when the modulation frequency is close to twice the trapping frequency. The factor of two reflects the fact that both upward and downward trapping forces are modulated. Note that there was no factor of two for the trapping frequency measurements presented in section 5.3, since a modulation of the evanescent-wave intensity only affects the bottom of the trap.

As expected, the vertical trapping frequency scales as the square root of the standing-wave power (see fig. 5.7) and we reach frequencies of up to 2.5 kHz. In principle, much stronger compression is conceivable for higher powers, with the caveat of correspondingly stronger horizontal forces. For a trapping frequency of 2 kHz, we could trap

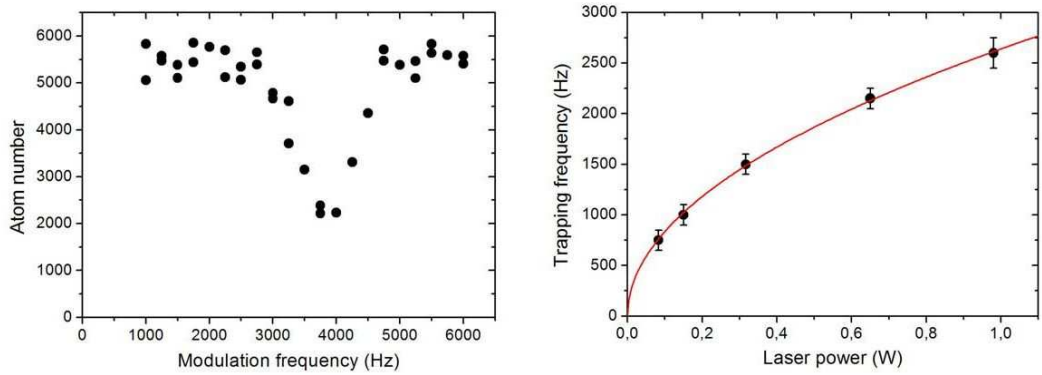

Figure 5.7: Trapping frequency measurements in the standing-wave surface trap. Left, typical loss dip due to parametric heating. Right, trapping frequencies up to 2.5 kHz are obtained, and the expected scaling with the square root of the laser power is confirmed.

1.0×10^4 atoms at a temperature of about 250 nK. As discussed in chapter 7, lower temperatures are desirable to observe confinement-induced modifications of three-body loss. Better conditions might be achievable after further optimization of the initial atom number and implementation of evaporative cooling in the standing-wave trap.

In conclusion, we have demonstrated a standing-wave surface trap and confirmed the expected tight confinement. The measured lifetime of 10 s should allow for further evaporative cooling and makes the trap a promising tool for the investigation of two-dimensional systems.

6 Efimov resonance and temperature shift

Cesium in its lowest internal state offers an abundant supply of broad and narrow Feshbach resonances [Ino98, Tie93, Chi04] at accessible magnetic field strengths. The scattering length a thus varies strongly with magnetic field and can be controlled within a wide range of negative and positive values with magnitudes of up to a few thousand Bohr radii a_0. The exceptional magnetic tunability of interactions was a main motivation for the technical efforts to provide fast and precise magnetic field control in our new setup. The absence of Eddy currents in our glass cell apparatus and careful coil construction and current stabilization have contributed to this goal. In this chapter, measurements on three-body loss at varying scattering lengths are presented that exploit the improved level of magnetic field control. Another key ingredient is the ability to prepare ultracold thermal cesium gases at moderate densities and temperatures as low as 50 nK. Because of these preconditions, our apparatus was well suited for the investigation of a three-body resonance that finally provided evidence for the long-standing theoretical prediction of Efimov quantum states.

6.1 Efimov's scenario

Interactions between particles often involve complicated potentials that are only roughly known for short distances between the particles. A characteristic range l of the two-body interaction potential sets the scale below which the details of the potential are important. In the ultracold limit, the s-wave scattering length a describes the scattering process of two particles. The two-body interaction is called resonant when $|a|$ greatly exceeds the characteristic range l. In this case, the long-range nature of the wavefunction renders the details of the short-range potential irrelevant. It is then possible to obtain universal theoretical results that apply to a wide variety of physical systems as long as the assumption of resonant interaction holds.

As an example for universality in the resonance regime, a weakly bound dimer state exists for large positive scattering lengths. Its binding energy is given by the universal expression $E_b = -\hbar^2/(ma^2)$, where m is the atomic mass and $\hbar$ Planck's constant divided by 2π. The mere dependence on a reflects the fact that two-body physics is completely characterized by the scattering length for resonant interactions. In fig-

ure 6.1, the resonance limit is approached as $1/a$ tends to zero, and the dimer energy is represented by a parabola for $a > 0$.

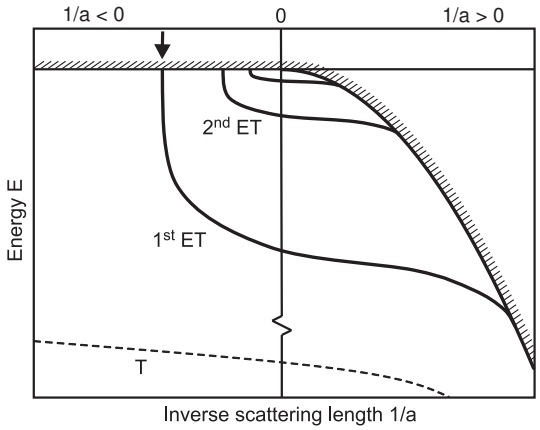

Figure 6.1: Scheme of Efimov's scenario [Kra06b]. Resonant interactions are present close to $1/a = 0$ and yield a series of Efimov trimers (ET). Efimov states are weakly bound and connect to the scattering continuum on both sides of the resonance, as opposed to a regular deeply-bound trimer state (T).

When a third atom is added, the parabola E_b marks the threshold to the dimer-atom continuum at positive scattering lengths, while states with lower energy are necessarily bound trimer states. At negative scattering lengths, weakly bound dimers do not exist. Therefore, only three-body bound states are present at negative energies, while states with positive energy can dissociate into three free atoms. In this context, Efimov has found theoretically a series of bound three-body states with universal properties [Efi70, Efi71, Bra06] arising as a consequence of resonant two-body interactions. The energy of these states is plotted as a function of $1/a$ in figure 6.1. When $1/a$ approaches the resonance from the negative-a side, a first Efimov trimer appears at the three-atom threshold ($E = 0$). Passing through the resonance region, the state connects to the positive-a side, where it finally intersects with the atom-dimer threshold ($E = E_b$). An infinite series of such Efimov states appears at even smaller binding energies when scattering lengths are increased and binding energies are decreased in powers of universal scaling factors $\exp(\pi/s_0) \approx 22.7$ and $\exp(-2\pi/s_0) \approx 1/515$ (with $s_0 = 1.00624$).

Efimov's prediction strongly affects scattering processes in the resonance region. At negative scattering lengths, three free atoms can couple to an Efimov trimer when the trimer intersects the continuum threshold. This gives rise to a triatomic Efimov resonance. A similar situation emerges for positive scattering lengths when the trimer hits the atom-dimer threshold and a resonance occurs for collisions between atoms and dimers.

6.2 Three-body loss equations

A simple experimental signature of a triatomic Efimov resonance is trap loss due to enhanced three-body recombination. Resonant coupling of three colliding atoms to an Efimov state leads to increased loss because the Efimov trimer quickly decays into deeply bound dimer states plus a free atom. Therefore, measurements on three-body recombination at varying scattering length can be used to probe Efimov's resonance scenario. As a tool to extract recombination rates from loss measurements, we introduce a model that describes the time evolution of the atom number and temperature in a trap.

When ultracold atoms are held in a trap for some time, the atom number decreases due to various loss mechanisms. The simplest contribution to the loss comes from imperfections of the trap, e.g. leaks in the trapping potential, photon scattering, or the presence of residual background gas in the vacuum system. In this case, the probability for an atom to be ejected from the trap is independent of the density of surrounding atoms. Such one-body effects lead to a simple exponential decay of the density and atom number. Introducing the one-body decay rate α we can write $\dot{n} = -\alpha\, n$ for the density, and after integrating over the volume, $\dot{N} = -\alpha\, N$ for the atom number.

While improving the quality of the trap to avoid one-body decay is a mainly technical challenge, there will still be loss processes involving collisions of two or more atoms at a time. The probability of an atom to be lost then depends on the presence of other atoms nearby, i.e. on the local density. This leads to non-exponential decay described by the equations $\dot{n} = -L_2\, n^2$ and $\dot{n} = -L_3\, n^3$ for two- and three-body loss, respectively.

A straight-forward strategy to suppress density dependent loss is to keep the density low. In fact, ultracold gases are never stable in the long run, since the ground state of the system would be a solid. But as inelastic collision processes are suppressed at low densities, ultracold gases can be held in a metastable state. For measurements of inelastic loss, the ability to control the speed of the decay via the density facilitates the determination of loss rates that vary over many orders of magnitude.

For reliable rate measurements it is is crucial to experimentally differentiate between the contributions from two-body and three-body loss. Exponential one-body loss can be identified as the loss rate at very low densities. But analyzing the non-exponential part of the decay in general gives unreliable fitting values for L_2 and L_3, as the respective decay curves do not differ much. Inelastic two-body loss takes place when the atoms gain energy by changing their internal state in a collision process. Obviously, polarizing the atoms into the internal state with the lowest energy prevents two-body loss. However, this is only possible in optical dipole traps, because the lowest state can not be trapped magnetically. In magnetic traps, both two- and three-body loss will be present, and reliable measurements of loss coefficients are only possible in exceptional cases [Bur97, Söd99].

The absence of inelastic two-body collisions in our optical dipole traps makes three-body recombination the dominant loss mechanism under normal experimental con-

ditions. Two atoms form a bound state during a collision of three particles, and the release of the binding energy ejects the particles from the trap. Note that the presence of the third particle is necessary to fulfill energy and momentum conservation. Integrating the loss rate equation $\dot{n} = -L_3\, n^3$ over the volume gives $\dot{N}/N = -L_3\, \langle n^2 \rangle$. Here, $\langle n^2 \rangle$ is the average squared density seen by a given probe particle and measures the probability of the probe particle to encounter two other nearby particles.

In a box potential of volume V, the average squared density $\langle n^2 \rangle$ equals $(N/V)^2$ and is independent of the temperature of the ensemble. Neglecting any temperature dependence of L_3 then gives the differential equation $\dot{N}/N = -L_3\, (N/V)^2$ for the decrease in particle number, which can be solved by separation of variables.

The situation is different for inhomogenous systems, because then the average squared density depends on the temperature of the atomic cloud. When three-body decay leads to a rise in temperature, the accessible trapping volume gets larger and therefore the density decreases. For a three-dimensional harmonic trap, with $\bar{\omega}/2\pi$ denoting the geometrical mean of the trapping frequencies, we get $L_3 \langle n^2 \rangle = \gamma N^2/T^3$ with $\gamma = L_3 m^3 \bar{\omega}^6 / \left(8\pi^3 k_b^3 \sqrt{27}\right)$. The dependence on the third power of the temperature is so strong that it is essential to include the time evolution of the temperature in the decay model. Neglecting this effect can lead to fitting results for L_3 which greatly deviate from the correct value.

In general there are two contributions to the heating due to three-body loss. The first one is anti-evaporation heating and comes from the fact that the loss occurs preferentially in the center of the trap, where the density is highest. However, the atoms in this region tend to have energies which are below average. In a harmonic trap, atoms undergoing three-body collisions have an average potential energy $k_B T/2$, while the ensemble average is $3k_B T/2$. The loss of an atom thus leaves an extra energy of $k_B T$ in the remaining ensemble.

The second contribution to the heating during three-body loss is called recombination heating. Normally, the binding energy of the formed molecule is so large that the molecule and the third atom are quickly lost from the trap. However, at large positive scattering lengths, the binding energy $\hbar^2/(ma^2)$ might be so small that the third atom remains trapped for a sufficiently long time, and then deposits some of its extra energy in the sample via elastic collisions with other atoms. We denote this possible extra energy per lost atom by T_h.

The combined effect of anti-evaporation and recombination heating leads to an additional energy per lost atom of $k_B(T + T_h)$. After thermalization, the relative increase in temperature per lost atom is then given by dividing the extra energy by the average energy $3k_B T$. Multiplication with the loss rate yields the rate of temperature change.

In summary, we model the time evolution of atom number and temperature in our

traps with the following equations:

$$\frac{1}{N}\frac{dN}{dt} = -\alpha - \gamma\frac{N^2}{T^3} \tag{6.1}$$

$$\frac{1}{T}\frac{dT}{dt} = \gamma\frac{N^2}{T^3}\,\frac{T+T_h}{3T} \tag{6.2}$$

We aim at fitting the model parameter $\gamma \sim L_3$ to our experimental data. In principle, this can be done by numerically solving equations 6.1 and 6.2 while varying the parameters α, γ and T_h until the best fit to the data is reached [Web03a, Web03b]. We will show now how to obtain analytical solutions, which provide further insight and simplify the data analysis.

The model equations 6.1 and 6.2 represent a coupled system of ordinary first-order differential equations. The system is non-linear, and therefore no standard solving techniques apply. However, the structure of the equations is simple enough to allow for analytic integration. It is clear that two integrations are necessary to obtain solutions for $N(t)$ and $T(t)$.

The term $\gamma N^2/T^3$ appears in both equations 6.1 and 6.2, since it describes the probability of a probe particle to be involved in a three-body recombination event in one time unit. Using equation 6.2 to substitute this term in equation 6.1 gives:

$$\frac{1}{N}\frac{dN}{dt} = -\alpha - \frac{3}{T+T_h}\frac{dT}{dt} \tag{6.3}$$

It is now possible to integrate this equation in closed form, and with N_0 and T_0 denoting the initial atom number and temperature we get

$$\log\left(\frac{N}{N_0}\right) = -\alpha t - 3\log\left(\frac{T+T_h}{T_0+T_h}\right) \tag{6.4}$$

or equivalently

$$\frac{N}{N_0} = \left(\frac{T_0+T_h}{T+T_h}\right)^3 \exp\left(-\alpha t\right) \tag{6.5}$$

This equation describes the central relationship between the time evolution of the particle number and the temperature of the ensemble. When either N or T is observed over time, the other quantity can be determined from equation 6.5. We emphasize that this first integral of the differential equations 6.1 and 6.2 does not rely on any simplifying assumptions and holds for all values of α,γ and T_h.

With α known from low-density measurements or negligible, equation 6.5 could be used to determine the recombination heat T_h after recording both the decay of the particle number and the rise in temperature as a function of the trapping time.

In our experiments, we have mainly measured decay curves at negative scattering lengths, where no weakly bound dimer state is available. Three-body recombination then only involves deeply bound dimer states, and the released binding energy is so

large that the molecule and the third atom are immediately expelled from the trap. Therefore the process of recombination heating is absent and we can set T_h equal to zero. Compared to the dramatic three-body loss at negative scattering lengths, the one-body loss rate α is mostly negligible as well. The relation 6.5 then simplifies to $N \sim T^{-3}$, which is useful for quick estimates on the expected heating for a given reduction in atom number. For example, a loss of 30 percent in atom number will be accompanied by a relative increase in temperature of about 13 percent.

In order to solve the system 6.1 and 6.2, a second integral is still missing. From now on we restrict the calculation to the case of vanishing T_h, which is justified at negative scattering lengths, and later take a short look at the general case with $T_h \neq 0$. The first integral 6.5 relates N and T and can be used to eliminate T from equation 6.1, or alternatively to eliminate N from equation 6.2. It turns out that the calculation proceeds slightly easier with equation 6.2, which then reads

$$\frac{1}{T}\frac{dT}{dt} = \frac{\gamma}{3}\frac{1}{T^3}N_0^2\left(\frac{T_0}{T}\right)^6 \exp\left(-2\alpha t\right) \tag{6.6}$$

After separation of variables and integration we get

$$\frac{1}{9}\left(T^9 - T_0^9\right) = \frac{\gamma}{3}N_0^2T_0^6\frac{1}{2\alpha}\left(1 - \exp\left(-2\alpha t\right)\right) \tag{6.7}$$

Substituting this solution for T into relation 6.5 finally gives the full solution for N and T in the case of vanishing T_h:

$$\frac{N}{N_0} = \left(1 + 3\gamma N_0^2T_0^{-3}\frac{1}{2\alpha}\left(1 - \exp\left(-2\alpha t\right)\right)\right)^{-1/3}\exp\left(-\alpha t\right) \tag{6.8}$$

$$\frac{T}{T_0} = \left(1 + 3\gamma N_0^2T_0^{-3}\frac{1}{2\alpha}\left(1 - \exp\left(-2\alpha t\right)\right)\right)^{1/9} \tag{6.9}$$

When the one-body loss rate α is negligible, the solutions further simplify due to $\left(1 - \exp\left(-2\alpha t\right)\right) / \left(2\alpha\right) \cong t$.

We now turn to the general case $T_h \neq 0$ and follow the same steps as in the previous calculation. The left hand side of equation 6.7 then becomes a more general polynomial of ninth order, with powers of T_h as coefficients. The inverse of such a polynomial has no representation in terms of elementary functions. After all, the solution $T(t)$ can be given implicitly via a closed-form representation of its inverse function $t(T)$.

Equations 6.8 and 6.9 are the solutions to the coupled differential equations 6.1 and 6.2 for negligible T_h. Since the differential equations can be solved numerically as well, what are the analytical solutions good for? First, numerical calculations do not provide the same insight into the structure of the solutions. For example, the simple scaling law $N \sim T^{-3}$ for small α and T_h might easily be overlooked. Second, the numerical implementation of solving the differential equations with varying fitting parameters is tedious, especially with regards to a thorough treatment of fitting errors.

It is much simpler to use equations 6.8 and 6.9 in a standard nonlinear fitting routine[1]. In the general case $T_h \neq 0$, numerical procedures are necessary. However, the first integral 6.5 is still valid and should be used to eliminate the coupling between the model equations 6.1 and 6.2, which simplifies the numerical implementation.

We end the discussion of the model with a cautionary remark on some hidden assumptions. The trap is assumed to be deep enough so that evaporative loss does not occur, even after significant heating due to three-body loss. The model also presumes thermal equilibrium during the decay, which can be questionable for the dramatic loss close to a resonance. It is then helpful to work at lower densities, which suppresses three-body effects more strongly than elastic two-body collisions. Finally, the model does not take into account any temperature dependence of the decay rate constant, i.e. the variation of L_3 with temperature is assumed to be negligible.

6.3 Loss rate measurements

This section presents our measurements on three-body loss at varying magnetic fields. In the range of negative scattering lengths, a dramatic loss resonance is observed.

Every experimental cycle starts with the preparation of an ultracold atomic gas in the surface trap. We apply our standard sequence of loading the MOT, transfer into the hollow beam trap with subsequent Sisyphus cooling on the evanescent wave, loading of the dimple trap, optical pumping and then forced evaporative cooling. During evaporation, the magnetic field is set to 27 G in order to obtain a moderate positive scattering length of 450 a_0. We typically end up with samples of 6000 atoms at a temperature of 250 nK. The trapping frequencies in the final optical trap are 550 Hz in the vertical direction and 36 Hz in the horizontal directions. Under these conditions, the peak density of the atomic cloud is about $1.1 \times 10^{12}\,\mathrm{cm}^{-3}$.

The timing sequence then proceeds with a jump in the magnetic field to the desired value. At this value, we then measure the decay curve by recording the remaining atom number at variable hold times. In our experiment, we can not record the time evolution of the temperature during the decay. A reliable temperature measurement takes too long, since our low atom numbers require a lot of averaging. Our approach is based upon extracting the initial slope of the decay curve of the atom number, while making sure that the density and temperature are approximately constant during the short measurement time. In the limit of an infinitesimal time interval, this approach would directly yield the initial time derivative of the decay. For an evaluation of errors, we make use of the trap loss equations described in section 6.2.

Instead of choosing a fixed time interval, we have adapted the maximum hold time to the strength of loss at the particular magnetic field value. This was done by imposing the requirement of a maximum relative loss of 10 per cent in particle number. For the strong loss observed close to 7 G, we had to restrict the hold times to below 20 ms,

[1] e.g. in Origin

while up to 200 ms were acceptable for other magnetic field values. Figure 6.2 shows a typical decay curve together with the regression line obtained with a standard linear fitting routine. Since the shot-to-shot variation in atom number is comparable to the maximum allowed loss of 10 per cent, some statistical averaging is needed before reliable fitting values for the decay slope are obtained.

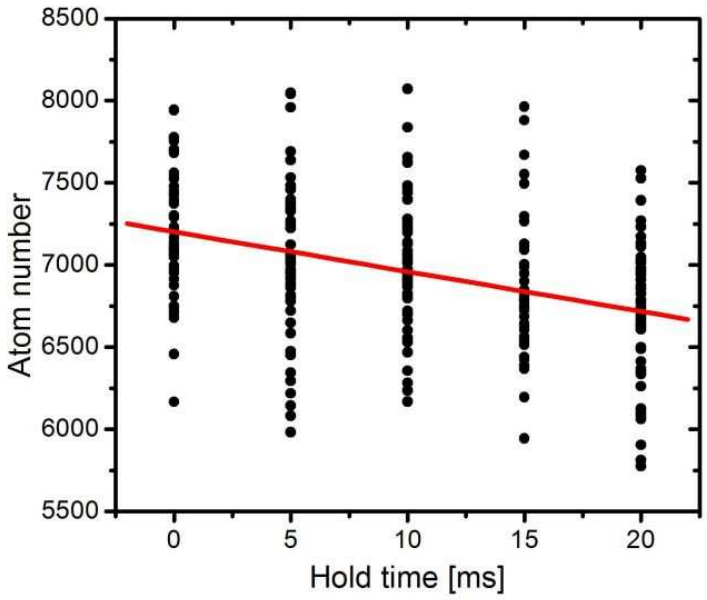

Figure 6.2: Decay of particle number at a magnetic field of $B = 2.02\,\mathrm{G}$, with the straight line resulting from linear regression. The measurement comprises 243 individual data points.

For an estimate of the error that is introduced by approximating the non-linear decay as described in section 6.2 with a linear fitting function, let us consider the change in slope after a loss in particle number of 10 per cent. It is clear that the decay slows down due to a reduction in density which is caused by both the decrease in particle number and a rise in temperature. We calculate the rise in temperature with the scaling law $N \sim T^{-3}$ obtained from equation 6.5 by neglecting T_h and α. This is justified at negative scattering lengths, where recombination heating is absent and where three-body loss in our trap takes place on a timescale of below 200 ms, while the one-body lifetime is many seconds. Equation 6.1 then gives $\dot{N} \sim N^4$, and it follows that the slope of the decay curve after losing 10 per cent of the atoms is reduced by about 35 per cent. As we can expect the linear fitting routine to yield an average between the maximal initial slope and the minimal final slope, we take into account a possible downward shift of 20 per cent of the measured value with respect to the actual initial slope.

We present our decay rate measurements in table 6.1. The data was taken on five days in September 2005, and is shown in chronological order with horizontal lines separating different measurement days.

B (G)	N_0 (mV)	M (mV s^{-1})	R	N	$-M/N_0$ (s^{-1})	n_0 (10^{12} cm^{-3})	L_3 (10^{-24} cm^6 s^{-1})
29.74	159(2)	-69.5(14.7)	-0.36	153	0.44	1.10	-
24.71	147(2)	-62.8(16.3)	-0.28	173	0.43	1.02	-
15.70	135(2)	-65.7(22.1)	-0.24	141	0.49	0.93	0.2(2.3)
10.00	130(3)	-93.9(49.4)	-0.21	84	0.72	0.90	1.7(4.1)
7.70	132(2)	-512(78.3)	-0.53	108	3.87	0.92	21.2(8.0)
4.84	132(2)	-202(51.1)	-0.31	152	1.53	0.91	6.8(4.7)
13.00	129(2)	-52.8(14.2)	-0.27	174	0.41	0.90	-0.3(2.0)
9.00	133(2)	-345(57.1)	-0.53	93	2.60	0.92	13.3(5.8)
6.19	132(1)	-318(35.7)	-0.59	150	2.41	0.91	12.2(4.7)
7.70	158(1)	-1325(204)	-0.48	147	8.38	1.31	23.9(8.1)
3.50	157(1)	-375(104)	-0.27	244	2.39	1.30	5.9(3.5)
2.02	159(1)	-536(85.1)	-0.38	243	3.36	1.32	8.6(3.4)
1.00	157(1)	-494(86.8)	-0.33	276	3.14	1.31	8.2(3.5)
9.00	159(1)	-559(62.5)	-0.53	207	3.51	1.32	9.1(3.1)
24.71	159(1)	-70.6(8.3)	-0.40	375	0.44	1.32	-
6.19	145(2)	-471(95.3)	-0.42	116	3.25	1.25	9.3(4.2)
18.58	144(2)	-61.3(14.8)	-0.29	194	0.42	1.25	-
10.00	145(2)	-235(63.0)	-0.34	107	1.63	1.25	3.9(2.7)
12.00	141(2)	-129(40.4)	-0.26	138	0.91	1.22	1.6(2.0)
1.00	129(1)	-372(101)	-0.26	195	2.89	0.89	16.0(8.9)
24.71	127(2)	-58.3(18.0)	-0.31	99	0.46	0.88	-
39.74	138(2)	-58.1(18.1)	-0.23	179	0.42	0.95	-
65.00	127(2)	-70.1(27.3)	-0.23	116	0.55	0.88	-
65.00	148(2)	-183(37.4)	-0.44	100	1.24	1.19	-
65.00	152(2)	-77.8(27.2)	-0.17	274	0.51	1.22	-
17.00	137(2)	-68.5(16.5)	-0.34	133	0.50	1.11	-
6.68	136(1)	-434(74.8)	-0.47	122	3.19	1.10	11.8(4.9)

Table 6.1: Decay rate measurements at various magnetic field values

The first column indicates the magnetic field value that was held during the decay. The atom number signal was obtained by recapture into the MOT and subsequent fluorescence detection with an amplified photodiode. The signal was calibrated with absorption images, with a resulting calibration factor of 45.17 atoms/mV. Typical initial atom numbers were 6000 atoms, providing a voltage signal level of about 130 mV. The columns N_0 and M give the initial signal and the slope of the linear regression line as shown in figure 6.2. The stated uncertainties are the statistical standard errors as obtained from the fit. The next columns show the correlation coefficient R and the number of individual data points N.

M/N_0 gives the ratio of slope and initial signal, and represents the experimental value of $\frac{1}{N}\frac{dN}{dt}$. The peak density n_0 plays a crucial role when calculating decay constants. It is determined from the given values of atom number, trapping frequencies and temperature. The temperature was measured on each of the five days, with the following results and statistical fitting errors: 280(30) nK, 250(30) nK, 240(20) nK, 280(50) nK, 250(20) nK.

A closer look at the column of relative slope M/N_0 reveals that for magnetic fields larger than 17 G, i.e. for positive scattering lengths, the relative slope is almost constant and assumes values close to $-0.45\,\mathrm{s}^{-1}$. (An exception is the second measurement at 65 G with a much larger value for the relative slope, but repeating the measurement with better statistics confirmed the expected smaller value.) The observed constant loss can not be attributed to three-body recombination, since the rates should vary strongly with magnetic field and should be negligible at our moderate peak densities [Web03b]. We can also exclude residual evaporative loss because of the missing variation with scattering length. The observed loss rate corresponds to a lifetime of 2.2 seconds and is still smaller than the one-body lifetime of about 6 seconds. An explanation for this difference would be a loss contribution from 'blue collisions', i.e. the collision of two atoms accompanied by the absorption of a photon from the blue-detuned evanescent wave [Jon06]. The excitation of repulsive molecular states expels the atoms from the trap and gives rise to two-body loss. Since the observed loss presents only a small offset, we simply subtract $0.45\,\mathrm{s}^{-1}$ from all relative slope measurements and give a generous error range of $\pm 0.15\,\mathrm{s}^{-1}$. This error range also takes into account the slight variations in peak density which affect the expected two-body rates. Admittedly, the rate of blue collisions might depend on the scattering length because of changes in the wavefunction overlap factors. However, we only observe a minor variation at positive scattering lengths and do not expect a dramatically different behavior at negative scattering lengths.

The offset subtraction presents a small correction for the loss rate measurements at large negative scattering lengths. Table 6.2 reveals that we are able to calculate reliable three-body rates for magnetic field values below 10 G. The rate coefficient L_3 is obtained by division of the corrected M/N_0 values by the average squared density $n_0^2/\sqrt{27}$.

The error of M/N_0 is determined by the statistical uncertainty in the slope M, while the small variation in the initial atom number N_0 can be neglected. In order to account for the uncertainty that is introduced by subtracting the offset, we first consider the lower value $(M - \Delta M)/N_0$ for the relative slope and subtract the upper value $(0.45 + 0.15)\,\mathrm{s}^{-1}$ of the offset and thus obtain a lower limit for the corrected relative slope values. The upper limit corresponds to the upper value $(M + \Delta M)/N_0$, raised by 20 percent to account for the possible downward shift of the linear approximation, and then diminished by the lower offset $(0.45 - 0.15)\,\mathrm{s}^{-1}$. This error range then determines the relative error for the corrected M/N_0 values.

Additional uncertainty comes from the division by the squared density. We first take into account statistical fluctuations due to unobserved drifts in temperature during a

measurement day. Because the squared density is proportional to T^{-3}, allowing for 10 per cent of relative drift in temperature translates to a 30 per cent relative error for n_0^2. This error is then quadratically added to the relative error of the corrected M/N_0 values in order to obtain the statistical relative error for L_3. In table 6.1, the corresponding absolute error ranges for L_3 are given.

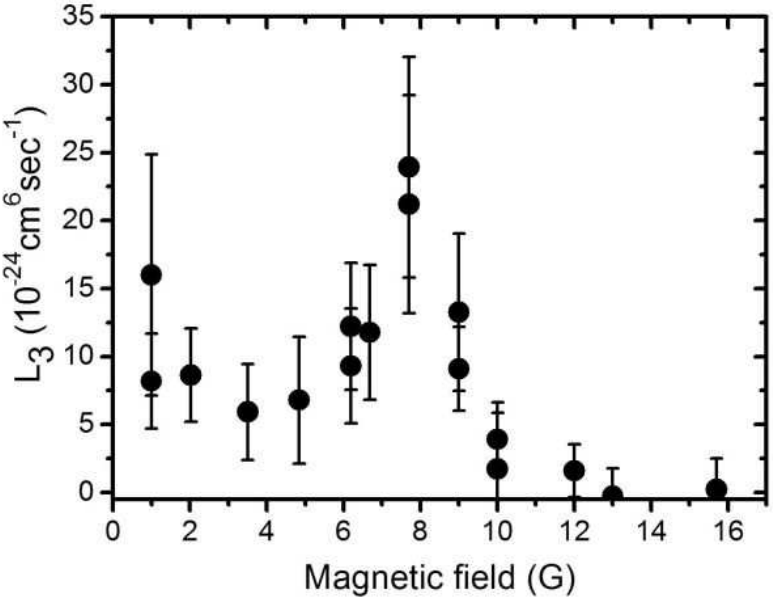

Figure 6.3: Three-body loss rate coefficient L_3 for magnetic fields between zero and 17 G, which is the range of negative scattering lengths.

The error bars in figure 6.3 only indicate statistical errors. We now consider the systematic uncertainty in the density which affects the calibration of the L_3-axis in figure 6.3. The quadratic density is proportional to the product of the squared trapping frequencies $(\nu_x\nu_y\nu_z)^2$. The frequencies are determined to $\nu_z = 550(50)$ Hz and $\nu_{x,y} = 36(4)$ Hz, and we assume independent deviations from the measured values in the three directions. The 10 per cent error for each frequency then translates to $\sqrt{3} \times 20 \simeq 35$ percent error of the squared density. In addition, the measurement of atom numbers is calibrated with absorption images with an estimated uncertainty of 50 per cent. In total, the calibration of the L_3 axis in figure 6.3 should be accurate to within a factor of 3. This systematic uncertainty does not affect the lineshape and position of the observed loss peak.

In conclusion, our measurements of three-body recombination rates in the magnetic field range from 0 to 17 G clearly show a pronounced resonance close to 7.5 G. At maximum, extremely large rate coefficients on the order of $2 \times 10^{-23}\,\mathrm{cm^6 s^{-1}}$ are observed. Our measurements were performed at a temperature of 250 nK and agree with data from another cesium experiment in our group. The other experiment could ad-

ditionally provide measurements at temperatures as low as 10 nK and identify a loss minimum at positive scattering lengths [Kra06b]. In total, these findings have led to the conclusion that the observed loss resonance at 7.5 G is due to an Efimov state crossing the scattering threshold. The complete experimental evidence is presented in [Kra06a].

6.4 Temperature shift

The Efimov resonance was observed at a magnetic field value of about 7.5 G, where the scattering length is about $-850\,a_0$. In a further investigation, we have performed accurate measurements of the resonance position at various temperatures. As a result, a significant shift with temperature could be observed. The data provides quantitative insight into the behavior of an Efimov state diving into the three-atom continuum.

To illustrate this effect, Figure 6.4 shows a bound Efimov state close to the three-atom continuum. We only consider negative scattering lengths, where weakly bound dimers are absent. With increasing scattering length, the binding energy of the Efimov trimer gets smaller until it vanishes at a_-, where the state hits the three-atom threshold. At this position, an Efimov resonance would occur in the limit of zero collision energies. For larger scattering lengths, the Efimov state evolves into a triatomic continuum resonance [Bri04] that can dissociate into three free atoms. Conversely, three free atoms can couple to the resonance state which then decays to a deeply bound dimer and an atom and thus enhances three-body recombination. At non-zero temperatures, resonant conditions are fulfilled at a scattering length slightly upshifted from a_- due to the available collision energy E_{coll} and the finite slope of the resonance state.

The right hand side of figure 6.4 shows again our measurements of three-body loss rates at a temperature of 250 nK (see section 6.3). We denote the position of maximum loss by a_{max}, which differs from a_-. When the temperature is reduced, a_{max} shifts and approaches a_- in the zero-energy limit. The shift is small and does not exceed the width of the loss peak.

For precise determinations of a_{max}, it is essential to note that actual rate measurements are not necessary. Simple measurements of remaining atom numbers after a fixed hold time are sufficient. Because the number of lost atoms depends monotonously on the loss rate coefficient L_3, the position of a minimum in the remaining atom number coincides with the position of maximal L_3. As there is no linear relationship in the case of large loss fractions, the lineshape and width of the resonance signal will be different, but the position of the extremum will be the same. Therefore it is possible to accurately determine a_{max} without the need to perform elaborate rate measurements and careful density calibrations.

Every experimental cycle starts with the preparation of ultracold cesium via the methods discussed in chapter 5. As a final cooling step, we perform evaporative cooling in a partially levitated surface trap. A homogenous magnetic field of 27 G is applied to tune the scattering length [Chi04] to the moderate positive value $450\,a_0$, which proved to yield the best evaporation results. The magnetic gradient used to compen-

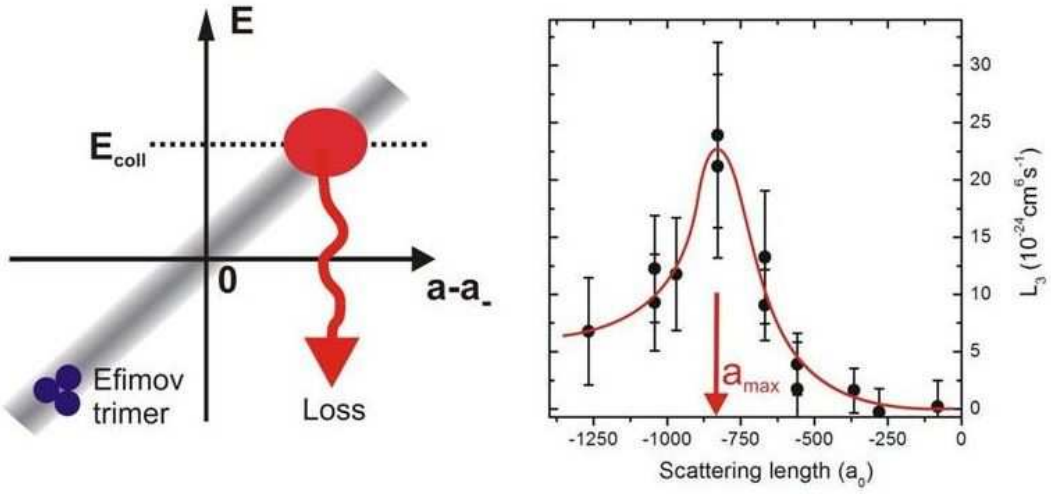

Figure 6.4: Left, schematic view of a bound Efimov state crossing the three-atom threshold at the position a_- and evolving into a continuum resonance. Right, our recombination rate measurements at a temperature of 250 nK with a line to guide the eye. The position of maximum loss a_{max} shifts with decreasing temperature and approaches a_-.

sate gravity is still present during evaporation and then slowly ramped down within 500 ms. After plain evaporation has died away within another 200 ms, the atomic sample is ready for the actual measurement procedure. We typically operate with a few thousand atoms at temperatures in the nanokelvin range which can be set via the evaporation depth.

The measurement procedure begins with a jump in the magnetic field to a value close to the resonance position at about 7.5 G. The field is held constant for 17 ms while atoms are lost due to three-body recombination. We then switch off the magnetic field and immediately take an absorption image to record the remaining atom number. We repeat this procedure with randomly varying values of the magnetic field in order to search for a minimum in the remaining atom signal.

An accurate determination of the minimum position requires averaging over many repetitions of the experimental cycle to reduce the statistical fluctuations of the atom number signal. After reading off an approximate value for the minimum position, we extract its precise location and statistical error by fitting a parabola to the data points in the vicinity of the minimum (see fig.6.5). The fitting parameters are the center position, the curvature and the offset of the parabola. We expect the center position to coincide with the position of the minimum as long as a sufficiently narrow magnetic field range close to the minimum is used for the fit. The field range can be validated by looking for changes in the fitting parameters when the range is further restricted. Note that the position of the minimum is determined without making assumptions on the lineshape of the loss signal. As a cautionary remark, we point out that it is not possible to directly interpret the curvature of the parabolic fits in terms of the resonance width since the

loss signal is not simply proportional to the decay rates.

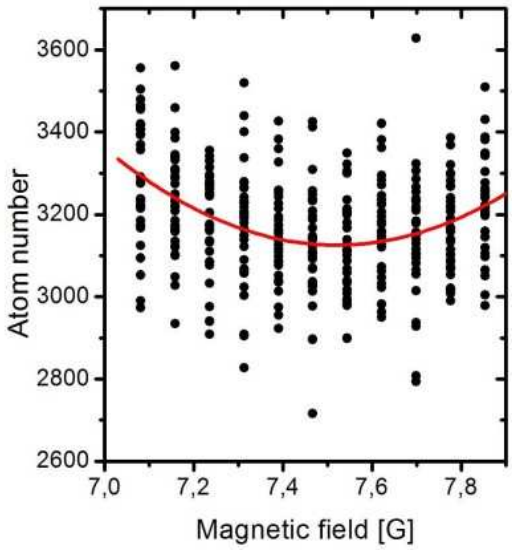

Figure 6.5: Remaining atom number for magnetic fields close to the resonance. The parabolic fit yields the position of the minimum, in this case 7.52(2) G. The dataset is comprised of 350 points, recorded within a measurement time of 100 minutes.

The dramatic three-body loss on resonance leads to experimentally challenging conditions. We have carefully optimized our current control circuit for the coils to obtain a fast jump in the magnetic field. The desired current value is reached within less than a millisecond and then held with an accuracy of better than two percent during the 17 ms measurement time. Close to resonance, the scattering length varies with the magnetic field with a slope of $133\,a_0/\,\mathrm{G}$. Thus, the calibration uncertainty of the magnetic field due to the settling time of the control circuit translates into a possible systematic offset of $\pm 15\,a_0$ in the determination of scattering lengths. We point out that we benefit from the absence of eddy currents in our glass cell apparatus, which would otherwise hamper the creation of precise jumps in the magnetic field. A straight-forward way to relax the requirements of fast magnetic field control is to reduce the atomic density and thus to slow down three-body loss. For this reason, our measurements at the lowest temperatures were performed near the detection limit with as few as 1000 atoms. Typical peak densities were below $5 \times 10^{11}\,\mathrm{cm}^{-3}$.

We have determined the magnetic field value of maximum loss for temperatures in the range from 500 nK down to 44 nK. As a result, we observe the peak position to shift from 7.7 G at high temperatures to 7.4 G for the lowest temperature. Figure 6.6 presents the data after conversion of the magnetic field values to the corresponding scattering lengths [Chi04]. The loss peak shifts from $-825\,a_0$ down to $-872\,a_0$ for the coldest samples. Two data points have been measured after deep evaporation followed by a recompression ramp that increased the trapping potential by a factor of three within 900 ms. The results are consistent with the measurements in uncompressed

traps and show that plain evaporation is absent. The vertical error bars indicate the statistical uncertainty from the parabolic fitting procedure. The horizontal error bars take into account the uncertainty of the temperature measurements and the expected rise in temperature that accompanies the loss [Web03b].

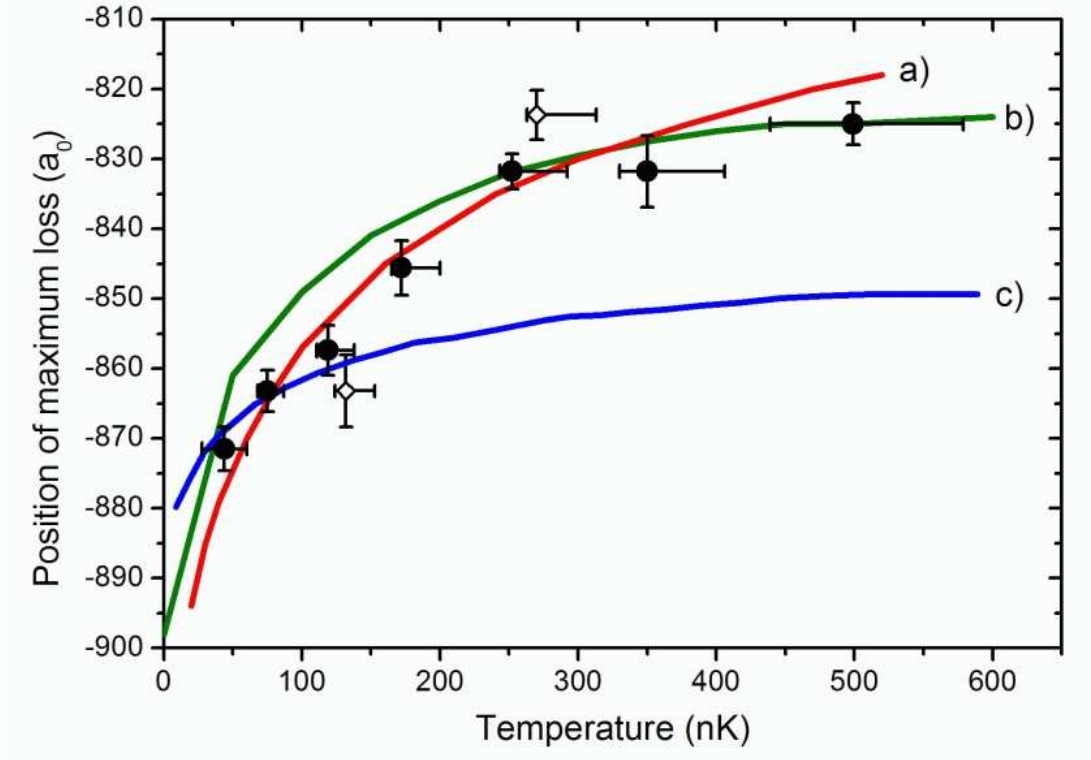

Figure 6.6: Position of maximum three-body loss a_{max} for different temperatures of the atomic sample (filled circles). Two data points were measured after recompression of the optical trap (open diamonds). The solid curves represent theoretical calculations: a) [Esr], b) [Yam], c) [Jon]

We compare our measurements with several calculations that extend the theory of three-body recombination [Bra06, Fed96, Nie99, Esr99, Bed00, Bra01] to non-zero collision energies. Theoretical treatments [Jon, Yam] need to take into account the energy and width of the continuum resonance in dependence of the scattering length, thermal averaging and the effect of the unitarity limit [D'I04]. In figure 6.6, the solid lines represent three independent theoretical calculations. Curve a) is based on the model of [Jon] and nicely agrees with our data. A slight adjustment of the fitting parameter a_- was allowed, while changes in the parameter $\eta = 0.06$ had little effect. Curve b) shows the results of [Yam] with a preliminary fit to our data. Curve c) is based on a numerical approach [Esr] with a single fit parameter.

Models a) and b) are in good agreement with our measurements. The sign of the shift is clearly correct. The magnitude of the shift and also the shape of the curve

with its saturation behavior at high temperatures are well reproduced. Curve c) takes a similar form, although it somewhat underestimates the size of the shift. In summary, our measurements agree with calculations on the basis of Efimov's theory and allow for a valuation of different theoretical treatments.

We point out that figure 6.6 was obtained by selecting a temperature value T_0 on the horizontal axis and then measuring the position of maximum loss a_0. In a different interpretation, selecting a_0 on the vertical axis and varying the temperature would lead to a maximum loss rate at T_0. This interpretation is reminiscent of collider experiments, where a chosen particle species with given interactions is examined in a range of collision energies. In our case, measurements at fixed magnetic field with varying evaporation depth are hampered by the necessity to take into account the changes in atom number and density when the evaporation ramp is varied.

In conclusion, we have studied a shift in the position of an Efimov resonance in ultracold cesium when the temperature of the gas is varied. The position of maximum loss shows a significant shift which can be understood on the basis of theoretical calculations extending Efimov's results into the scattering continuum at non-zero collision energies.

7 Conclusion and Outlook

This last chapter briefly draws the conclusions from our experimental achievements and gives an outline of promising future directions of research.

Conclusion

In a major technical effort we have updated the vacuum system of our experiment by replacing the old stainless steel chamber with a glass cell. A special epoxy seal was used to integrate a custom-made prism into the cell, and we are content with the performance of the seal that allowed for trapping lifetimes of 14 s. The updating process has led to three main improvements as compared to the traditional setup: an improved quality of the superpolished prism surface, better optical access, and faster magnetic field control.

Against our hopes, the improvement in polishing quality has not led to more efficient evaporation in the surface trap. It seems that the performance of evaporation is still limited by the presence of defects on the surface, and probably a different strategy needs to be implemented in order to obtain large Bose-Einstein condensates. However, we were able to reliably reach temperatures below 50 nK in thermal cesium gases, which was crucial for our investigation of an Efimov resonance.

While optical access was clearly a limiting factor in the old setup, the glass cell apparatus now provides ample space for additional devices or laser beams. We have made use of the improved access by implementing a standing-wave surface trap, and demonstrated tight confinement and long lifetimes in this novel trapping scheme. After upgrading the laser power and improving the initial atom numbers, the trap would represent a promising tool for the creation and investigation of two-dimensional systems.

Fast and accurate magnetic field control were essential for our measurements of three-body recombination at negative scattering lengths. In collaboration with another experiment in our group [Kra06b], we could exploit the unique magnetic tunability of interactions in ultracold cesium gases to provide the first evidence of Efimov quantum states. The link to Efimov physics has opened up exciting prospects for further investigations of few-body quantum phenomena. In order to strengthen this link, we have measured the temperature shift of the resonance position and have obtained results that agree with theoretical expectations on the basis of Efimov's framework. As a conclu-

sion, it is likely that a further experimental and theoretical characterization of ultracold cesium gases will lead to new insights into the physics of few-body quantum systems.

Outlook

In the future, the standing-wave surface trap could be used to create low-dimensional systems. Modified collisional properties [Pet00, Bou02] are expected when the scattering length a becomes comparable to the harmonic oscillator length a_{ho}. For a scattering length of $1000\,a_0$, with a_0 denoting Bohr's radius, this condition requires trapping frequencies of about 10 kHz. So far we have demonstrated frequencies up to 2.5 kHz, but the standing-wave surface trap could easily generate stronger confinement at higher laser powers. Since the trap does not require the use of a single-mode laser, fiber lasers might be a viable choice for high output powers.

Especially appealing would be to investigate Efimov physics in a system of reduced dimensionality. A feasible idea is to measure three-body recombination rates close to the observed resonance at large negative scattering lengths in the standing-wave surface trap. Significant changes of position, strength and width of the Efimov resonance are likely to be observable when the condition $a \sim a_{ho}$ of modified scattering is approached [Jon]. It is possible that the somewhat weaker condition of the recombination length ρ exceeding the harmonic oscillator length a_{ho} already leads to confinement-induced effects. For our maximum trapping frequency of 2.5 kHz with $a_{ho} = 3300\,a_0$, the resonant recombination length [Kra06b] $\rho = 10000\,a_0$ at a temperature of 250 nK is already the dominating length scale. However, a further reduction of the temperature would be highly desirable to increase the recombination length and to distinguish confinement-induced effects from the thermal effects which also affect the shape and position of the resonance.

Our present preparation scheme is limited by inefficient evaporation in the surface trap and the fact that the transfer from the MOT to the surface results in comparatively low atom numbers from the very beginning. Although a tiny condensate could be formed in the old apparatus, we are pessimistic about the prospects of creating a large condensate with the present approach. Fortunately, the flexible design of our apparatus allows for a major change in strategy by producing a large condensate in a standard dipole trap high above the prism with subsequent transfer to the surface.

A simple idea for the transfer exploits the already demonstrated possibility to freeze condensate expansion by magnetically switching the scattering length to zero [Her05]. This procedure should provide enough time to let the atoms fall and smoothly stop them on the surface with a time-dependent magnetic gradient.

Mixture of cesium and rubidium

At present, efforts are under way to add ^{87}Rubidium to the system. Loading a precooled mixture into a levitated dipole trap is facilitated by the almost equal ratio of

magnetic moment to atomic mass in the lowest internal states of cesium and rubidium. In a dipole trap at a wavelength of about 1060 nm, forced evaporative cooling should selectively affect the rubidium atoms due to different potential depths for the two species. Sympathetic cooling of cesium might offer a viable route to obtain large condensates, with rubidium regarded as a mere helping coolant.

Of course, ultracold mixtures present an intriguing area of research in its own right. So far, little is known about collisions between cesium and rubidium [And05]. A search for interspecies Feshbach resonances would be the natural starting point for a characterization of interactions. If accessible, such resonances could enable the creation of heteronuclear molecules and pave the way for experiments on deeply bound molecules with large permanent electric dipole moments [Sag05] and strong dipolar interactions.

It is interesting to note that weakly bound dimers should exhibit strong dipolar effects as well, yet in a different way. The application of laser light at a wavelength that is tuned in between the main absorption lines of the species imposes an optical potential that differs in sign for the two species. For a certain wavelength, the absolute magnitude of the potential will be the same, but the light is blue-detuned and repulsive for one species and red-detuned and attractive for the other. In an intensity gradient, one species will seek high intensities, while the other is repelled to low intensities.

Let us now consider a heteronuclear dimer that is exposed to such an intensity gradient. We assume that the molecular bond has little effect on the optical polarizabilities, which is a good approximation for weakly-bound dimers. It is intuitively clear that the opposing forces on the species tend to align the molecule. Although the potentials cancel to lowest order, the finite size of the molecule and the gradient give rise to a significant potential energy that depends on the orientation of the molecule. In analogy to an electric dipole of opposing charges that interacts with a gradient in the electrostatic potential, we now deal with a dipole of opposing polarizabilities that interacts with a gradient in the optical intensity.

In our case of a Rb-Cs mixture, we readily have a Titanium-Sapphire laser available that could provide light at the required wavelength. A convenient way to achieve large gradients would be a standing-wave trap, and potential depths of a few microkelvin are attainable at moderate power and focussing. The potential then changes by a few microkelvin over a distance of $\lambda/4 \simeq 200\,\mathrm{nm}$. On the other hand, the size of a weakly-bound dimer can easily reach $500\,a_0$. Taking the ratio of these length scales and multiplying with the potential depth leads to dipole energies on the order of a microkelvin. We conclude that these dipolar forces are sufficiently strong to compete with the thermal motion in an ultracold sample and to provide polarized dimers, and they could even be used to deform or dissociate the molecules.

Although there are many unknowns and experimental challenges ahead, the prospect of a quantum gas of molecules with anisotropic properties and tunable interactions is surely worth an effort.

A Cesium Hyperfine Structure and Zeeman Effect

The cesium ground state at vanishing magnetic field is composed of two hyperfine states which are separated by about 9.2 GHz. In the presence of magnetic fields, each hyperfine state splits into its m_F-substates due to the Zeeman effect. The exact Zeeman shifts can be calculated via the Breit-Rabi formula given in [Bre31]. As a consequence of the strong hyperfine interaction for cesium, it is mostly sufficient to consider first and second order Zeeman shifts. Here we derive the relevant formulas and provide accurate numerical values. In addition to frequency shifts, first-order corrections to the states and the matrix elements of the spin operators are evaluated.

Cesium in its electronic ground state carries no orbital angular momentum ($L = 0$), so the ground state structure is given by the spins of the electron $S = \frac{1}{2}$ and of the nucleus $I = \frac{7}{2}$. These values give rise to a 16-dimensional Hilbert space that describes all possible spin orientations.

In the atomic Hamiltonian there are only three terms affecting the spin structure of the ground state [Pet02]:

$$H = A\,\vec{I}\cdot\vec{S} + CS_z + DI_z \tag{A.1}$$

The first term proportional to $\vec{I}\cdot\vec{S}$ describes the hyperfine splitting at zero magnetic field. Its origin lies in the contact term of the magnetic interaction between the spins [CT97]. The interaction is mainly described by the magnetic dipole-dipole term, but this term vanishes because of the spherical symmetry of the electronic motion in the ground state. On the other hand, the contact term takes into account that the nucleus is not a point-like dipole by correcting the magnetic dipole-dipole formula inside the nucleus. This term doesn't vanish, since the electronic wavefunction in the ground state is not zero at the position of the nucleus.

The second and third term are due to the Zeeman Effect in an external magnetic field B, which is taken to be in the z-direction. The magnetic dipoles associated with the spins of the electron and the nucleus interact with B, and the constants C and D are proportional to the magnitude of B.

For cesium, the constants in A.1 are given by

$$\begin{aligned} A &= 2298157942.5\,\mathrm{Hz} * h \\ C &= 2802495.0 * B/\mathrm{G} * \mathrm{Hz} * h \\ D &= -561.7 * B/\mathrm{G} * \mathrm{Hz} * h \end{aligned}$$

The value of A is determined by the definition of the second (see equation A.3). The value of C is given by $C = g_{el}\mu_B B$ with $g_{el} = 2.002319$ [Ber92] and $\mu_B = 9.274009 \times 10^{-28}$ J/G [Pet02]. D is given by $D = -B\mu/I$ with $\mu = 2.579\,\mu_N$, $I = 7/2$ and $\mu_N = 5.050783 \times 10^{-31}$ J/G [Pet02].

At magnetic field strengths of a few Gauss, there is a clear hierarchy for the constants: A lies in the GHz range, C in the MHz range and D in the kHz range. Therefore the hyperfine interaction dominates, perturbed by the Zeeman effect of the electronic spin. The Zeeman effect due to the nuclear spin provides only a very small correction and is often negligible.

The Hamiltonian A.1 with constants A.2 presents the physical model for the Zeeman effect of the hyperfine structure of cesium. The following (purely mathematical) calculations reveal the consequences of the model.

Without external magnetic field ($C = D = 0$), the Hamiltonian A.1 is diagonal in the $|F, m_F\rangle$ basis, where $\vec{F} = \vec{I} + \vec{S}$ is the total spin:

$$H = A\,\vec{I}\cdot\vec{S} = \frac{A}{2}\left(\vec{F}^2 - \vec{I}^2 - \vec{S}^2\right) \tag{A.2}$$

F can take on the values $\frac{7}{2} \pm \frac{1}{2}$, i.e. $F = 3$ and $F = 4$. The energy of these two hyperfine levels is

$$E^{(0)} = \frac{A}{2}\left(F(F+1) - \frac{7}{2}\left(\frac{7}{2}+1\right) - \frac{1}{2}\left(\frac{1}{2}+1\right)\right)$$

$F = 3$ is therefore the lower hyperfine state (7-fold degenerate) with an energy $-\frac{9}{4}A$, whereas $F = 4$ represents the upper hyperfine state (9-fold degenerate) with an energy $\frac{7}{4}A$. The hyperfine splitting ΔE is

$$\Delta E^{(0)} = 4A = 9'192'631'770\,Hz \times h, \tag{A.3}$$

which is exact by definition of the second.

In an external magnetic field, the Zeeman energy terms in the Hamiltonian A.1 can be treated as a perturbation [CT97] as long as the field is not too strong. One writes

$$H = H_0 + W$$

with $H_0 = A\,\vec{I}\cdot\vec{S}$ and $W = CS_z + DI_z$. The unperturbed basis states $|F, m_F\rangle$ are degenerate, so in order to find the correct zero-order states we have to diagonalize W in the subspace $F = 3$ and in $F = 4$. As the perturbation W commutes with F_z, its matrix elements between basis states with different m_F vanish. Since inside each subspace $F = 3$ or $F = 4$ every basis state has a different value of m_F, the $|F, m_F\rangle$ basis already diagonalizes the restricted W and therefore gives the correct zero-order states of the perturbative expansion.

Using the appropriate Clebsch-Gordan coefficients [CT97], the $|F, m_F\rangle$ states can be expanded in the eigenstate basis $|m_S, m_I\rangle$ of S_z and I_z

$$\begin{aligned} |F = 4, m_F\rangle &= \sqrt{\frac{4 + m_F}{8}}\,|\frac{1}{2}, m_F - \frac{1}{2}\rangle + \sqrt{\frac{4 - m_F}{8}}\,|-\frac{1}{2}, m_F + \frac{1}{2}\rangle \\ |F = 3, m_F\rangle &= -\sqrt{\frac{4 - m_F}{8}}\,|\frac{1}{2}, m_F - \frac{1}{2}\rangle + \sqrt{\frac{4 + m_F}{8}}\,|-\frac{1}{2}, m_F + \frac{1}{2}\rangle \end{aligned}$$

Then the following matrix elements can be calculated

$$\langle 3, m_F|\, S_z\, |3, m_F\rangle = -\frac{1}{8}\, m_F \tag{A.4}$$

$$\langle 3, m_F|\, I_z\, |3, m_F\rangle = \frac{9}{8}\, m_F \tag{A.5}$$

$$\langle 4, m_F|\, S_z\, |4, m_F\rangle = \frac{1}{8}\, m_F \tag{A.6}$$

$$\langle 4, m_F|\, I_z\, |4, m_F\rangle = \frac{7}{8}\, m_F \tag{A.7}$$

$$\langle 4, m_F|\, S_z\, |3, m_F\rangle = -\frac{1}{8}\sqrt{16 - m_F^2} \tag{A.8}$$

$$\langle 4, m_F|\, I_z\, |3, m_F\rangle = \frac{1}{8}\sqrt{16 - m_F^2} \tag{A.9}$$

These matrix elements are needed to evaluate the perturbation series. The first order energy correction is given by

$$E^{(1)}_{F,m_F} = \langle F, m_F|\, W\, |F, m_F\rangle \tag{A.10}$$

with $W = C\, S_z + D\, I_z$. Therefore

$$E^{(1)}_{F=3,m_F} = -\frac{1}{8}\, C\, m_F + \frac{9}{8}\, D\, m_F \tag{A.11}$$

$$E^{(1)}_{F=4,m_F} = \frac{1}{8}\, C\, m_F + \frac{7}{8}\, D\, m_F \tag{A.12}$$

Since the constants C and D are proportional to the magnetic field B, these equations describe the linear Zeeman effect. In many cases the contribution of the nuclear spin is negligible, since D is much smaller than C. The first order shift is then $\mu_B/4 * m_F * B$ which gives $350\,\mathrm{kHz} * m_F * B/\mathrm{G} * h$.

The general formula for the second-order energy correction is

$$E^{(2)}_0 = \sum_{n \neq 0} \sum_i \frac{1}{E^{(0)}_0 - E^{(0)}_n}\, |\langle \varphi^i_n|\, W\, |\psi^{(0)}_0\rangle|^2 \tag{A.13}$$

Here $|\psi^{(0)}_0\rangle$ denotes the unperturbed level with energy $E^{(0)}_0$ in zeroth order. The sum is taken over all basis states $|\varphi^i_n\rangle$ with an energy $E^{(0)}_n$ different from $E^{(0)}_0$. So in the

degenerate case not only the state to be corrected, but also the other states of the same energy level are left out. In our case, the energy correction of a state in $F = 3$ involves only the $F = 4$ states and vice versa:

$$E^{(2)}_{F=3,m_F} = \sum_{m=-4}^{m=4} \frac{1}{-\frac{9}{4}A - \frac{7}{4}A} \, |\langle F = 4, m \,|\, W \,|F = 3, m_F\rangle|^2 \tag{A.14}$$

$$E^{(2)}_{F=4,m_F} = \sum_{m=-3}^{m=3} \frac{1}{\frac{7}{4}A - (-\frac{9}{4}A)} \, |\langle F = 3, m \,|\, W \,|F = 4, m_F\rangle|^2 \tag{A.15}$$

Using A.8, A.9 and the fact that $W = C\,S_z + D\,I_z$ couples only basis states with the same m_F, one gets

$$E^{(2)}_{F,m_F} = \mp \frac{1}{256A} \,(16 - m_F^2)\,(C - D)^2 \tag{A.16}$$

with the minus sign for $F = 3$ and plus for $F = 4$. Thus the quadratic Zeeman effect lowers the energy for $F = 3$ and increases it for $F = 4$, except for the states $|F = 4, m_F = \pm 4\rangle$ with vanishing quadratic energy correction.

We now calculate the first order correction of the states. The general formula is

$$\begin{aligned} |\psi^{(1)}_{0,r}\rangle &= \sum_{n\neq 0} \sum_i \frac{1}{E^{(0)}_0 - E^{(0)}_n} \,\langle \varphi^i_n \,|\, W \,|\psi^{(0)}_{0,r}\rangle \,|\varphi^i_n\rangle \\ &\quad + \sum_{s\neq r} \sum_{n\neq 0} \sum_i \frac{1}{E^{(1)}_{0,r} - E^{(1)}_{0,s}} \frac{1}{E^{(0)}_0 - E^{(0)}_n} \langle \psi^{(0)}_{0,s}| \, W \,|\varphi^i_n\rangle\langle\varphi^i_n| \, W \,|\psi^{(0)}_{0,r}\rangle \,|\psi^{(0)}_{0,s}\rangle \end{aligned}$$

Here it is assumed that the degeneracy of E_0 is lifted in first order, with the first order corrections denoted by $E^{(1)}_{0,r}$. The second line describes the coupling between the degenerate states within the level E_0. In our case, this contribution vanishes, as W only couples to the state with the same m_F in the other hyperfine level, and from there W can only couple back to the original state. So we are left with

$$|\psi^{(1)}_{F=3,m_F}\rangle = \frac{1}{-4A} \,\langle F = 4, m_F| \, CS_z + DI_z \,|F = 3, m_F\rangle \,|F = 4, m_F\rangle \tag{A.17}$$

and a similar equation for $F = 4$. Using A.8, A.9 we arrive at

$$|\psi^{(1)}_{F,m_F}\rangle = \pm \frac{1}{32A} \sqrt{16 - m_F^2}\,(C - D)\,|F \pm 1, m_F\rangle \tag{A.18}$$

with the plus sign for $F = 3$ and minus for $F = 4$. Thus the presence of an external magnetic field leads to mixing between states with the same m_F in the two hyperfine levels.

Insertion of the values A.2 leads to the following numerical expressions for the Zeeman energies:

$$\begin{aligned} E^{(1)+(2)}_{F=3,m_F}/(\mathrm{Hz} * h) &= -350943.7875\, m_F\, B/\mathrm{G} - 13.355\,(16 - m_F^2)\,(B/\mathrm{G})^2 \\ E^{(1)+(2)}_{F=4,m_F}/(\mathrm{Hz} * h) &= +349820.3875\, m_F\, B/\mathrm{G} + 13.355\,(16 - m_F^2)\,(B/\mathrm{G})^2 \end{aligned}$$

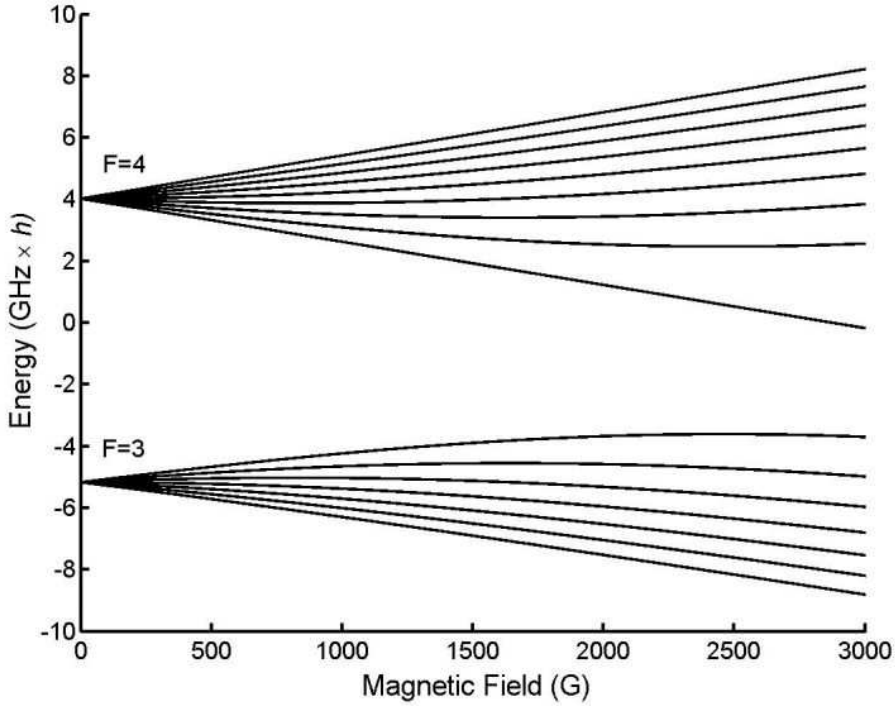

Figure A.1: Zeeman effect of the cesium hyperfine structure

For example, the frequency of the clock transition $|3,0>$ to $|4,0>$ shifts by $427\,\mathrm{Hz} * (B/\mathrm{G})^2$ due to the second-order Zeeman effect.

It is also possible to diagonalize A.1 without relying on perturbation theory. In fact, the Hamiltonian separates into 2×2 matrices which are straightforward to diagonalize, leading to the Breit-Rabi formula given in [Bre31]. By comparison with the exact energies the results of second-order perturbation theory are found to deviate by at most $30\,\mathrm{Hz} * h$ at a field of 10 G, and $30\,\mathrm{kHz} * h$ at 100 G.

B Magnetic levitation

A magnetic gradient field can be used to apply magnetic forces which partially or fully compensate gravity. We provide accurate numerical values for levitation of the $|F = 3, m_F = 3\rangle$ state and discuss the issue of horizontal anti-trapping forces.

The gravitational potential energy for a cesium atom at height z is $U_{grav} = mgz$, where m denotes the atomic mass and g is the local acceleration constant. For Innsbruck, g takes a value of $9.80553\,\mathrm{m/s^2}$ [BGI] and we get

$$U_{grav}\,/\,h = 32.659\,\mathrm{MHz} * z/\mathrm{cm} \tag{B.1}$$
$$U_{grav}\,/k_B = 1567.4\,\mu\mathrm{K} * z/\mathrm{cm} \tag{B.2}$$

Large and shallow optical traps can not hold the atoms against the force of gravity unless a supporting magnetic gradient is applied. In a magnetic field, the atomic ground state splits into its m_F-substates as described in appendix A. Under normal conditions the atom does not change its m_F-state when it moves around in the trap, since its spin adiabatically follows the local magnetic field. The Zeeman energy of the m_F-state can then be treated as a potential energy for the external atomic motion. With the results of appendix A we obtain the magnetic potential for atoms in $F = 3, m_F = 3$:

$$U_{mag}\,/\,h = -1.05283\,\mathrm{MHz} * B/\mathrm{G} - 93.5\,\mathrm{Hz} * (B/\mathrm{G})^2 \tag{B.3}$$
$$U_{mag}\,/k_B = -50.528\,\mu\mathrm{K} * B/\mathrm{G} - 4.49\,\mathrm{nK} * (B/\mathrm{G})^2 \tag{B.4}$$

For complete levitation, the magnetic force cancels gravity:

$$\frac{\partial U_{mag}}{\partial z} = -\frac{\partial U_{grav}}{\partial z} \tag{B.5}$$

With the negative signs in equations B.3 and B.4 indicating a high-field seeking state, the magnetic field must increase in the upward direction to compensate the downward force of gravity. When a quadrupole field is used to create the gradient, the zero of the field should therefore be situated below the atomic cloud. Equation B.5 leads to

$$\frac{\partial B}{\partial z} = 31.02\,\mathrm{G/cm} - 0.0055\,\mathrm{G/cm} * B/\mathrm{G} \tag{B.6}$$

Thus the levitation gradient is $31.02\,\mathrm{G/cm}$ with a small correction term from the quadratic Zeeman shift.

The application of a vertical magnetic gradient necessarily leads to horizontal anti-trapping forces. We consider a magnetic field configuration with a vertical symmetry axis, where horizontal components of the field vanish on axis for symmetry reasons. A vertical gradient β of the vertical magnetic field component is always accompanied by a horizontal gradient $-\beta/2$ of the horizontal components, since Maxwell's equations require $div\vec{B} = 0$. Let us consider a plane at fixed height with ρ denoting the horizontal distance to the axis. Close to the axis, the absolute value of the magnetic field is then

$$B = \sqrt{B_0^2 + \frac{\beta^2}{4}\rho^2} \simeq B_0 + \frac{\beta^2}{8B_0}\rho^2 \tag{B.7}$$

with B_0 denoting the absolute value of the vertical field. Thus the magnetic field increases in the horizontal directions which leads to a repulsive potential for high-field seeking atomic states.

For the state $F = 3, m_F = 3$, equation B.3 gives a linear Zeeman effect $U_{mag} = -\mu B$ with $\mu = 1.05283\,\mathrm{MHz/G} * h$, which is roughly $\mu \simeq 3\mu_B/4$ in terms of the Bohr magneton μ_B. Multiplication of equation B.7 with μ and expressing the quadratic term as $m\alpha^2\rho^2/2$ yields

$$\alpha = \beta\sqrt{\frac{\mu}{4mB_0}} \tag{B.8}$$

where $\alpha/(2\pi)$ is the anti-trapping frequency of the repulsive harmonic potential in the horizontal directions when a vertical magnetic gradient β is applied.

As an example, the full levitation gradient of 31 G/cm at an offset field of 10 G creates a horizontal anti-trapping potential with frequency $\alpha/(2\pi) = 4.4\,\mathrm{Hz}$. The anti-trapping frequency is reduced by a factor of two when either the gradient β is reduced by the same factor, or when the offset field B_0 is increased by a factor of four.

C Computer Control System

Automated experiment control requires a computer system that provides time-accurate output of many digital and analog signals, and also the read-in of analog signals and camera pictures.

At the heart of our system lies an Adwin-light card (with Adwin-LD extension) which is built in into our main control computer. The cards occupy two ISA-slots of the main computer. The upper card is the "Adwin-light" card (not "Adwin", or "Adwin-light-16" or "Adwin-Gold", these cards are different). It provides 6 digital inputs, 6 digital outputs, 2 analog outputs (12 bit), 8 analog inputs (single ADC with multiplexer) and 2 counters. The lower card is the "Adwin-LD" that adds 44 digital output channels. Both cards are connected to the same processor module "T400", a smaller extension at the inner end of the cards. Since the cards possess their own processor and clock that are independent of the main computer's Windows NT environment, a time-jitter of less than one microsecond is guaranteed.

External connections are made via a two-row, 37-pin sub-D connector in the upper slot for the Adwin-light, and a three-row, 50-pin sub-D connector in the lower slot for the Adwin-LD. Not all of the 44 digital outputs of the LD-card are used directly, 16 outputs are working as a data bus and 5 outputs as addressing bits. Three self-built extensions are connected to the bus-system. Two extensions contain 8 DACs each and one extension contains digital latches, so that we get 16 analog outputs and 32 additional digital outputs. All of the outputs are updated synchronously at a maximum rate of 10 kHz. The analog output extensions are carefully designed to avoid ground loops and provide clean 16-bit analog voltages from -10 V to 10 V.

The Adwin cards execute a program written in 'Adbasic' on their small processor. Before each experimental cycle, the desired digital and analog output sequence is transferred from a LabView user interface to the Adwin memory. The program is then responsible for the actual output, and synchronizes the timing sequence to the 50 Hz power line via an external line trigger. Path and name of the control program are "C:\Steuerung\Adwin\sequenzalles2.bas", and the lower-priority program "measure2.bas" deals with reading in analog input signals.

Images from two CCD-cameras are processed by a separate computer. A framegrabber card reads out images from a 14-bit Theta Systems camera. Pictures from an older 12-bit Princeton Instruments camera are grabbed and automatically saved by another computer, and are accessed through our Novell-network.

The user interfaces for the control and camera computers are programmed in LabView. Image analysis is done immediately after each cycle, using several Matlab scripts. The main settings and results of every cycle are saved to a log-file, which can be interpreted by another Labview program. In total, the system not only provides automatic control of the experiment, but also produces real-time plots of the data that is obtained.

Additional information can be found at

- the "Adwin / Portexpander" folder of our manual collection in the lab
- the electronic folder "C:\Steuerung\Adwin" of our main control computer
- the Jäger-Messtechnik homepage "http:// www.adwin.de/"

D Publications

Temperature shift of a triatomic Efimov resonance in an ultracold gas of cesium atoms

B. Engeser, K. Pilch, A. D. Lange, H.-C. Nägerl, and R. Grimm
in preparation

Evidence for Efimov quantum states in an ultracold gas of caesium atoms

T. Kraemer, M. Mark, P. Waldburger, J. G. Danzl, C. Chin, B. Engeser, A. D. Lange, K. Pilch, A. Jaakkola, H.-C. Nägerl, and R. Grimm
Nature **440**, 315 (2006).

Two-Dimensional Bose-Einstein Condensate in an Optical Surface Trap

D. Rychtarik, B. Engeser, H.-C. Nägerl, and R. Grimm
Phys. Rev. Lett. **92**, 173003 (2004).

Evanescent-Wave Trapping and Evaporative Cooling of an Atomic Gas at the Crossover to Two Dimensions

M. Hammes, D. Rychtarik, B. Engeser, H.-C. Nägerl, and R. Grimm
Phys. Rev. Lett. **90**, 173001 (2003).

References

[And05] M. Anderlini, E. Courtade, M. Cristiani, D. Cossart, D. Ciampini, C. Sias, O. Morsch, and E. Arimondo, *Sympathetic cooling and collisional properties of a Rb-Cs mixture*, Phys. Rev. A **71**, 061401(R) (2005).

[Bed00] P. F. Bedaque, E. Braaten, and H.-W. Hammer, *Three-body Recombination in Bose Gases with Large Scattering Length*, Phys. Rev. Lett. **85**, 908 (2000).

[Ber92] Bergmann Schaefer, *Teilchen*, vol. 4 of *Lehrbuch der Experimentalphysik*, Walter de Gruyter, 1992.

[BGI] *Bureau Gravimétrique International*, Gravity reference station 005311 at Innsbruck International Airport, <http://bgi.cnes.fr/>.

[Bou02] I. Bouchoule, M. Morinaga, C. Salomon, and D. Petrov, *Cesium gas strongly confined in one dimension: Sideband cooling and collisional properties*, Phys. Rev. A **65**, 033402 (2002).

[Bra01] E. Braaten and H.-W. Hammer, *Three-Body Recombination into Deep Bound States in a Bose Gas with Large Scattering Length*, Phys. Rev. Lett. **87**, 160407 (2001).

[Bra06] E. Braaten and H.-W. Hammer, *Universality in Few-body Systems with Large Scattering Length*, Physics Reports **428**, 259 (2006).

[Bre31] G. Breit and I. I. Rabi, *Measurement of Nuclear Spin*, Phys. Rev. **38**, 2082 (1931).

[Bri04] F. Bringas, M. T. Yamashita, and T. Frederico, *Triatomic continuum resonances for large negative scattering lengths*, Phys. Rev. A **69**, 040702(R) (2004).

[Bur97] E. A. Burt, R. W. Ghrist, C. J. Myatt, M. J. Holland, E. A. Cornell, and C. E. Wieman, *Coherence, Correlations, and Collisions: What One Learns about Bose-Einstein Condensates from Their Decay*, Phys. Rev. Lett. **79**, 337 (1997).

[Chi04] C. Chin, V. Vuletić, A. Kerman, S. Chu, E. Tiesinga, P. Leo, and C. Williams, *Precision Feshbach spectroscopy of ultracold Cs_2*, Phys. Rev. A 032701 (2004).

[Col03] Y. Colombe, D. Kadio, M. Olshanii, B. Mercier, V. Lorent, and H. Perrin, *Schemes for loading a Bose-Einstein condensate into a two-dimensional dipole trap*, J. Opt. B: Quantum Semiclassical Opt. **5**, 155 (2003).

[CT97] C. Cohen-Tannoudji, B. Diu, and F. Laloë, *Quantenmechanik*, vol. 2, Walter de Gruyter, 1997.

[Det01] S. Dettmer, D. Hellweg, P. Ryytty, J. J. Arlt, W. Ertmer, K. Sengstock, D. S. Petrov, G. V. Shlyapnikov, H. Kreutzmann, L. Santos, and M. Lewenstein, *Observation of Phase Fluctuations in Elongated Bose-Einstein Condensates*, Phys. Rev. Lett. **87**, 160406 (2001).

[D'I04] J. P. D'Incao, H. Suno, and B. D. Esry, *Limits on Universality in Ultracold Three-Boson Recombination*, Phys. Rev. Lett. **93**, 123201 (2004).

[Dow96] J. Dowling and J. Gea-Banacloche, *Evanescent light-wave atom mirrors, resonators, wave-guides, and traps*, Adv. At. Mol. Opt. Phys. **37**, 1 (1996).

[Du04] S. Du, M. B. Squires, Y. Imai, L. Czaia, R. A. Saravanan, V. Bright, J. Reichel, T. W. Hänsch, and D. Z. Anderson, *Atom-chip Bose-Einstein condensation in a portable vacuum cell*, Phys. Rev. A **70**, 053606 (2004).

[Efi70] V. Efimov, *Energy levels arising from resonant two-body forces in a three-body system*, Phys. Lett. B **33**, 563 (1970).

[Efi71] V. Efimov, *Weakly-bound states of three resonantly-interacting particles*, Sov. J. Nucl. Phys. **12**, 589 (1971).

[Esr] B. D. Esry, private communication.

[Esr99] B. D. Esry, C. H. Greene, and J. P. Burke, *Recombination of Three Atoms in the Ultracold Limit*, Phys. Rev. Lett. **83**, 1751 (1999).

[Fed96] P. O. Fedichev, M. W. Reynolds, and G. V. Shlyapnikov, *Three-Body Recombination of Ultracold Atoms to a Weakly Bound s Level*, Phys. Rev. Lett. **77**, 2921 (1996).

[For00] F. de Fornel, *Evanescent Waves: From Newtonian Optics to Atom Optics*, Springer, 2000.

[Gör01] A. Görlitz, J. Vogels, A. Leanhardt, C. Raman, T. Gustavson, J. Abo-Shaeer, A. Chikkatur, S. Gupta, S. Inouye, T. Rosenband, and W. Ketterle, *Realization of Bose-Einstein Condensates in Lower Dimensions*, Phys. Rev. Lett. **87**, 130402 (2001).

[Gri00] R. Grimm, M. Weidemüller, and Y. Ovchinnikov, *Optical Dipole Traps for Neutral Atoms*, Adv. At. Mol. Opt. Phys. **42**, 95 (2000).

[Ham02a] M. Hammes, *Optical Surface Microtraps based on Evanescent Waves*, Ph.d. thesis, Univ. Innsbruck (2002).

[Ham02b] M. Hammes, D. Rychtarik, H.-C. Nägerl, and R. Grimm, *Cold-atom gas at very high densities in an optical surface microtrap*, Phys. Rev. A **66**, 051401 (2002).

[Ham03] M. Hammes, D. Rychtarik, B. Engeser, H.-C. Nägerl, and R. Grimm, *Evanescent-Wave Trapping and Evaporative Cooling of an Atomic Gas at the Crossover to Two Dimensions*, Phys. Rev. Lett. **90**, 173001 (2003).

[Hen97] C. Henkel, K. Mølmer, R. Kaiser, N. Vansteenkiste, C. I. Westbrook, and A. Aspect, *Diffuse atomic reflection at a rough mirror*, Phys. Rev. A **55**, 1160 (1997).

[Her05] J. Herbig, *Quantum-Degenerate Cesium: Atoms and Molecules*, Ph.d. thesis, Univ. Innsbruck (2005).

[Ino98] S. Inouye, M. R. Andrews, J. Stenger, M. H.-J., D. M. Stamper-Kurn, and W. Ketterle, *Observation of Feshbach resonances in a Bose-Einstein condensate*, Nature **392**, 151 (1998).

[Jen04] A. S. Jensen, K. Riisager, D. V. Fedorov, and E. Garrido, *Structure and reactions of quantum halos*, Rev. Mod. Phys. **76**, 215 (2004).

[Joc04] S. Jochim, *Bose-Einstein Condensation of Molecules*, Ph.d. thesis, Univ. Innsbruck (2004).

[Jon] S. Jonsell, private communication.

[Jon06] K. M. Jones, E. Tiesinga, P. D. Lett, and P. S. Julienne, *Ultracold photoassociation spectroscopy: Long-range molecules and atomic scattering*, Rev. Mod. Phys. **78**, 483 (2006).

[Ker00] A. Kerman, V. Vuletic, C. Chin, and S. Chu, *Beyond Optical Molasses: 3D Raman Sideband Cooling of Atomic Cesium to High Phase-Space Density*, Phys. Rev. Lett. **84**, 439 (2000).

[Ket96] W. Ketterle and N. J. van Druten, *Evaporative cooling of atoms*, Adv. At. Mol. Opt. Phys. **37**, 181 (1996).

[Ket99] W. Ketterle, D. S. Durfee, and D. M. Stamper-Kurn, *Making, probing and understanding Bose-Einstein condensates*, Proceedings of the International School of Physics 'Enrico Fermi', Course CXL, IOS Press, Amsterdam, 67–176 (1999).

[Kra06a] T. Kraemer, *to be published*, Ph.d. thesis, Univ. Innsbruck (2006).

[Kra06b] T. Kraemer, M. Mark, P. Waldburger, J. G. Danzl, C. Chin, B. Engeser, A. D. Lange, K. Pilch, A. Jaakkola, H.-C. Nägerl, and R. Grimm, *Evidence for Efimov quantum states in an ultracold gas of caesium atoms*, Nature **440**, 315 (2006).

[Man99] I. Manek, *Gravito-optical Surface Trap for Cesium Atoms*, Ph.d. thesis, Univ. Heidelberg (1999).

[Nie99] E. Nielsen and J. H. Macek, *Low-Energy Recombination of Identical Bosons by Three-Body Collisions*, Phys. Rev. Lett. **83**, 1566 (1999).

[O'H03] J. F. O'Hanlon, *A User's Guide to Vacuum Technology*, Wiley-Interscience, 2003.

[Ovc97] Y. B. Ovchinnikov, I. Manek, and R. Grimm, *Surface Trap for Cs atoms based on Evanescent-Wave Cooling*, Phys. Rev. Lett. **79**, 2225 (1997).

[Pet00] D. S. Petrov, M. Holzmann, and G. V. Shlyapnikov, *Bose-Einstein Condensation in Quasi-2D Trapped Gases*, Phys. Rev. Lett. **84**, 2551 (2000).

[Pet02] C. J. Pethick and H. Smith, *Bose-Einstein Condensation in Dilute Gases*, Cambridge University Press, 2002.

[Pil05] K. Pilch, *Weiterentwicklung eines Experiments zur Untersuchung zweidimensionaler Quantengase*, Diploma thesis, Univ. Innsbruck (2005).

[Pin97] P. W. H. Pinkse, A. Mosk, M. Weidemüller, M. W. Reynolds, T. W. Hijmans, and J. T. M. Walraven, *Adiabatically Changing the Phase-Space Density of a Trapped Bose Gas*, Phys. Rev. Lett. **78**, 990 (1997).

[Pit03] L. P. Pitaevskii and S. Stringari, *Bose-Einstein Condensation*, Oxford University Press, 2003.

[Pri04] L. Pricoupenko, H. Perrin, and M. Olshanii (Eds.), *Quantum Gases in Low Dimensions*, vol. 116, J. Phys. IV, 2004.

[Raa87] E. L. Raab, M. Prentiss, A. Cable, S. Chu, and D. E. Pritchard, *Trapping of Neutral Sodium Atoms with Radiation Pressure*, Phys. Rev. Lett. **59**, 2631 (1987).

[Ryc04a] D. Rychtarik, *Two-dimensional Bose-Einstein Condensate in an optical surface trap*, Ph.d. thesis, Univ. Innsbruck (2004).

[Ryc04b] D. Rychtarik, B. Engeser, H.-C. Nägerl, and R. Grimm, *Two-Dimensional Bose-Einstein Condensate in an Optical Surface Trap*, Phys. Rev. Lett. **92**, 173003 (2004).

[Sag05] J. M. Sage, S. Sainis, T. Bergeman, and D. DeMille, *Optical Production of Ultracold Polar Molecules*, Phys. Rev. Lett. **94**, 203001 (2005).

[SK98] D. M. Stamper-Kurn, H.-J. Miesner, A. P. Chikkatur, S. Inouye, J. Stenger, and W. Ketterle, *Reversible Formation of a Bose-Einstein Condensate*, Phys. Rev. Lett. **81**, 2194 (1998).

[Söd95] J. Söding, R. Grimm, and Y. B. Ovchinnikov, *Gravitational laser trap for atoms with evanescent-wave cooling*, Optics Communications **119**, 652 (1995).

[Söd99] J. Söding, D. Guéry-Odelin, P. Desbiolles, F. Chevy, H. Inamori, and J. Dalibard, *Three-body decay of a rubidium Bose-Einstein condensate*, Appl. Phys. B **69**, 257 (1999).

[Sou02] *Ultracold matter*, Nature Insight **416**, 205 (2002).

[Tie93] E. Tiesinga, B. J. Verhaar, and H. T. C. Stoof, *Threshold and resonance phenomena in ultracold ground-state collisions*, Phys. Rev. A **47**, 4114 (1993).

[Tow95] C. G. Townsend, N. H. Edwards, C. J. Cooper, K. P. Zetie, C. J. Foot, A. M. Steane, P. Szriftgiser, H. Perrin, and J. Dalibard, *Phase-space density in the magneto-optical trap*, Phys. Rev. A **52**, 1423 (1995).

[Tow96] C. G. Townsend, N. H. Edwards, K. P. Zetie, C. J. Cooper, J. Rink, and C. J. Foot, *High-density trapping of cesium atoms in a dark magneto-optical trap*, Phys. Rev. A **53**, 1702 (1996).

[Tre01] P. Treutlein, K. Chung, and S. Chu, *High-brightness atom source for atomic fountains*, Phys. Rev. A **63**, 051401 (2001).

[Wal92] H. Wallis, J. Dalibard, and C. Cohen-Tannoudji, *Trapping Atoms in a Gravitational Cavity*, Appl. Phys. B **54**, 407 (1992).

[Web03a] T. Weber, *Bose-Einstein Condensation of Optically Trapped Cesium*, Ph.d. thesis, Univ. Innsbruck (2003).

[Web03b] T. Weber, J. Herbig, M. Mark, H.-C. Nägerl, and R. Grimm, *Three-Body Recombination at Large Scattering Lengths in an Ultracold Atomic Gas*, Phys. Rev. Lett. **91**, 123201 (2003).

[Wei99] J. Weiner, V. S. Bagnato, S. Zilio, and P. S. Julienne, *Experiments and theory in cold and ultracold collisions*, Rev. Mod. Phys. **71**, 1 (1999).

[Yam] M. T. Yamashita, T. Frederico, and L. Tomio, *Three-boson recombination at ultralow temperatures*, arXiv:cond-mat/0608542 .

Vielen Dank

An dieser Stelle möchte ich allen meinen Dank aussprechen, die mich bei meiner Doktorarbeit unterstützt haben.

Ich bedanke mich herzlich bei...

Rudi, für sein weitreichendes Engagement für die gesamte Arbeitsgruppe und die wissenschaftliche Betreuung meiner Doktorarbeit in den vergangenen viereinhalb Jahren.

Charly, Almar, Gerhard, Antti und Andrea, meinen tatkräftigen Mitstreitern im Labor. Es war immer eine Freude, mit Euch zu arbeiten. Auch an die gemeinsame Zeit abseits der Uni, ob in den Bergen oder im Café, werde ich mich immer gerne erinnern.

David und Markus, die mit ihrer soliden Vorarbeit den Grundstein für unser Experiment gelegt haben.

Mattias, Elmar, Tino, Jens, Tobias, Toni, Gabriel R., Peter, Michael, Phillip, Hanns-Christoph, Francesca, Steven, Johann und Cheng, den Freunden des Cäsiumatoms, für viele kleine Hilfen und wertvolle Diskussionen.

Den derzeitigen und früheren Kollegen der benachbarten Experimente:
Selim, Markus B., Alex, Stefan R., Reece, Matthew, Christoph, Matthias, Gregor, Klaus, Johannes, Sascha, Michael H., Ina, Florian L., Stefan S., Harald, Florian S., Eric, Gabriel K., Andreas, Clarice, Raquel und Frederik, für ihre Hilfsbereitschaft und die nette Arbeitsatmosphäre.

Christine und allen weiteren Mitarbeitern aus den Sekretariaten und den Werkstätten, für die stets freundliche und zuverlässige Unterstützung.

Meiner Familie und meinen guten alten Freunden, die mir Rückhalt geben.

Diese Seite wurde am 3.12.2006 hinzugefügt und ist nicht Teil der Doktorarbeit.